APPLIED COMPUTATIONAL ELECTROMAGNETICS SOCIETY JOURNAL

December 2017
Vol. 32 No. 12
ISSN 1054-4887

The ACES Journal is abstracted in INSPEC, in Engineering Index, DTIC, Science Citation Index Expanded, the Research Alert, and to Current Contents/Engineering, Computing & Technology.

The illustrations on the front cover have been obtained from the research groups at the Department of Electrical Engineering, The University of Mississippi.

EMERITUS ASSOCIATE EDITORS-IN-CHIEF

EMERITUS EDITORIAL ASSISTANTS

DECEMBER 2017 REVIEWERS: REGULAR PAPERS

Shakil Ahmed
Rajesh Elangovan
Grant Ellis
Long Li
Yasser Madany
Samir Mahmoud
Peyman Mahouti
Xiao-Min Pan
Xuewei Ping
Jean Piou
Azhagumurugan R.
Anand R.
Ashish Singh
Varun Singh
Wenhua Yu

DECEMBER 2017 REVIEWERS: EXPRESS PAPERS

Shahid Ahmed
Volkan Akan
David Chen
William Coburn
Alistar Duffy
Yunus Erdemli
Alessandro Fanti
Randy Haupt
Maokun Li
Lifford McLauchlan
Pejman Rezaei
Rashid Saleem
Katherine Siakavara
Ashish Singh
Steven Weiss
Yu Mao Wu
Bo Zhao

THE APPLIED COMPUTATIONAL ELECTROMAGNETICS SOCIETY JOURNAL

Vol. 32 No. 12 December 2017

TABLE OF CONTENTS – REGULAR PAPERS

TABLE OF CONTENTS – EXPRESS PAPERS

Design of a Planar, Concentric Coil for the Generation of a Homogeneous Vertical Magnetic Field Distribution

Ben Minnaert, Lieven De Strycker, and Nobby Stevens

Research Group Dramco, ESAT
KU Leuven, Technology Campus Ghent, Ghent, Belgium
Ben.Minnaert@kuleuven.be, Lieven.DeStrycker@kuleuven.be, Nobby.Stevens@kuleuven.be

Abstract ─ This paper describes an algorithm to design a planar, concentric coil that generates a homogeneous vertical magnetic field distribution, with a target self inductance. The algorithm consists of several steps. The first step is the random generation of a large set of concentric coils, taken into consideration a number of boundary conditions such as the outer dimensions and the radius of the conducting wire. The optimal coil is found from this set after a twofold selection, namely on the self inductance value and on the uniformity of the vertical magnetic field, which was evaluated using a cost function. The algorithm is straightforward and based on closed expressions, which leads to a rapid execution of the procedure. We evaluated the algorithm on a representative reference configuration. The best coil of the large set was selected and the quasi-uniform field distribution of this coil was confirmed by experimental verification.

Index Terms ─ Magnetic field, planar coil, self inductance, uniform field distribution.

I. INTRODUCTION

In several growing domains such as inductive wireless powering [1-4], Radio Frequency IDentification (RFID) [5] and Near Field Communication (NFC) [6], two inductively coupled coils are used to transfer energy and to exchange information over a short-range, wireless link. In inductive wireless powering systems, the energy transfer dominates the design, while for RFID or NFC the emphasis is on the data transfer. In both approaches, an increased homogeneity of the magnetic field is a favorable property. For example, if the transmitter coil for an inductive wireless power transfer system generates a more homogeneous field, it enhances the flexibility of positioning the receiver coil [7]. This can be beneficial for the charging of low-power consumer electronics such as smartphones [8-10], but also for higher power applications, such as the on-road charging of electrical vehicles while they are driving [11, 12]. An increased homogeneity of the field is also for RFID and NFC applications beneficial: it increases the readout region and efficiency of information exchange [13], which is an advantage for, e.g., moving receivers. An example application is the registering of the RFID tags of cattle at an automatic feeding installation [14].

Besides the flat field distribution, it is also important to take the self inductance into account. If one wants to replace an existing coil with an optimized coil with a more homogeneous field, it will have a minimal impact on the rest of the circuitry if the self inductance is not modified.

In this study, we will develop an algorithm to design a concentric, fully planar, transmitter coil that leads to a high and quasi-uniform magnetic field distribution with a specific self inductance value. The result of the algorithm is a set of dimensional parameters that can be used directly to design the coil. Limitations imposed by, e.g., the wire radius, are taken into account.

Interesting work on the design of coils for the generation of quasi-uniform magnetic field generation has been published in recent years by various authors. Kim et al [15] designed a planar coil of multiple loops connected in series and parallel. They mix the current direction in each loop in forward and in reverse, thus generating a more uniform magnetic field distribution. The same alternate winding design is applied by Zhang and Chau [16] to continuously charge a moving receiver. They apply different transmitter coils next to each other with alternating current directions, to minimize the gap in the field distribution between different transmitter coils. In this way they create a more uniform magnetic field which allows for an enhanced energy transfer performance around the gap between the coils.

Casanova et al. [17] designed a dedicated coil of 20 cm by 20 cm for inductive wireless power transfer. The coil design is a flat spiral. The geometry is determined by sweeping all possible parameters, evaluating the magnetic field for all possibilities, and choosing the design that leads to the most flat field distribution using an objective function. An analogous procedure was used by Yinlian et al. [18] to design two coil structures that realize in parallel a flat field distribution.

Liu and Hui [19] have patented a technique, based

Submitted On: February 29, 2016
Accepted On: October 24, 2017

on a hybrid coil structure. It consists of a concentric coil and a spiral winding. A number of limitations are posed here, since the spacing between the spiral coil loops must be constant. It is also observed that the spiral coil is not located in the same plane of the concentric coil, which makes the structure inherently non-planar, which can be considered less attractive for most applications due to the increased height of the coil. The same applies for the work of Lee et al. [20] who proposed a technique to bend a rectangular coil further away from the receiving coil at the edges of this structure. By realizing a more uniform magnetic field distribution, they increased the overall transfer efficiency up to 44% compared to a conventional coil, regardless of the location of the receiving coil.

Waffenschmidt [7] developed an excellent algorithm to determine the turn distribution of a planar coil to generate a specified homogeneous field. In the first step, his algorithm calculates a current distribution from a specified magnetic field. In the second step, the corresponding turn distribution to this current distribution is derived. Using the generalized minimal residual method, this algorithm can be extended to more coil turns [21]. Azpúra [22] proposed a semi-analytical method for designing a coil that generates a more uniform field. Starting from the Biot-Savart law, he analytically determines the field distribution of a start configuration. He then uses an iterative algorithm based on TABU search to improve the homogeneity of the field. The number of turns of each coil and the thickness of wire is adjusted at each iteration until the required field is reached.

An important difference between our algorithm and the aforementioned references is that we impose a certain, by the user determined, self inductance for the planar coil. In that way, our improved coil will have a minimal impact on the rest of an existing circuitry since the self inductance is not modified. Previous related work always managed to increase the homogeneity of the field by, among others, changing the inductance. Moreover, as a result of the availability of closed expressions for the field distribution and self inductance, our algorithm can be evaluated in a very short time.

This paper is organized as follows. In Section II, the expressions for the field evaluation, the self inductance and the homogeneity of the field for a circular, concentric, planar coil are elaborated. These expressions are used extensively in the algorithm that is described in detail in Section III, which describes in detail the flow in order to obtain the planar coil with the best field distribution and a specific target self inductance. The algorithm is demonstrated on a representative example in Section IV, where the results are also verified experimentally. The main results are summarized in the conclusions (Section V).

In this study, we limit our attention to a concentric coil. The reason is that when a certain degree of freedom is offered to the user to position its electronic device, the most flexible solution is the one where there is no rotational preference direction. This obviously leads to a concentric configuration.

II. FIELD DISTRIBUTION AND INDUCTANCE CALCULATION

The vertical magnetic field generated by a circular current loop with radius *R* and current *I* is available in a closed form. If the origin of the coordinate set is chosen at the center of the circular loop, with the loop in the *xy*-plane, Equation (1) is applicable [23]:

$$H_z(r,z) = \frac{I}{2\pi}\frac{1}{\sqrt{(r+R)^2+z^2}} \cdot\left\{\mathcal{K}(k) - \frac{r^2-R^2+z^2}{(r-R)^2+z^2}\mathcal{E}(k)\right\}, \quad (1)$$

with

$$k = \frac{2\sqrt{rR}}{\sqrt{(r+R)^2+z^2}}. \quad (2)$$

Here, r and z are the cylindrical coordinates of the observation point, while $\mathcal{K}(k)$ and $\mathcal{E}(k)$ are the complete elliptic integrals of the first and second kind respectively. When multiple, concentric loops are present, as shown on Fig. 1, the field is found as the sum of the different loop contributions. Without loss of generality (due to linearity), we normalize the field at a current of 1 A. We suppose that the same current is flowing counterclockwise (top view) in the different loops. Equation (3) thus describes the vertical magnetic field generated by *N* concentric coils with different radii R_n:

$$H_z(r,z) = \frac{1}{2\pi}\sum_{n=1}^{N}\frac{1}{\sqrt{(r+R_n)^2+z^2}} \cdot\left\{\mathcal{K}(k_n) - \frac{r^2-R_n^2+z^2}{(r-R_n)^2+z^2}\mathcal{E}(k_n)\right\}, \quad (3)$$

with

$$k_n = \frac{2\sqrt{rR_n}}{\sqrt{(r+R_n)^2+z^2}}. \quad (4)$$

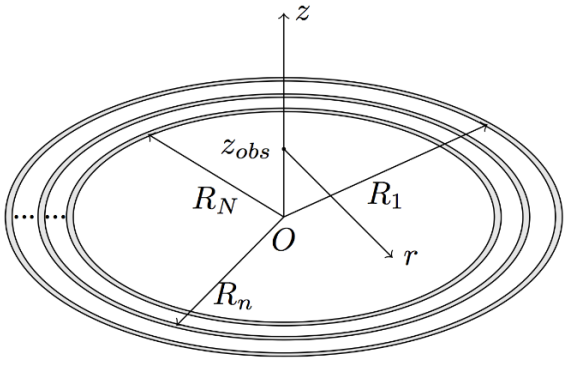

Fig. 1. Configuration under study with the corresponding conventions.

Since we want to design a planar, concentric coil with a certain target self inductance *L*, we need a closed expression for this lumped parameter. If the radius of the wire r_w is much smaller than the radius of the loop R_n,

the self inductance L can be approximated by [24]:

$$L = \sum_{n=1}^{N} \mu_0 R_n \left[\ln\left(\frac{8R_n}{r_w}\right) - 2\right] + \sum_{i=1}^{N}\sum_{j=1}^{N} M_{i,j}(1-\delta_{i,j}), \quad (5)$$

with

$$M_{i,j} = \mu_0\sqrt{R_i R_j}\left[\left(\frac{2}{k_{i,j}} - k_{i,j}\right)\mathcal{K}(k_{i,j}) - \frac{2}{k_{i,j}}\mathcal{E}(k_{i,j})\right], \quad (6)$$

and

$$k_{i,j} = \frac{2\sqrt{R_i R_j}}{R_i + R_j}. \quad (7)$$

$\delta_{i,j}$ is the Kronecker delta (zero for $i \neq j$ and 1 if $i = j$). In order to have a planar structure, the radial difference between any two different loops should be at least two times the radius of the wire r_w:

$$\left|R_i - R_j\right| \geq 2r_w \text{ for } i \neq j. \quad (8)$$

Based on previous expressions, we can construct a planar, circular concentric coil with a certain self inductance L. Once the dimensions of the different loops are chosen, the field at any height z_{obs} can be evaluated making use of expression (3). The goal is however, that an optimized coil with a specific self inductance L is defined, which leads to a homogeneous vertical field distribution at a specific observation height z_{obs}. In order to quantify the homogeneity of the field in an interval between r_{min} and r_{max}, we define the following cost function v:

$$v = \int_{r_{min}}^{r_{max}} \left|\frac{\mathrm{d}H_z(r,z_{obs})}{\mathrm{d}r}\right| \mathrm{d}r = \int_{r_{min}}^{r_{max}} |\mathrm{d}H_z(r,z_{obs})|. \quad (9)$$

It is clear that v will be minimal for flat and thus, homogeneous field distributions between r_{min} and r_{max}.

III. ALGORITHM

In our algorithm, we choose the maximal outer dimension of the coil, being $R_1 + r_w$, fixed. It has been proven [25] that the *distribution* of the magnetic field for a circular current loop is independent on the outer radius R. Indeed, expressions (1) and (3) can be rewritten as a function of two dimensionless parameters, the normalized radius and the normalized height, with R as the normalization variable [25]. R then acts as a scaling factor and does not modify the distribution.

The goal of the algorithm is to find a concentric, planar configuration with a given exterior dimension $R_1 + r_w$ and a given self inductance L that generates a homogeneous field distribution. If one wants to design a planar, concentric coil with a specific inductance using as less wire length as possible, it can be derived from expression (5) that all current loops must be located at the utmost exterior. We will call this configuration the reference coil with exterior dimension $R_1 + r_w$ (Fig. 2 shows such a coil with $N_{ref} = 10$ number of loops). Figure 3 shows the typical magnetic field distribution for such a configuration. One notices that the magnetic field in the center is lower than near the edges. It is clear that in order to realize a more uniform vertical field distribution, we have to increase the field in the central region. If we consider a second configuration where we fill the entire central region with current loops (i.e., a "disk configuration"), we obtain a magnetic field that is higher in the center than at the outer edges (Fig. 3). In this latter case, the different loops are closely stacked to each other and the different values (for n from 1 to N) are:

$$R_n = r_w + (N-n)2r_w. \quad (10)$$

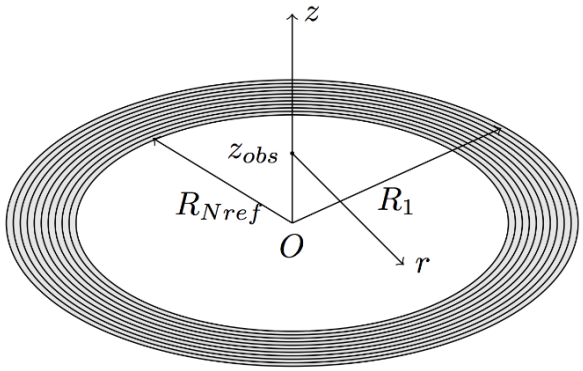

Fig. 2. Reference coil with all loops at the utmost exterior.

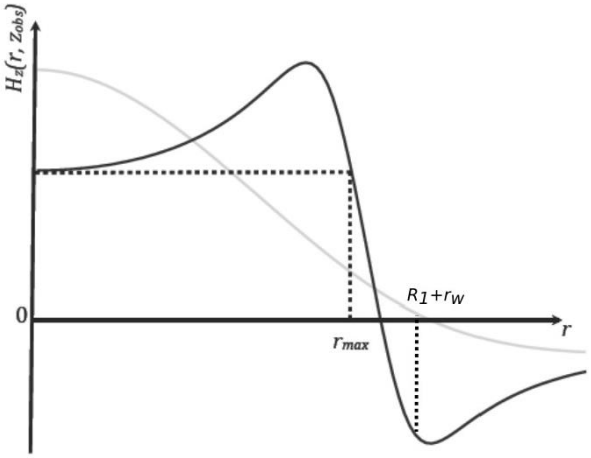

Fig. 3. Typical field distributions: all loops at the outer edge (black curve) and all loops lowest possible radius (gray curve).

Both typical field distributions are also found by other authors, e.g., [7]. Based on the distributions of Fig. 3, we can now propose a strategy to obtain a more homogeneous field distribution, with a given exterior dimension $R_1 + r_w$ and given self inductance L_{ref}. If we consider the reference coil and simply add extra loops in the central region, we obtain a more homogeneous field distribution. However, this would increase the self inductance. Therefore, in order to keep the self inductance fixed to the self inductance of the reference coil, we also will have to decrease the number of loops at the outer

edge. One can see, based on Equations (5) and (8), that the total number of loops of the optimized coil N_{opt} will be larger than N_{ref}.

The goal of the algorithm is to define a planar, concentric coil that leads to a significant more uniform *z*-oriented magnetic field. Therefore, we have to define a lateral region where this condition has to be realized, i.e., an interval over which the cost function *v* (Equation (9)) is to be evaluated. Since we want a field as homogeneous as possible over an area as large as possible, we choose the value of r_{min} to be 0, and let the value of r_{max} be determined by the reference coil. We define r_{max} as the radial distance where the decaying field becomes smaller than the value found in the center in the case of the reference coil, as illustrated graphically on Fig. 3. Above this radius r_{max}, the variation of the field is no longer relevant.

For the input of the algorithm, the following parameters are given by the user: the required self inductance L_{ref}, the radius of the wire r_w, the outer dimension of the planar coil $R_1 + r_w$ and the vertical distance z_{obs} where the magnetic field is to be observed. The algorithm is split in two steps. First, a set of concentric coils is created that have a self inductance that is close to the value of the required self inductance L_{ref}. In the second step, the configuration within this set that delivers the most uniform $H_z(r, z_{obs})$ (where *r* runs from 0 to r_{max}) is determined.

On Fig. 4, the flowchart of the algorithm is shown. At the start, the user inputs the values for L_{ref}, r_w, $R_1 + r_w$ and z_{obs}. From these data, the algorithm calculates for all possible reference coils (i.e., coils with all loops exterior) the corresponding inductance, based on expression (5). It then selects the coil with the inductance closest to L_{ref}. We call this the reference coil with number of loops N_{ref}. From this reference coil, the value of r_{max} is calculated (using Equation (3) and the given observation height z_{obs}).

The next task to be executed is the generation of a large set of planar coils. Therefore, the number and radii of the loops is modified and a random generator determines a new set of radii. The limitation on the random generator is that the difference of the values of the radii R_n must be at least $2r_w$ in order to keep the structure planar. The random generator returns uniformly distributed random numbers in the specified interval. We define N_{ext} as the number of loops that is kept at the most outside position and N_{int} as the number of loops that have a radius smaller than $R_1 - 2N_{ext}r_w$. These loops are thus located in the central part of the coil. Figure 5 shows an example, where N_{ext} equals 8 and N_{int} is 3. The total number of loops N_{opt} is of course $N_{ext} + N_{int}$. The only limitation towards the radii of the inner loops is that they must differ by at least $2r_w$. The difference between the interior loop radii values can vary.

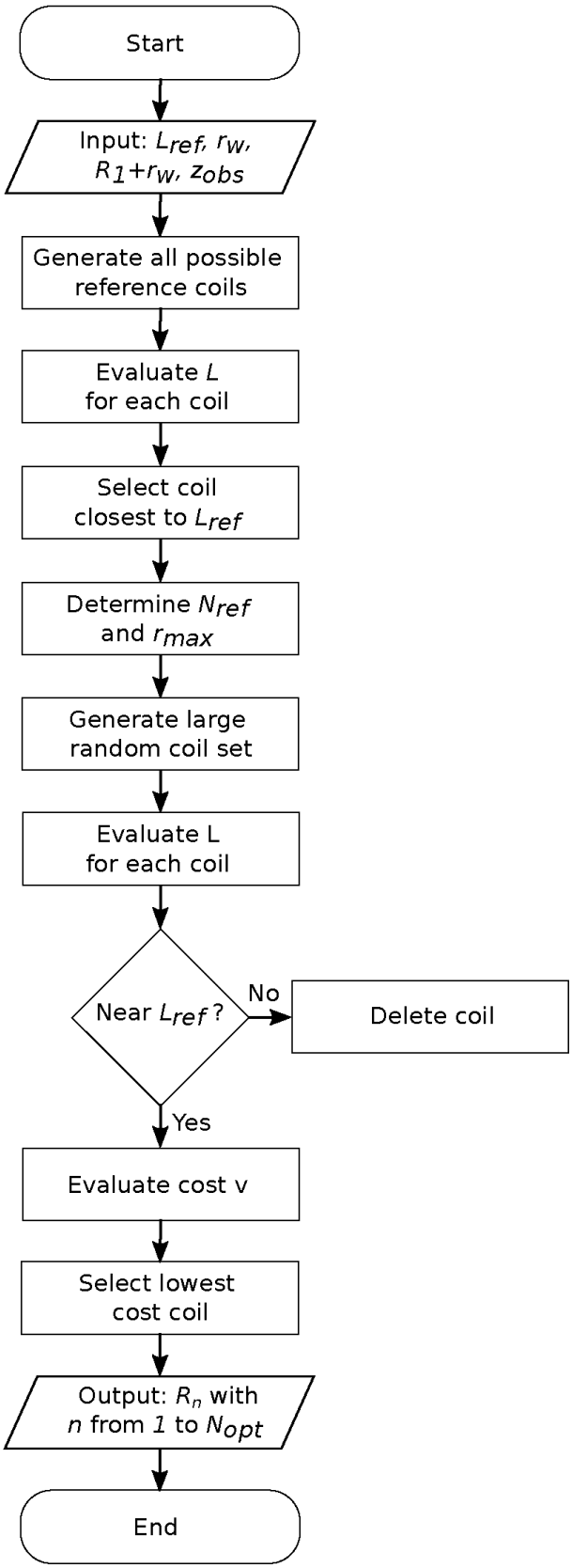

Fig. 4. Flowchart of the algorithm.

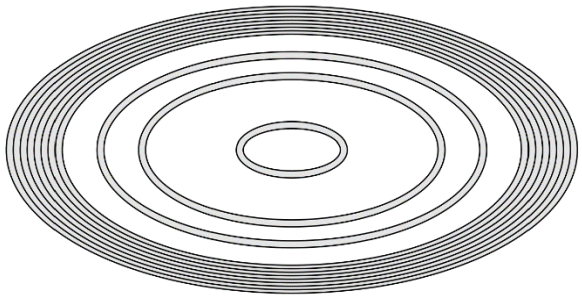

Fig. 5. Planar concentric coil with $N_{ext} = 8$ and $N_{int} = 3$.

Then the self inductance *L* of each coil is calculated by using the closed expression (5). Based on the calculated self inductance values, we decide which coils can be deleted and which ones are selected for further evaluation. The user has a certain degree of freedom here, but a relative difference of a couple of percent seemed a reasonable choice. For example, the Agilent 42851 Precision LCR meter has, depending on the measurement conditions, an inductance measurement accuracy of about 2%. Therefore, $L \in [0.98\, L_{ref},\ 1.02\, L_{ref}]$, which allows a maximum relative difference of 2%, are the boundaries we will choose in Section IV. At this point of the procedure, we have a large set of concentric coils with a self inductance that is close to the user specified L_{ref}.

The next step is the evaluation of the cost function *v* (expression (9)) for the remaining coils to find the current loop distribution that leads to the most uniform field for *r* between 0 and r_{max}. For the numerical evaluation of *v*, we approximate the integral of Equation (9) by a finite sum, as described by equation (11). Here, r_0 equals 0, r_{M+1} equals r_{max} and *M* is large. We have observed that this sum converges rapidly as *M* approaches several hundreds of evaluation points between 0 and r_{max}:

$$v \approx \sum_{m=0}^{M} |H_z(r_{m+1}) - H_z(r_m)|. \qquad (11)$$

Since this corresponds with the midpoint Riemann sum, the order of magnitude of the error as a consequence of this approximation is $\mathcal{O}((r_{max}/M)^2)$. In order to find the design with the most uniform vertical field distribution at the height z_{obs}, the coil with the smallest cost value *v* is selected. The outcome of the procedure delivers us all required parameters of the optimized planar coil: the number of loops N_{opt}, with the corresponding radii R_n.

IV. EXAMPLE AND EXPERIMENTAL VERIFICATION

To illustrate the algorithm, we apply it on a representative example. The dimensions of the set-up are based on the "power transmitter design A2" [26] from the Qi-standard that allows free positioning. We have constructed a reference coil with the following dimensions: $2r_w$ equals 0.83 mm (a wire that was available for measurement verification), $R_1 + r_w$ is 40 mm and the number of loops N_{ref} is 10. The exact numbers are not dedicated to our method, it rather allows us to focus the attention on the main, representative results. An observation height (z_{obs}) of 5 mm and frequency of 100 kHz was chosen, which are representative for the wireless charging of low power electronic devices [27] (with the exception of biological implants where larger distances and frequencies are more typical).

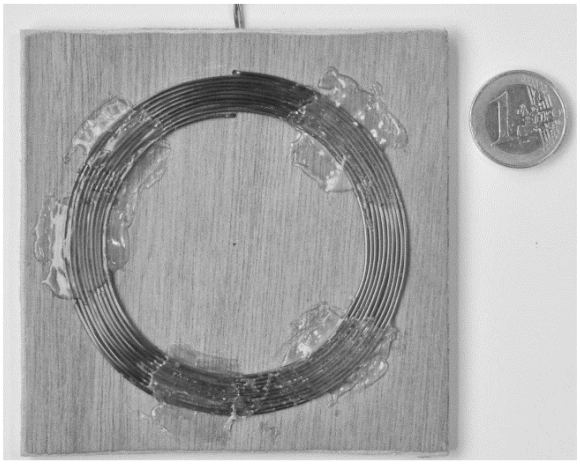

Fig. 6. The reference coil.

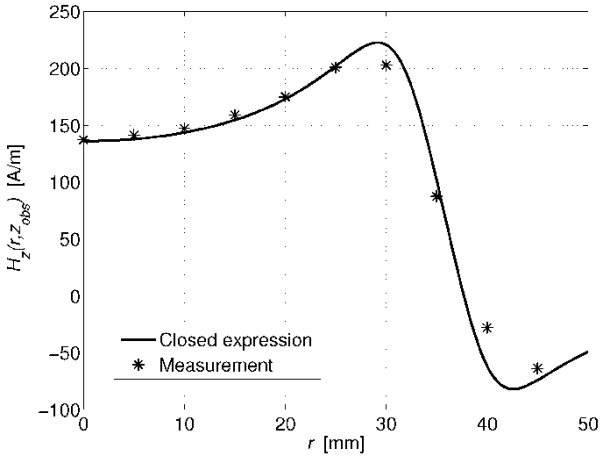

Fig. 7. Vertical magnetic field of the reference coil at the observation height z_{obs} of 5 mm.

A photograph of this coil is depicted on Fig. 6. The reflecting zones are caused by the glue to keep the loops at the same position. In order to have an estimate on the size of both coils, a one euro coin (that has a diameter of 23.25 mm) is also shown on the picture.

Application of the self inductance formula (Equation (5)) leads to a value of 13.24 µH for L_{ref}. The vertical magnetic field distribution is shown on Fig. 7, calculated

with closed expression (3), where the excitation current equals 1 A. For the rest of this study, the results are normalized to a current of 1 A. The distance r_{max}, as defined in the description of the algorithm, corresponds to a value of 34.9 mm in this specific configuration. As mentioned above, the variation of the field above this radius r_{max} is not relevant.

On Fig. 7, experimental data is also shown. We have used the GM08 Hand-held Gaussmeter from Hirst Magnetic Instruments Ltd. to measure the vertical magnetic field. Very good correspondence is obtained between the analytical formulation and the measured data. Now that we have defined the reference coil and verified its vertical field distribution, we can start the algorithm with the goal to find a planar concentric coil with a much more uniform field distribution at z_{obs}= 5 mm for *r* between 0 and r_{max}. In order to compare the results with our reference coil, we will require that the new planar coil has the same self inductance L_{ref} as our reference coil (i.e., 13.24 µH), with a maximum relative difference of ± 2%.

In total, we evaluated 10^5 different coils (interior radii random generated) with values for N_{ext} of 6 to 9, where the maximal value of $N_{ext} + N_{int}$ was 15. For larger values of $N_{ext} + N_{int}$, many small loops were at the interior in order to achieve the same inductance. This increases the field at the center too much so that field homogeneity cannot be reached anymore. With this set, 7488 coils (thus about 7.5%) passed the test of being close to the original L_{ref}, with a maximal relative difference of ± 2%. From these 7488 coils, the smallest *v*-number was 97.1 A/m, where the *v*-number of the reference coil was 179.7 A/m.

The coil that was selected has a theoretical self inductance L_{opt} of 13.27 µH, which deviates only 0.23% from the L_{ref} of 13.24 µH. The optimized coil has 9 exterior loops (N_{ext}) and 3 interior loops (N_{int}). The values of R_1 to R_9 are straightforward, since they are part of the exterior loops. R_n equals in our case $40 - 0.83/2 - (\mathrm{n} - 1)0.83$ mm, where *n* runs from 1 to 9. For the three other, interior loops we have a value of 26.41 mm for R_{10}, 20.80 mm for R_{11} and 12.95 mm for R_{12}. We fabricated this optimized coil, as can be seen on Fig. 8.

As a first verification, we measured the self inductance of our coils using an Agilent 42851 Precision LCR meter. We measured a value of 12.20 µH and 12.42 µH for respectively the reference coil and the optimized coil. Two observations can be made. In the first place, the measured self inductance deviates from the theoretical predictions based on the formula (5). On the one hand, this theoretical prediction is an approximation. On the other hand, one also has to take into account that due to practical reasons, it is not always possible for the entire circumference to reduce the distance between any two adjacent loops to zero. This will thus lead to some loss of self and mutual inductance. However, the most important observation, apart from the value itself, is that the two measured self inductances are close to each other, within a relative difference of 2%.

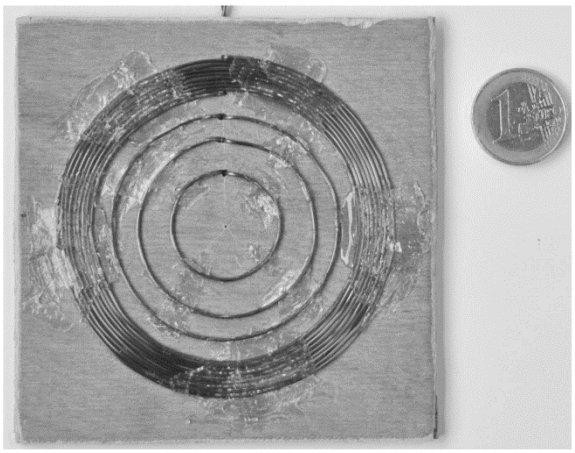

Fig. 8. The optimized coil.

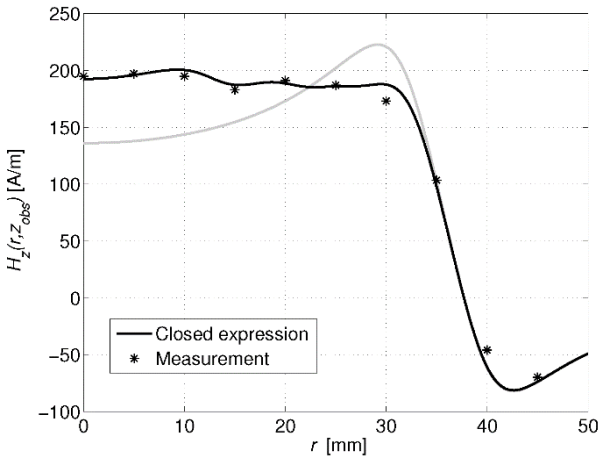

Fig. 9. Vertical magnetic field of the optimized coil at the observation height z_{obs} of 5 mm. The gray line shows the vertical magnetic field for the reference coil as comparison.

On Fig. 9, we have shown the field distribution of the coil with the minimal cost *v*, with the corresponding measurement result. One can see that the field itself, is indeed much more uniform over the *r*-region between 0 and r_{max}, which means that the cost *v* is a good selection criterion. A second observation, is that the field values are also high over the entire region, it is only at the outer regions of the optimized coil that the field values are smaller than the reference coil field values. On Fig. 9, a gray line with the result of the reference coil is added to facilitate the comparison. Remark that by minimizing the

cost v, we actually only targeted to obtain a uniform field, without directly imposing conditions on the value of this field. It turns out that a minimized cost also leads to a high field value. Table 1 summarizes the results for the reference and optimized coil.

Table 1: Overview of different parameters for the reference and optimized coil

	Reference Coil	Optimized Coil
N_{ext}	10	9
N_{int}	0	3
$L_{theoretical}$	13.24 µH	13.27 µH
$L_{measured}$	12.20 µH	12.42 µH
v	179.7 A/m	97.1 A/m

The algorithm for this example was executed in the numerical environment Matlab® on a modest computer, i.e., a MacBook Pro with an Intel Core i7 processor of 2.6 GHz with 4 GB 1600 MHz DDR3 SDRAM. It took 57.6 s for the algorithm to produce the end results for this representative example. The short algorithm time is due to the available closed-form expressions at the different steps. The time-consuming part is almost entirely attributed to the fact that many (10^5) coils need to be evaluated.

Because the algorithm chooses the best coil (with regard to the cost function v from a large coil set), the procedure always converges and produces a useful result. The user implementing our method has to be aware of two possible issues:

- Since the algorithm selects the optimal coil from a random generated coil set, the exact same solution will not be reproduced when the program is executed more than once. However, if the user sets the number of generated coils high enough (10^5 in our example), the end result will lead to as equally homogeneous magnetic field distribution, well within any practical measurement errors. Given the fast execution time of the algorithm on a modest machine, the user will not experience any significant obstacles by choosing a very large coil set.
- The novelty of this algorithm, compared to previous work, is that it imposes a by the user chosen self inductance L of the coil. This allows the user to replace an existing coil with the calculated coil, allowing a more homogeneous field with minimal impact on the rest of the network. The algorithm requires an interval for this self inductance L, for example a relative difference of 2% as chosen in this example. However, it might be beneficial to choose a larger interval, thus allowing more freedom to generate a uniform field distribution. Depending on the application, the user can, by circuital simulation, study the influence of varying the coil inductance and adapt the interval accordingly.

VI. CONCLUSION

In this paper, an algorithm to design a concentric, planar coil that leads to a homogeneous vertical magnetic field distribution is described. The novelty of this approach is that the procedure takes a certain target self inductance into account, so that the optimized coil can easily replace another coil without impact on the rest of the circuitry. As a consequence of the availability of closed expressions for the field distribution and self inductance, a very large set of random generated coils can be evaluated in a very short time. The result of the algorithm leads to all parameters required to realize the optimized planar coil, taken into account the radius of the wire in order to keep the structure planar. The method is applied on a representative coil. The results were verified experimentally and excellent correspondence was obtained.

ACKNOWLEDGMENT

The authors would like to thank iMinds and the Flemish Agency for Innovation by Science and Technology (IWT) for funding. The authors are also grateful to Bart Thoen from KU Leuven, who practically realized the different concentric coils with great attention for detail.

REFERENCES

[1] N. Shinohara, "The wireless power transmission: Inductive coupling, radio wave, and resonance coupling," *Wiley Interdisciplinary Reviews: Energy and Environment*, vol. 1, no. 3, pp. 337-346, 2012.

[2] X. Jin, J. M. Caicedo, and M. Ali, "Near-field wireless power transfer to embedded smart sensor antennas in concrete," *Applied Computational Electromagnetics Society Journal*, vol. 30, no. 3, 2015.

[3] M. H. Misran, A. Rahim, S. Kamal, A. A. Eteng, and G. A. Vandenbosch, "Assessment of kapton-based flexible antenna for near field wireless energy transfer," *Applied Computational Electromagnetics Society Journal*, vol. 32, no. 1, 2017.

[4] M. H. Salleh, N. Seman, and R. Dewan, "The investigation of substrate's dielectric properties for improving the performance of Witricity devices," *Applied Computational Electromagnetics Society Journal*, vol. 32, no. 1, 2017.

[5] G. Orecchini, L. Yang, A. Rida, F. Alimenti, M. M. Tentzeris, and L. Roselli, "Green technologies and RFID: Present and future," *Applied Computational Electromagnetics Society Journal*, vol. 25, no. 3, pp. 230-238, 2010.

[6] V. Coskun, K. Ok, and B. Ozdenizci, *NFC Essentials in Near Field Communication: From*

Theory to Practice. John Wiley & Sons, Ltd, Chichester, UK, 2012.

[7] E. Waffenschmidt, "Homogeneous magnetic coupling for free positioning in an inductive wireless power system," *Emerging and Selected Topics in Power Electronics, IEEE Journal of*, vol. 3, no. 1, pp. 226-233, 2015.

[8] W. X. Zhong, X. Liu, and S. R. Hui, "A novel single-layer winding array and receiver coil structure for contactless battery charging systems with free-positioning and localized charging features," *Industrial Electronics, IEEE Transactions on*, vol. 58, no. 9, pp. 4136-4144, 2011.

[9] X. Shi, C. Qi, M. Qu, S. Ye, and G. Wang, "Effects of coil locations on wireless power transfer via magnetic resonance coupling," *Applied Computational Electromagnetics Society Journal*, vol. 31, no. 3, 2016.

[10] E. Waffenschmidt and T. Staring, "Limitation of inductive power transfer for consumer applications," *Power Electronics and Applications, EPE'09. 13th European Conference on, IEEE*, pp. 1-10, 2009.

[11] S. Chopra and P. Bauer, "Driving range extension of EV with on-road contactless power transfer—A case study," *Industrial Electronics, IEEE Transactions on*, vol. 60, no. 1, pp. 329-338, 2013.

[12] T. E. Stamati and P. Bauer, "On-road charging of electric vehicles," *Industrial Electronics, In Transportation Electrification Conference and Expo (ITEC), IEEE*, pp. 1-8, 2013.

[13] S. C. Chen and V. Thomas, "Optimization of inductive RFID technology," *Electronics and the Environment, Proceedings of the 2001 IEEE International Symposium on*, pp. 82-87, 2001.

[14] N. Stevens, L. Destrycker, and W. Verschelde, "Procedure to calculate the inductance of a circular loop near a metal plate," *Przegląd Elektrotechniczny*, vol. 87, no. 9A, pp. 255-258, 2011.

[15] J. Kim, H.-C. Son, and Y.-J. Park, "Multi-loop coil supporting uniform mutual inductances for free-positioning WPT," *Electronics Letters*, vol. 49, no. 6, pp. 417-419, 2013.

[16] Z. Zhang and K. T. Chau, "Homogeneous wireless power transfer for move-and-charge," *IEEE Transactions on Power Electronics*, vol. 30, no. 11, pp. 6213-6220, 2015.

[17] J. J. Casanova, Z. N. Low, J. Lin, and R. Tseng, "Transmitting coil achieving uniform magnetic field distribution for planar wireless power transfer system," *Radio and Wireless Symposium, RWS '09*, pp. 530-533, 2009.

[18] D. Yinliang, S. Yuanmao, and G. Yougang, "Design of coil structure achieving uniform magnetic field distribution for wireless charging platform," *IEEE Power Electronics Systems and Applications (PESA), 4th International Conference on*, pp. 1-5, 2011.

[19] L. Xun and S. Y. R. Hui, "Optimal design of a hybrid winding structure for planar contactless battery charging platform," *Power Electronics, IEEE Transactions on*, vol. 23, no. 1, pp. 455-463, 2008.

[20] W. S. Lee, H. L. Lee, K. S. Oh, and J. W. Yu, "Uniform magnetic field distribution of a spatially structured resonant coil for wireless power transfer," *Applied Physics Letters*, vol. 100, no. 21, 2012.

[21] B. Minnaert and N. Stevens, "An improved algorithm for the creation of homogeneous magnetic field distributions," *Electromagnetics in Advanced Applications (ICEAA), International Conference on, IEEE*, pp. 517-520, 2015.

[22] M. A. Azpúra, "A semi-analytical method for the design of coil-systems for homogeneous magnetostatic field generation," *Progress In Electromagnetics Research B*, vol. 37, pp. 171-189, 2012.

[23] J. G. Van Bladel, *Electromagnetic Fields*. John Wiley & Sons, 2007.

[24] C. M. Zierhofer and E. S. Hochmair, "Geometric approach for coupling enhancement of magnetically coupled coils," *Biomedical Engineering, IEEE Transactions on*, vol. 43, no. 7, pp. 708-714, 1996.

[25] N. Stevens, "Normalisation of magnetic field distribution generated by circular current loop," *Electronics Letters*, vol. 50, no. 17, pp. 1234-1236, 2014.

[26] Wireless Power Consortium, The Qi Wireless Power Transfer System Power Class 0 Specification, Part 4: Reference Designs, Ver. 1.2.2, 2016.

[27] Wireless Power Consortium, System Description Wireless Power Transfer, vol. 1, Part 1, Ver. 1.0, 2010.

Mutual Coupling Reduction of Closely Spaced MIMO Antenna Using Frequency Selective Surface based on Metamaterials

Mansoor Dashti Ardakani and Reza Amiri

Institut National de la Recherche Scientifique – Énergie Matériaux et Télécommunications
Montréal, QC., H5A 1K6, Canada
Mansoor.Dashti@gmail.com

Abstract ─ A new structure for mutual coupling reduction, which is using the application of Frequency Selective Surface (FSS) based on metamaterials is presented in this paper. In this method, first a custom-designed unitcell is presented that provides a proper S_{12} response for the mutual coupling reduction and then, this unitcell is used in a two-element array of wideband dipoles. According to the results, this unitcell provides a maximum reduction of 15dB in the frequency response of the antenna array,while it does not have a considerable effect on the reflection coefficient and radiation pattern of the antenna. To verify the results, the antenna is fabricated and measured and there is a very good agreement between the simulation and measurement.

Index Terms ─ End-fire antenna, frequency selective surfaces, metamaterial, MIMO antenna, mutual coupling.

I. INTRODUCTION

Today, MIMO antennas are the key elements in modern wireless communication systems, because can they minimize the interference, improve the link quality and channel capacity without the need of increasing the bandwidth. One major drawback in designing MIMO antennas is the interactions of electromagnetic wave between the adjacent elements which degrade the antenna parameters such as bandwidth and radiation pattern. To solve this issue, a lot of works have been carried out to decrease the effect of mutual coupling between antennas such as EBG, DGS, as well as metamaterials [1-5]. The abovementioned techniques have been applied for broadside radiation type. For instance, two inverted–L shaped branches and a rectangular slot with one circular end was etched on the ground plane of a folded monopole antenna, which covers different standards suitable for mobile phone applications [6]. With this proposed technique the mutual coupling is better than 15dB and 20dB in the lower and upper band respectively. However, for some applications it is necessary not to modify the ground plane so as to integrate the antenna element to RF front-end systems. Another approach to minimize the effect of mutual coupling is to integrate arrays of split-ring resonators as a metamaterial inclusion between each adjacent element [7]. Recently, the authors in [8] have presented a compact S-shaped EBG structure to reduce the E-plane mutual coupling between two patch antennas by 15 dB at 5.25 GHz. However, the drawback of this configuration is the use of via which adds a complexity to achieve S-shaped configuration.

The authors in [9] have introduced three interdigital lines that excite the orthogonal polarization mode for reducing the mutual coupling between adjacent patch antennas. With this method the isolation corresponds to -20dB. However, using vias in the interdigital lines adds the complexity to the antenna configuration. Applying a T-shaped slot impedance transformer between two-closely spaced PIFA antennas [10] is another approach with isolation of 19.2 and 22.8 for WLAN and WiMAX frequency band respectively. Utilizing the wall loaded by a coplanar strip and defected split-ring resonator is another viable approach to reduce the mutual coupling between closely distanced patch antennas [11]. However, the presence of the wall makes the antenna structure bulky, which is useless for modern wireless communication systems.

In this paper, we propose a simple structure to suppress the effect of mutual coupling between two planar end-fire dipole antennas. The proposed antenna operates in the wide frequency bandwidth of 1.8-4.2 GHz with edge to edge distance of 2mm.To reduce the interaction between antennas, an array of modified FSS metamaterials [12] is integrated on the back side of the dipole antenna. To verify the results, a prototype of the antenna is fabricated indicating there is a good agreement between the simulation and measurement. The measured isolation between antennas is below -40dB over frequency band of 2.15-3.1 GHz, which makes this structure a good candidate for MIMO antenna applications.

II. UNITCELL LAYOUT

Figure 1 shows the schematic view of the proposed design for the FSS metamaterial unitcell. Compared to

Submitted On: June 23, 2016
Accepted On: June 20, 2017

other structures, this unitcell does not have any vias and it is easy to fabricate. This unitcell is implemented on a Rogers RT/5880 substrate with the effective permittivity of 2.2 and the thickness of 1.575mm.

To calculate the frequency response of the unitcell, it is simulated in the HFSS software using the PEC and PMC walls along X and Z directions and two ports located in the Y direction, and the S parameter results are plotted in Fig. 2.

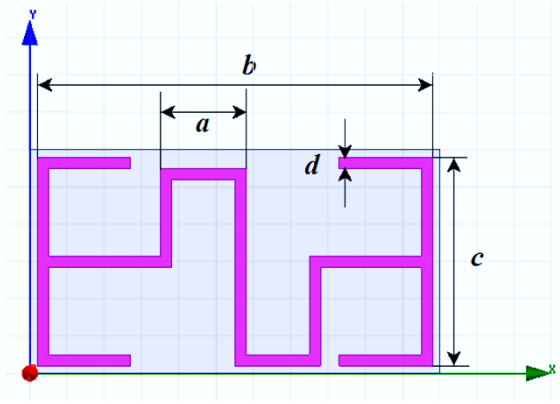

Fig. 1. Schematic view of the unitcell (a=2.3, b=10.6, c=5.6, and d=0.3 mm).

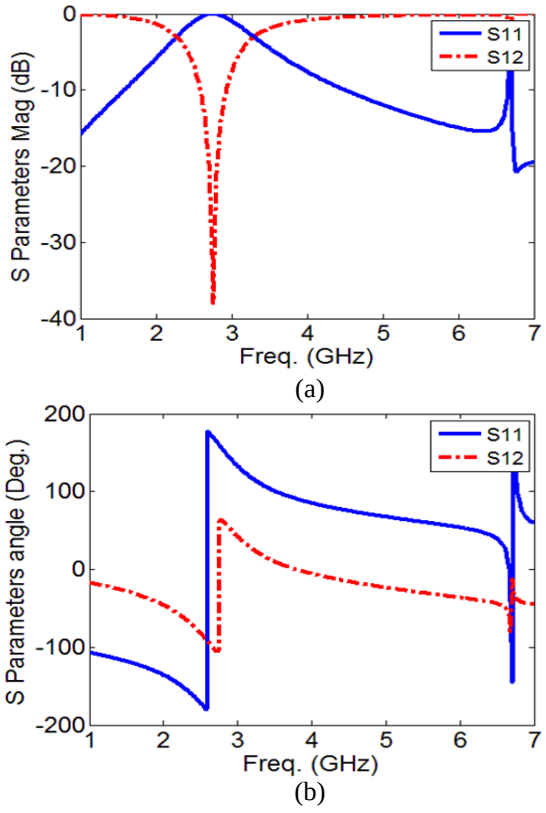

Fig. 2. Simulated S-parameters of the unitcell: (a) magnitude and (b) phase.

According to the results, there is a very deep fall-off in the S_{12} response of the unitcell from 2.28 to 3.30 GHz. As mentioned in the previous section, the final objective of this paper is to apply this unitcell on a planar antenna array structure and use its sharp fall-off as a mutual coupling reduction mechanism.

III. ANTENNA DESIGN

Figure 3 depicts the schematic view of the presented antenna array with the unitcells printed as the mutual coupling reduction elements. The reference antenna is derived from [11] where a special balun structure is used to obtain a wideband result.

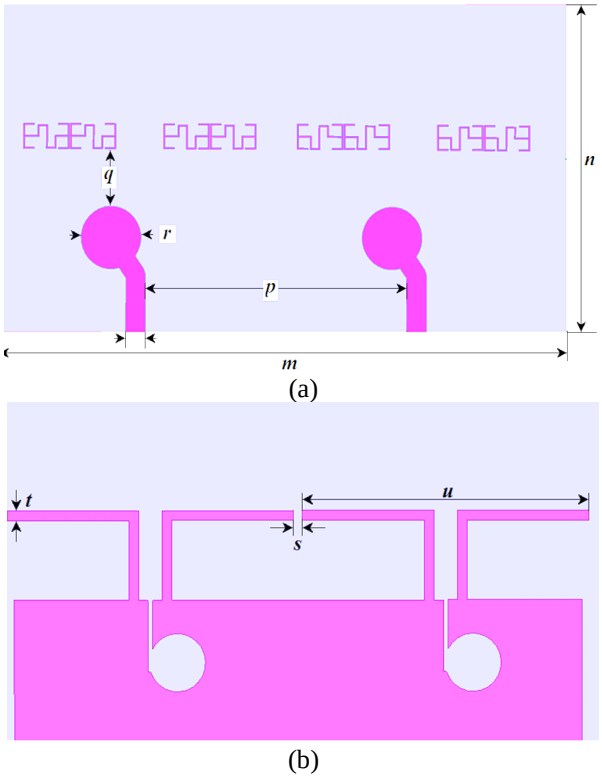

Fig. 3. Schematic view of the antenna with unitcells: (a) top, (b) bottom (dimensions in millimeters are: m=130, n=71.7, p=60.5, q=12.7, r=13.5, s=1.9, t=2, u=63.1).

This two-element antenna array is also implemented on the Rogers RT/5880 substrate with the thickness of 1.575mm. The effect of FSS metamaterial unitcells on the mutual coupling of the antenna is demonstrated in Fig. 4.

According to Fig. 4, a reduction in the S_{12} parameter of the antenna is observed from 1.7 to 3 GHz, the maximum amount of mutual coupling reduction is 15dB, which is achieved at the frequency of 2.45 GHz. The other important feature of the metamaterial inclusions in front of antenna is their negligible effect on the antenna matching as demonstrated in Fig. 5.

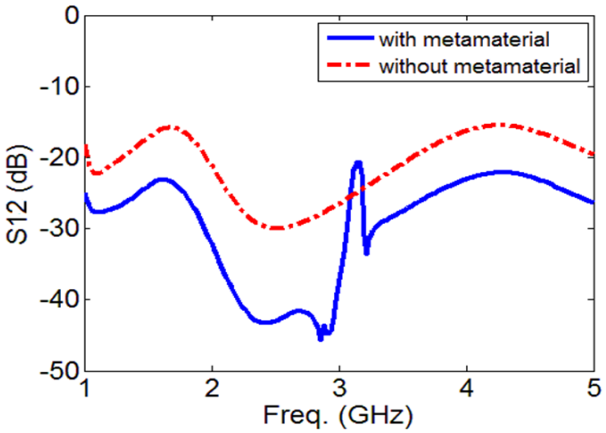

Fig. 4. Simulated S_{12} of the antenna with and without FSS metamaterial.

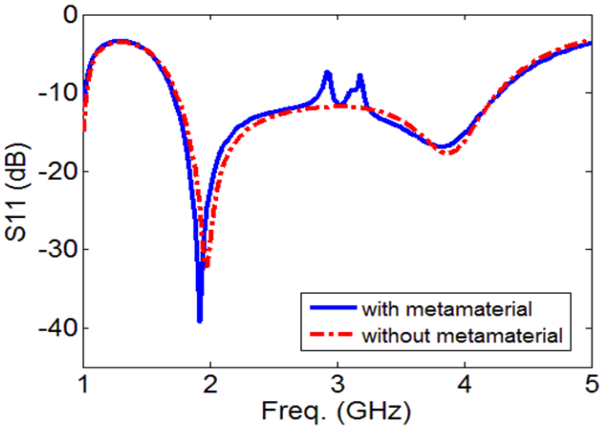

Fig. 5. Reflection coefficient of antenna with and without FSS metamaterial.

According to Fig. 5, the FSS metamaterial loading has no effect on antenna reflection coefficient and the S_{11} parameter is almost the same with and without FSS metamaterial. The antenna gain is 6dB when the unitcells are used which is the same as the antenna with no unitcells.

IV. EXPERIMENTAL RESULTS

To verify the simulation results, the antenna is fabricated and measured. A photograph of the fabricated prototype is shown in Fig. 6.

The measured reflection coefficient of the antenna with the decoupling elements is plotted in Fig. 7, which is in a very close agreement with the simulation results. Moreover, the measured radiation pattern of the fabricated prototype totally complies with the simulation in both E- and H-planes as depicted in Fig. 8.

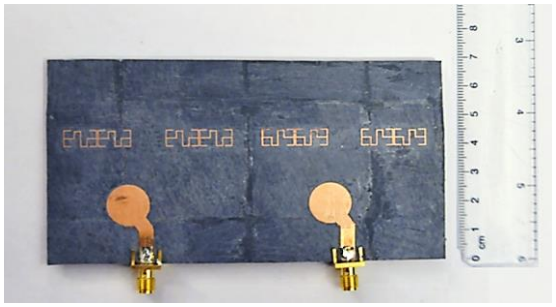

(a)

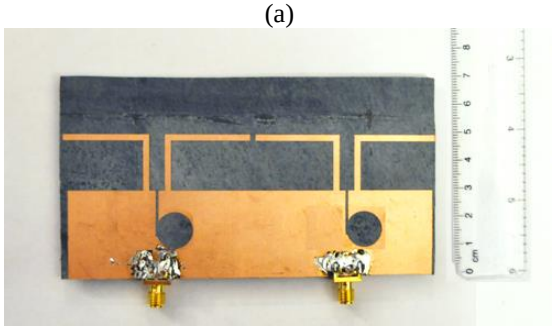

(b)

Fig. 6. The fabricated prototype: (a) top and (b) bottom.

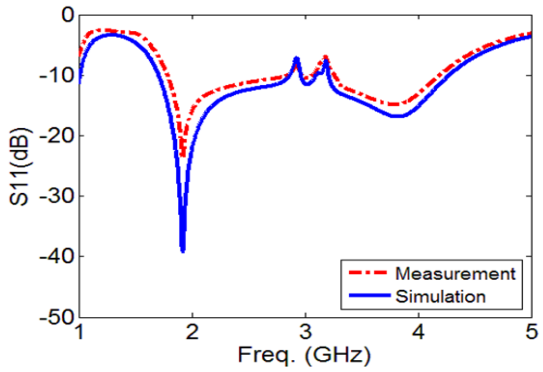

(a)

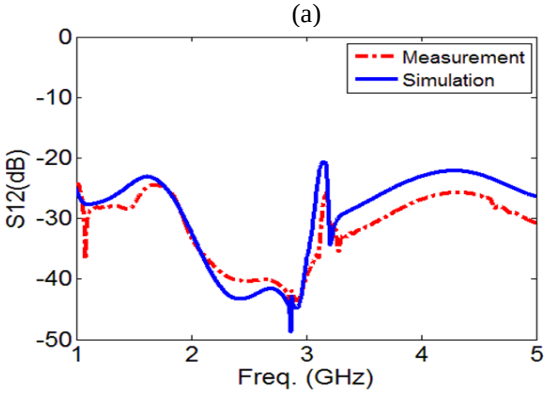

(b)

Fig. 7. Measured S-parameters of the antenna: (a) S_{11} and (b) S_{12}.

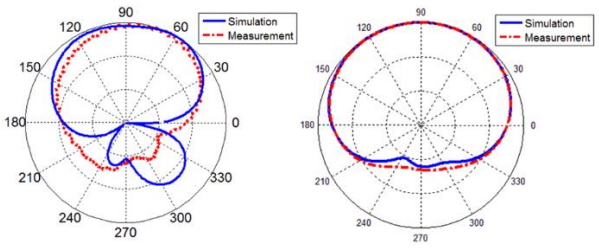

(a) (b)

Fig. 8. Measured radiation pattern at 2.45 GHz: (a) E-plane and (b) H-plane.

V. CONCLUSION

In this paper, a new structure for mutual coupling reduction has been introduced. In this structure, a special FSS metamaterial unitcell has been designed to produce a deep fall-off in the desired frequency range and then the presented unitcell is used in the structure of a planar two-element antenna array. According to the results, the presented technique leads to a reduction of 15dB in the S12 parameter of the antenna array while not affecting the antenna matching and radiation pattern. A prototype of the antenna array with the embedded unitcells is fabricated and the measurement results are very close to the simulation. The presented unitcell provides a simple, low-profile and effective method for mutual coupling reduction of antenna arrays and can be used in modern MIMO applications.

REFERENCES

[1] A. Yu and X. Zhang, "A novel method to improve the performance of microstrip antenna arrays using a dumbbell EBG structure," *IEEE Antennas Wireless Propag. Lett*., vol. 2, pp. 170-172, 2003.

[2] H. S. Farahani, M. Veysi, M. Kamyab, and A. Tadjalli, "Mutual coupling reduction in patch antenna arrays using a UC-EBG superstrate," *IEEE Antennas Wireless Propag. Lett*., vol. 9, pp. 57-59, 2010.

[3] M. M. Bait-Suwailam, O. F. Siddiqui, and O. M. Ramahi, "Mutual coupling reduction between microstrip patch antennas using slotted-complementary split-ring resonators," *IEEE Antennas Wireless Propag. Lett*., vol. 9, pp. 876-878, 2010.

[4] R. Karimian, H. Oraizi, S. Fakhte, and M. Farahani, "Novel F-shaped quad band printed slot antenna for WLAN and WiMax MIMO system," *IEEE Antennas Wireless Propag. Lett*., vol. 12, pp. 405-408, 2013.

[5] R. Karimian, M. Soleimani, and S. M. Hashemi, "Tri-bands four elements MMO antenna system for WLAN and WiMAX application," *Journal of Electromagnetic Wave and Application*, vol. 26, no. 17-18, pp. 2348-2357, 2012.

[6] S. Shoaib, I. Shoaib, N. Shoaib, X. Chen, and C. G. Parini, "Design and performance study of a dual-element multiband printed monopole antenna array for MIMO terminals," *IEEE Antennas Wireless Propag. Lett*., vol. 13, pp. 329-332, 2014.

[7] D. von B. M. Trindade, C. Müller, M. C. F. De Castro, and F. C. C. D. Castro, "Metamaterials applied to ESPAR antenna for mutual coupling reduction," *IEEE Antennas Wireless Propag. Lett*., vol. 14, pp. 430-433, 2015.

[8] A. Veeramani, A. Saee Arezomand, J. Vijayakrishnan, and F. B. Zarrabi, "Compact S-shaped EBG structures for reduction of mutual coupling," *In Advanced Computing & Communication Technologies (ACCT), 2015 Fifth International Conference on, IEEE*, pp. 21-25, 2015.

[9] H. Qi, X. Yin, L. Liu, Y. Rong, and H. Qian, "Improving isolation between closely spaced patch antennas using interdigital lines," *IEEE Antennas Wireless Propag. Lett.*, Early Access.

[10] S. Zhang, B. K. Lau, Y. Tan, Z. Ying, and S. He, "Mutual coupling reduction of two PIFAs with a T-shape slot impedance transformer for MIMO mobile terminals," *IEEE Trans. Antennas Propag*., vol. 60, no. 3, March 2012.

[11] H. Qi, X. Yin, L. Liu, Y. Rong, and H. Qian, "Mutual coupling suppression between two closely spaced microstrip antennas with an asymmetrical coplanar strip wall," *IEEE Antennas Wireless Propag. Lett*., Early Access.

[12] H. Chen, L.-X. Ran, J. T. Huang-Fu, X.-M. Zhang, K. S. Chen, T. M. Grzegorczyk, and J. A. Kong, "Magnetic properties of S-shaped split-ring resonators," *Progress in Electromagnetics Research, PIER*, vol. 51, pp. 231-247, 2005.

Mansoor Dashti Ardakani received his B.Sc. degree in Electrical Engineering from Shiraz University of Technology, Shiraz, Iran in 2009 and M.Sc. degree in Telecommunication Engineering from Iran University of Science and Technology (IUST), Tehran, Iran in 2012. He is presently Ph.D. Student at Institut National de Recherche Scientifique (INRS), Montréal, Canada. His research interests include passive microwave/ millimeter-wave circuit design, wireless, radar, metamaterial and FSS structures.

Reza Amiri received his B.Sc. degree in Electrical Engineering from Concordia University,Montréal, Canada in 2015 and M.Sc. degree in Telecommunication Engineering from Institut National de Recherche Scientifique (INRS), Montréal, Canada in 2017. He is presently Ph.D. Student at Institut National de Recherche Scientifique (INRS), Montréal, Canada. His research interests include passive microwave/millimeter-wave circuit design, wireless, radar Sensors and 5G transceivers.

A Double Modal Parameter Tracking Method To Characteristic Modes Analysis

Qihong He [1], Ziping Gong [1*], Hengyu Ke [1], and Ling Guan [2]

[1] School of Electronic Information
Wuhan University, Wuhan, 430072, China
2012102120001@whu.edu.cn, *zpgong@whu.edu.cn, hysp@whu.edu.cn

[2] Department of Communication Engineering
Nanjing University of Science and Technology, Nanjing, 210094, China
guanling@njust.edu.cn

Abstract ─ Mode tracking plays an important role in characteristic modes analysis. However, mode tracking in a proper and efficient way is still a challenging work. Based on modal linear correlation and modal stability, a double modal parameter tracking method is proposed in this paper, which is to track modes by correlating eigenvector and calculating the stability of characteristic angle simultaneously. To eliminate ambiguity case of multi-mode mapping one mode, two sorted mode with max Pearson correlation coefficient are identified same mode by utilizing saving best function. In order to verify accuracy and efficiency of the proposed method, four representative structures are analyzed. It can be observed that the proposed tracking method works better than the traditional methods.

Index Terms ─ Characteristic modes analysis, double modal parameter tracking method, modal linear correlation, modal stability.

I. INTRODUCTION

The Theory of Characteristic Modes (TCM) was first presented by Garbacz in his doctoral dissertation [1] and then refined by Harrington in 1970s [2, 3]. TCM shows deep insight into the nature feature of an object, which is based on the method of moment (MoM). But researchers originally didn't pay much attention to TCM. As the extreme development of computer, TCM has attracted many researchers' interest now. Applying the CMA, Chen an Wang show a UAV platform integrated pattern reconfigurable antenna [4], and a HF band shipboard antenna [5], where the radiation efficiency has been improved. Using the orthogonality between different modes, many antennas with good isolation in MIMO system have been designed by researchers [6-9] .

CMA is generally performed in spectrum. The same mode at different frequency samples needs to be identified firstly, which is called mode tracking. Mode tracking is the basis of characteristic mode application. However, mode tracking in a proper and efficient way is still a challenging work. There are a few of papers involving mode tracking. The tracking methods in these papers are all only tracking one modal parameter: a) Tracking method in paper [10, 11] is based on tracking eigenvalues. b) Tracking method in paper [12-14] is based on correlating eigenvectors. c)Tracking method in paper [15] is based on correlating modal far-field pattern. Tracking methods in a) and b) are both based on one parameter deriving from generalized eigenvalue equation, and no additional calculation is needed. Therefore, these methods have high computational efficiency. However, they can't deal well with complex structures since mode swapping always exists. Tracking method in c) utilizes stability of far-field pattern to obtain better results than a) and b), but a lot of computation has to be added for calculating far-field.

In this paper, a new tracking method named as double modal parameter tracking method (DMPTM) is proposed, which is based on tracking two modal parameters at the same time.

The remainder of this paper is organized as follows. In Section 2, the theory and the formulations in characteristic modes analysis are given briefly. In Section 3, DMPTM is introduced in detail. Four numerical experiments are presented in Section 4 to show the accuracy and efficiency of the proposed method. Section 5 concludes this paper.

II. BRIEF INTRODUCTION TO CMA

Linear combination of a set of characteristic modes can well approximately represent the solution of an electromagnetic problem. These characteristic modes correspond to the inherent properties of electromagnetic objects and have orthogonality between different modes [2]. For the sake of easy reference, the following paragraphs are a brief introduction to characteristic

Submitted On: January 18, 2017
Accepted On: October 25, 2017

modes analysis.

As presented in [2], characteristic modes can be obtained by solving the following generalized eigenvalue problem:

$$XJ_n = \lambda_n RJ_n, \tag{1}$$

where X and R are imaginary part and real part of impedance matrix Z, which is derived from the well known method of moment (MoM). J_n and λ_n are named as eigencurrents (or eigenvectors), and eigenvalues λ_n represents the radiation or scattering properties of the corresponding modes. If $\lambda_n > 0$, the mode stores magnetic energy. If $\lambda_n < 0$, the mode stores electric energy. And if $\lambda_n = 0$, the mode is at resonance. It is notable that characteristic modes are independent of a specific source or excitation, and only rely on the shape, size, material and working frequency band of the object.

Because of its large range of eigenvalues [12], characteristic angles α_n are introduced as following:

$$\alpha_n = 180^0 - \arctan(\lambda_n). \tag{2}$$

Obviously, the range of values for α_n is from 90^0 to 270^0. If $\alpha_n = 180^0$, the corresponding modes are at resonance.

In theory, the linear combination of infinite modes is needed to describe the electromagnetic properties of the study object. Fortunately, only several mode with small eigenvalues are needed to descript the electromagnetic behavior for electrically small or moderate objects [16].

III. DOUBLE MODAL PARAMETER TRACKING METHOD

In this section, double modal parameters tracking method is presented in detail.

A. Main ideas

Eigenvalues, eigenvectors and characteristic far fields are three main parameters in CMA, and they have different features: The range of values for eigenvalues is $(-\infty, +\infty)$, and they vary fast with frequencies and are easily affected by numerical accuracy, so eigenvalues are not suitable to be tracked. Characteristic far fields are the most stable among modal parameters, so they can be chosen to track mode. However its calculation cost is expensive and its calculation results are also affected by spatial angular step. The eigenvectors stability is between eigenvalues and characteristic far fields, and they are obtained directly through solving generalized eigenvalue equation, so mode tracking based correlating eigenvectors is a balanced choice between efficiency and accuracy.

However, mode tracking based only one modal parameter [10-15] can work well for simple structure, but they can not deal well with complex object.

This paper proposed a double modal parameter tracking method based modal correlation and modal stability. Its main ideas are:

1) Tracked mode satisfying both model correlation requirement and modal stability requirement can be identified to same mode.

2) To eliminate ambiguity situation where multi-modes map one mode, the pair of modes with the max correlation coefficient are mapped to same mode.

B. Modal correlation requirement

Modal correlation requirement is referred that correlation coefficients of same modes at different frequency samples are larger than specified linear correlation threshold. In this paper, linear correlation is measured by Pearson correlation coefficient, its formulation is followed [14]:

$$r_{m,n} = \left| \frac{\sum_{i=1}^{N}(x_i - \bar{x})(y_i - \bar{y})}{\sqrt{\sum_{i=1}^{N}(x_i - \bar{x})^2}\sqrt{\sum_{i=1}^{N}(y_i - \bar{y})^2}} \right|. \tag{3}$$

In formulation (3), $x = (x_1, x_2, \cdots, x_N)^T$ represents m^{th} eigenvector at frequency f_p, $\bar{x}$ represents the mean value of its components. y and $\bar{y}$ represent n^{th} eigenvector and its mean value at frequency f_q respectively, and $p \neq q$.

The range of values for $r_{m,n}$ is [0,1]. It represents that the two eigenvectors are linearity independent if $r_{m,n}$ equals 0, and it represents that the two eigenvectors are linear correlation if $r_{m,n}$ equals 1. Because eigenvectors are function of frequency, the correlation coefficients between same modes vary with frequency change, so a threshold for linear correlation is needed to be specified. According to our experience, the correlation threshold R_g is set to 0.8～0.9, the default value of R_g is 0.8. It means that sorted mode satisfied correlation requirement if their correlation coefficient is larger than R_g.

C. Modal stability requirement

Modal stability requirement is referred that modal parameters of same mode varying with frequencies are smaller than specified stability threshold. Stability is a universal characteristic in macroscopic physics word, so modal stability is inherent feature. In the aforementioned literatures, modal stability hasn't been paid sufficient attention, and the tracking methods in [10-15] don't make use of the modal stability.

In order to measure modal stability, characteristic

angle stability is defined as follows:

$$s = \left|\frac{\Delta\alpha}{\alpha_e}\right| = \left|\frac{\alpha_c - \alpha_e}{\alpha_e}\right|. \quad (4)$$

In formulation (4), α_e represents extrapolated characteristic angle derived from known characteristic angle array, by utilizing Matlab function spline. The α_c represents directly calculated characteristic angle according to formulation (2).

Tracked modes satisfy modal stability requirement if the modal stability of s is smaller than the specified threshold S_g. Because the range of values for characteristic angle is $\left[90^0, 270^0\right]$, so the range of values for *s* is also large. According to our experiences, S_g is set to 0.2∼0.5 which is changed according the complexity of structure. The default value of S_g is 0.5. Figure 1 shows the schematic diagram of modal stability *s*.

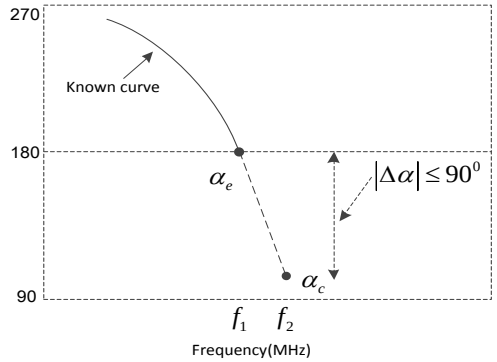

Fig. 1. Schematic diagram of modal stability.

D. The proposed tracking method

The proposed double modal parameter tracking method is divided into three stages: pre-processing stage, mode tracking stage, and post-processing stage.

D1. Pre-processing stage

There are several tasks in the pre-processing stage. Firstly, K eigen-pairs of each frequency, where M frequencies samples are setup at prior, are calculated and ordered in ascending order of eigenvalues. Secondly, Pearson correlation coefficients between eigenvectors of adjacent frequencies are calculated, according to formulation (3). Thirdly, Index-Table array with dimension of $M_{rows} \times K_{columns}$, where each column maps one mode and each row maps one frequency is initialized by its first row filled with $1,2,\cdots,K$ and others are filled with "NaN". The elements of the first row in Index-Table represent the K modes of the first frequency F1, which does not need to be tracked.

The Matlab function corr is used to calculate Pearson correlation coefficient between every eigenvector at frequency F_i and all K eigenvectors at frequency F_{i-1}, resulting in an array with K elements. After calculating correlation coefficients between all eigenvectors at adjacent frequencies, an array with dimension of $M \times M \times K$ will be obtained.

D2. Mode tracking stage

Mode tracking stage consists 4 tracking function: primary tracking function, rescuing function, opening new mode function, and saving best function, as is shown in Fig. 2. Mode tracking start with K eigenvectors at 2nd frequency sample F_2, then K eigenvectors at 3rd frequency sample F_3, until K eigenvector at last frequency sample F_M. The 4 tracking function will be performed at these frequencies except that primary tracking function, opening new mode function and saving best function are performed at 2nd frequency sample F_2.

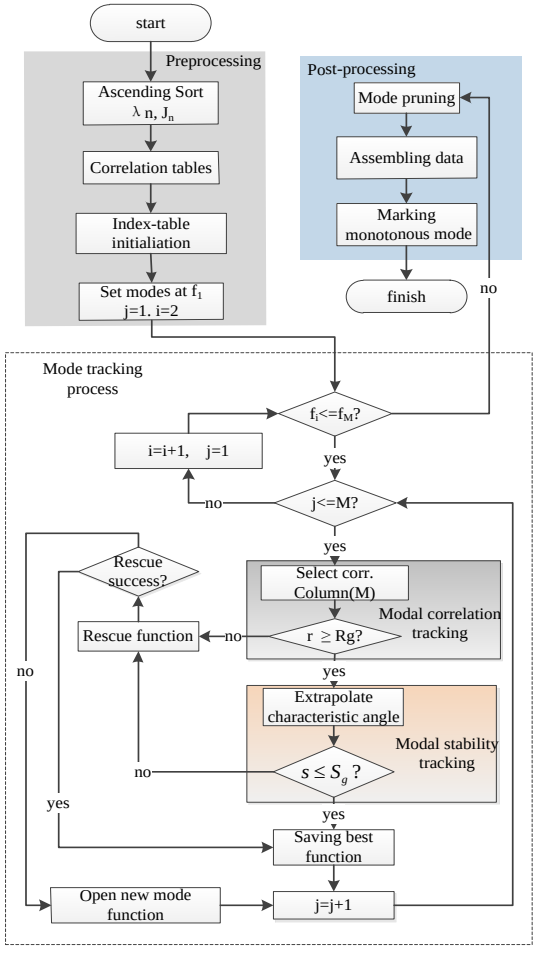

Fig. 2. Flow chart of proposed double modal parameter tracking method.

D2.1. Primary tracking function

Firstly, one determines whether there is any correlation coefficient between the j^{th} eigenvector at F_i (called current mode) and K eigenvectors at F_{i-1} larger than R_g . If there is none of them, tracking process comes to rescuing function. And if there is any, tracking process comes to extrapolate characteristic angle. This is called modal correlation tracking. Then tracking process comes to determine whether the modal stability coefficient is smaller than S_g. If the modal stability requirement is satisfied too, tracking process comes to saving best function, and if not, tracking process comes to rescue function again. This is called modal stability tracking.

D2.2. Rescuing mode function

Firstly, for the sake of convenience, the indicator of previous frequency sample is set as $p = i - 2$. Secondly, Pearson correlation coefficients between current eigenvector and K eigenvectors at previous frequency are calculated. Thirdly, modal correlation tracking and modal stability tracking are performed. If both modal correlation tracking and model stability tracking are successful, then rescuing function success, and tracking process comes to saving best function, otherwise tracking process comes to opening new mode function.

D2.3. Opening new mode function

The method of opening new mode function is similar to the one in paper [12]. It is to add a new column at right side of the last column of current Index-Table array. The i^{th} element of the new added column is filled with mode index, and the other elements are filled with "NaN", as is shown in Fig. 3.

D2.4. Saving best function

If tracking process comes to saving best function, it means that both modal correlation requirement and modal stability requirement are satisfied. Without loss of generality, we suppose that j^{th} eigenvector at frequency F_i (called current mode) and m^{th} eigenvector at frequency F_{i-1} do so, and suppose that the mode index of m at frequency F_{i-1} (called previous mode) is kept at 2^{nd} column in Index-Table, as is shown in Fig. 3. If the element of 2^{nd} column corresponding frequency F_i is "NaN", it will be directly replaced by the mode index j. Otherwise, supposing the element is "h", it means that the h^{th} eigenvector at frequency F_i (called kept mode) has been mapped to previous mode. This scenario is known as the ambiguity case of multi-mode mapping one mode. In order to eliminate ambiguity case, one needs to compare the correlation coefficient between current mode and previous mode with the correlation coefficient between kept mode and previous mode, then choose the pair of modes with larger correlation coefficient to map into same mode. Then the failed mode (mode h in Fig. 3.) in competing will be opened new mode if saving best function is performed in rescuing function, or will be put into rescuing function if saving best function is performed in primary tracing function.

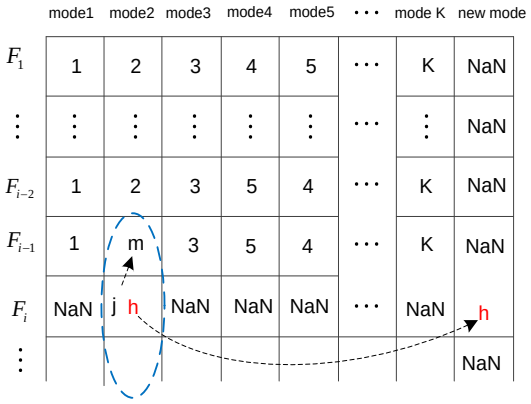

Fig. 3. Example of saving best function and opening new mode function.

D3. Post-processing

There are three works during post-processing in this paper, which are pruning Index-Table array, assembling data of eigen-pairs and marking monotonous modes. These three works are similar to the works in paper [12], it will be briefly described here.

Firstly, pruning Index-Table array means that columns with number of non-nan elements less than three will be cut off.

Secondly, assembling data of eigen-pairs means that the remaining modes in Index-Table after pruning are subsequently fulfilled with the real eigenvalues and eigenvectors, which are corresponding to mode index in Index-Table array.

Lastly, monotonous modes means that the modes with negligible meaning within the computed frequency band. It implies that characteristic angle of monotonous modes is smaller than 110^0 or larger than 250^0 within the computed frequency band. So the last work is to find out the index of monotonous modes.

IV. NUMERICAL RESULTS

In this section, four examples are presented to demonstrate the capability of the proposed method, the material in each example is perfect conductor, and the same triangle meshes are used for different tracking methods in each example.

A. Mode tracking of rectangular plate

The first example is a rectangular plate with size of 120×60 mm^2, as is shown in Fig. 4. The whole structure is divided into 798 triangles, resulting in 1158 RWG basis functions. The computed frequency band is from 1 GHz to 4 GHz with 0.1 GHz frequency step, and 6 eigen-pairs are required at each frequency sample, and R_g is 0.8 and S_g is 0.5.

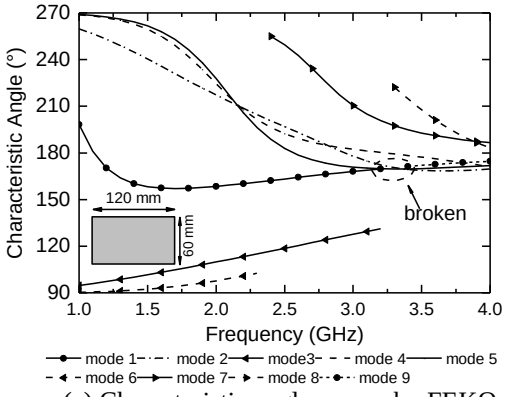

(a) Characteristic angle curves by FEKO

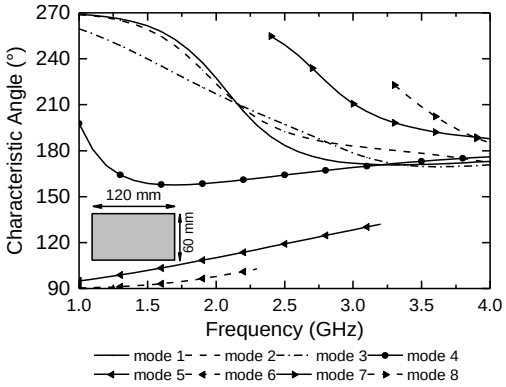

(b) Characteristic angle curves by DMPTM

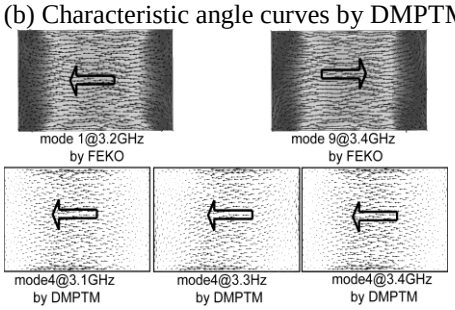

(c) Modal current distribution (big arrows indicate the direction of each model current)

Fig. 4. Characteristic angle curves and modal current distribution of metal rectangular plate.

Figure 4 (a) shows the tracking result by FEKO, and Fig. 4 (b) shows the tracking result by proposed method. It can be seen that the characteristic angle curves are similar except that the order of the modes is different. However, there are still obviously differences between them:

a) The FEKO gives 9 characteristic angle curves for different modes. However the DMPTM gives 8 characteristic angle curves for different modes.

b) The characteristic angle curve of mode 1 in Fig. 4 (a) is closed at 3.2 GHz, and mode 9 is opened at 3.4 GHz. However, the characteristic angle curve of mode 4 in Fig. 4 (b), which corresponds the characteristic angle curve of mode 1 in Fig. 4 (a), is continuous in the entire analysis frequency band.

In order to check tracking results, the mode current distribution is shown in Fig. 4 (c). It is found that the current distribution of mode 1 at 3.2 GHz is the similar to that of mode 9 at 3.4 GHz, which are tracked by FEKO, so they should be the same mode. In contrast, the mode current distribution of mode 4 tracked by DMPTM is similar at 3.1 GHz, 3.3 GHz and 3.4 GHz, so they are the same mode. Therefore, the proposed method in this paper gives the correct tracking results.

B. Mode tracking of Minkowski fractal structure

The second example is Minkowski fractal structure with outer size of 71.3×71.3 mm^2, as is shown in Fig. 5. The whole structure is divided into 664 triangles, resulting in 856 RWG basis functions. The computed frequency band is from 2.1 GHz to 2.8 GHz with 10 MHz frequency step, and 6 eigen-pairs are required at each frequency sample, and R_g is 0.8 and S_g is 0.5.

Figure 5 (a) shows the tracking result by FEKO, Fig. 5 (b) shows the tracking result by proposed method, Fig. 5 (c) shows the local enlargement of Fig. 5 (a), and Fig. 5 (d) shows the local enlargement of Fig. 5 (b). Characteristic angle cures in Fig. 5 (a) are very similar to the curves in Fig. 5 (b) except different mode order. It is can been seen from Fig. 5 (c) and Fig. 5 (d) that, there are 2 swapping modes and 2 non-continuous behaviors in Fig. 5 (a), but there are none of them in Fig. 5 (b). This is due to modal stability tracking in the double modal parameters tracking method. Therefore, the proposed tracking method in this paper gives better results than FEKO does in this example.

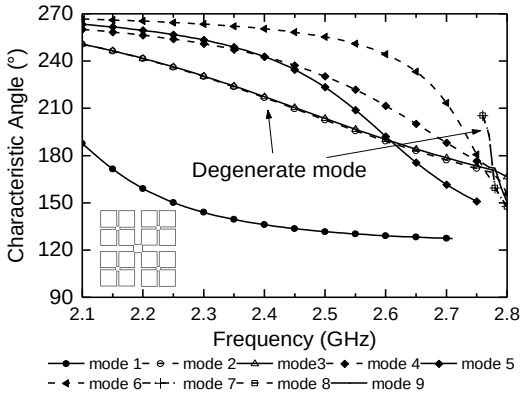

(a) Characteristic angle curves by FEKO

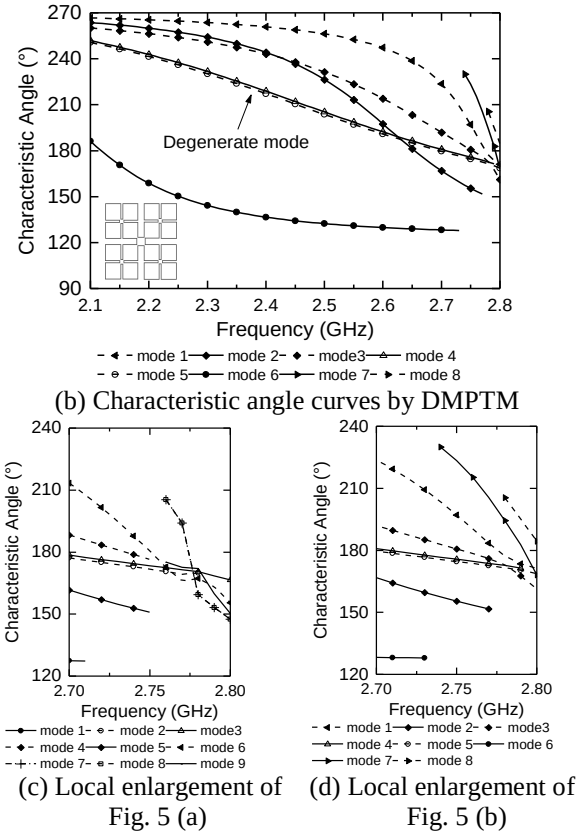

(b) Characteristic angle curves by DMPTM

(c) Local enlargement of Fig. 5 (a)

(d) Local enlargement of Fig. 5 (b)

Fig. 5. Characteristic angle curves of Minkowski fractal structure.

C. Mode tracking of open cavity structure

The third example is open complex cavity structure. The structure is an embedded conformal omni-directional antenna without any feed [17], as is shown in Fig. 6. In the metal cavity of diameter 138.0 mm and height 45.0 mm, there are narrow circular rings with a width 7.0 mm and a wide circular ring with width 40.0 mm. The two rings are located on aperture plane of the cavity. There is one shorting post connecting narrow circular ring and bottom of the cavity at 0^0 and 180^0 respectively, and there is one shoring post connecting wide circular ring and the bottom of the cavity at 90^0 and 270^0 respectively. The four shorting posts form eight "T" junctions.

The whole structure is divided into 1289 triangles, resulting in 1834 RWG basis functions. The computed frequency band is from 0.4 GHz to 0.7 GHz with 10 MHz frequency step, and 6 eigen-pairs are required at each frequency sample, and R_g is 0.8 and S_g is 0.5.

Figure 6 (a) shows the tracking result by FEKO, Fig. 6 (b) shows the tracking result by proposed method, Fig. 6 (c) shows the local enlargement of Fig. 6 (a), and Fig. 6 (d) shows the local enlargement of Fig. 6 (b). It can be seen that characteristic angle cures in Fig. 6 (a) are also very similar to curves in Fig. 6 (b) except different mode order. As is pointed in Fig. 6 (a) and Fig. 6 (b), both of them well identify two pairs of degenerate mode. However, the curves of mode 5 and mode 6 in Fig. 6 (c) are broken at 0.67 GHz, resulting that two additional curves of mode 7 and mode 8 are opened at 0.68 GHz. So, there are 2 non-continuous behaviors in Fig. 6 (a), but there are none of them in Fig. 6 (b).

Therefore, proposed tracking method gives better results than FEKO does in this example. This is also due to the double modal parameter tracking method.

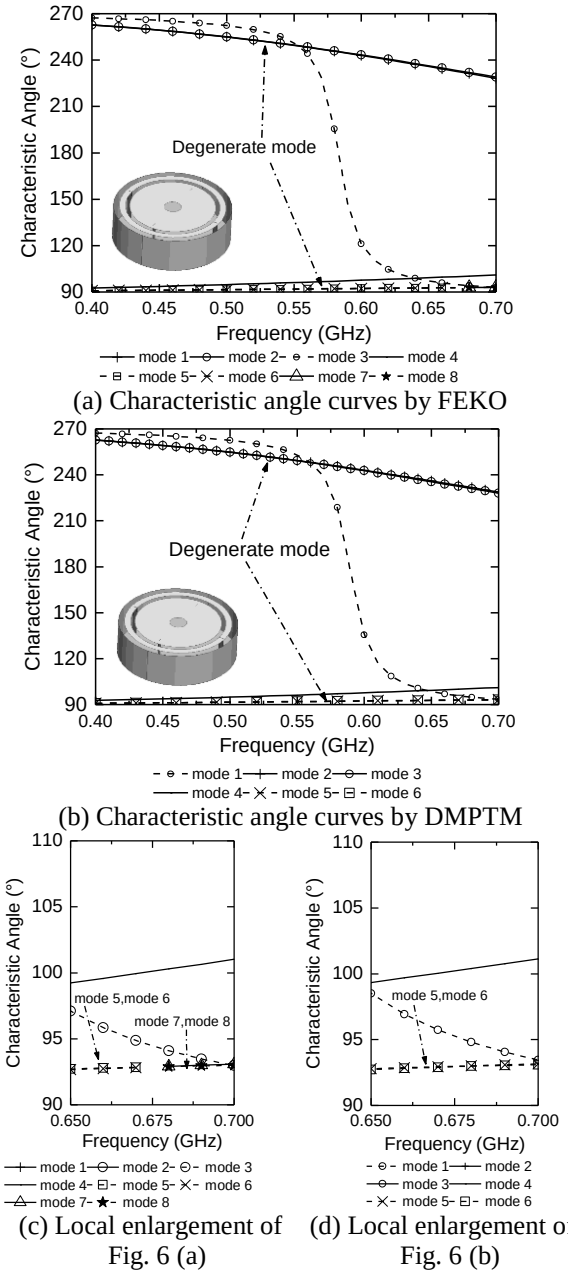

(a) Characteristic angle curves by FEKO

(b) Characteristic angle curves by DMPTM

(c) Local enlargement of Fig. 6 (a)

(d) Local enlargement of Fig. 6 (b)

Fig. 6. Characteristic angle curves of open cavity structure.

D. Mode tracking of a plane

The fourth example is an approximate model of commercial plane A320, which is with body length of 37 m and wingspan size of 39 meters.

The whole structure is divided into 4180 triangles, resulting in 6270 RWG basis functions. The computed frequency band is from 5 MHz to 11 MHz with 0.2 MHz frequency step, and 6 eigen-pairs are required at each frequency sample, and R_g is 0.8 and S_g is 0.2.

Figure 7 (a) shows the tracking result by FEKO, Fig. 7 (b) shows the tracking result by tracking method based on correlating eigenvector, and Fig. 7 (c) shows the tracking result by proposed method. In this example, the three figures show completely different results: there are 4 swapping modes and 2 non-continuous behaviors in Fig. 7 (a), and there are 2 swapping modes and 2 non-continuous behaviors in Fig. 7 (b), but there are none of them in Fig. 7 (c). Therefore, the proposed tracking method gives better results than FEKO and tracking method based correlating eigenvector.

Table 1 shows the detailed comparison of the proposed tracking method and FEKO, including the number of non-continuous behavior and the number of mode swapping. From Table 1, it can be seen that there is no non-continuous behavior and mode swapping for DMPTM in the four examples, but there are some for FEKO in these examples. Therefore, the proposed tracking method gives more correct tracking results than FEKO does.

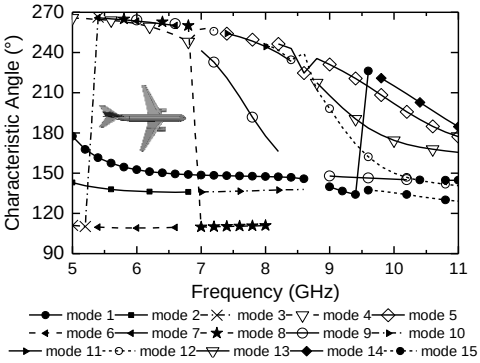

(a) Characteristic angle curves by FEKO

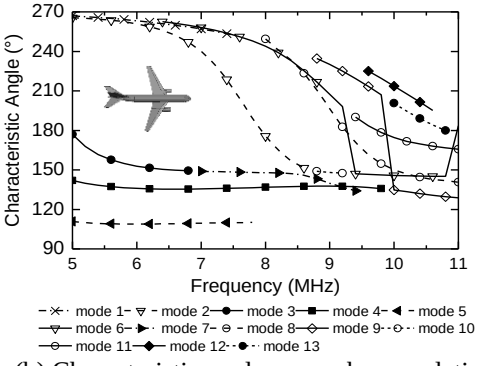

(b) Characteristic angle curves by correlating eigenvector

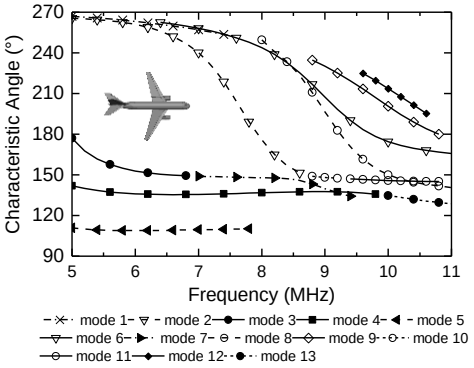

(c) Characteristic angle curves by DMPTM

Fig. 7. Characteristic angle curves of A320.

Table 1: Comparison of DMPTM and FEKO

Numeric Example	Number of Mode Swapping		Number of Non-continuous Behavior	
	FEKO	DMPTM	FEKO	DMPTM
Rectangular plate	0	0	1	0
Minkowski fractal structure	2	0	2	0
Open cavity structure	0	0	2	0
A320	4	0	2	0

V. CONCLUSION

In this paper, a double modal parameter tracking method (DMQTM) is proposed, which tracks modes based correlating eigenvectors and calculating the stability of characteristic angle simultaneously. In order to eliminate ambiguity case, saving best function is introduced. To verify accuracy and efficiency of the proposed DMQTM, four examples are analyzed by FEKO, tracking method based on correlating eigenvector and proposed method respectively. The numerical results demonstrate that the proposed method efficiently gives more accurate mode tracking curves than traditional tracking method does. In order to find out the exact resonant frequency for characteristic mode, our future work is to add adaptive frequency.

ACKNOWLEDGMENT

This work was supported in part by National Natural Science Foundation of 61331012, 61371197, and 41333106 in China.

REFERENCES

[1] R. J. Garbacz, "A Generalized Expansion for Radiated and Scattered Fields," Ph.D., Ohio State University, 1968.

[2] R. Harrington and J. Mautz, "Theory of characteristic modes for conducting bodies," *Antennas and*

Propagation, IEEE Transactions on, vol. 19, pp. 622-628, 1971.

[3] R. F. Harrington, J. R. Mautz, and C. Yu, "Characteristic modes for dielectric and magnetic bodies," *Antennas and Propagation, IEEE Transactions on*, vol. 20, pp. 194-198, 1972.

[4] C. Yikai and W. Chao-Fu, "Synthesis of platform integrated antennas for reconfigurable radiation patterns using the theory of characteristic modes," in *Antennas, Propagation & EM Theory (ISAPE), 2012 10th International Symposium on*, pp. 281-285, 2012.

[5] C. Yikai and C.-F. Wang, "Shipboard NVIS radiation system design using the theory of characteristic modes," in *2014 International Symposium on Antennas and Propagation and USNC-URSI Radio Science Meeting*, 2014.

[6] A. Araghi and G. Dadashzadeh, "Oriented design of an antenna for MIMO applications using theory of characteristic modes," *Antennas and Wireless Propagation Letters, IEEE*, vol. 11, pp. 1040-1043, 2012.

[7] A. Krewski, W. L. Schroeder, and K. Solbach, "Multi-band 2-port MIMO LTE antenna design for laptops using characteristic modes," in *Antennas and Propagation Conference (LAPC), 2012*, Loughborough, pp. 1-4, 2012.

[8] Z. Miers, L. Hui, and L. Buon Kiong, "Design of multi-antenna feeding for MIMO terminals based on characteristic modes," in A*ntennas and Propagation Society International Symposium (APSURSI), 2013 IEEE*, pp. 182-183, 2013.

[9] P. Miškovský and A. v. Arbin, "Evaluation of MIMO handset antennas with decorative metal elements using characteristic modes," in *2014 International Symposium on Antennas and Propagation and USNC-URSI Radio Science Meeting*, 2014.

[10] D. J. Ludick, J. v. Tonder, and U. Jakobus, "A hybrid tracking algorithm for characteristic mode analysis," 2013.

[11] E. Safin and D. Manteuffel, "Advanced eigenvalue tracking of characteristic modes," *IEEE Transactions on Antennas and Propagation*, vol. 64, pp. 2628-2636, 2016.

[12] M. Capek, P. Hazdra, P. Hamouz, and J. Eichler, "A method for tracking characteristic numbers and vectors," in *Electromagnetics Research B*, pp. 115-134, 2011.

[13] B. D. Raines and R. G. Rojas, "Wideband characteristic mode tracking," I*EEE Transactions on Antennas and Propagation*, vol. 60, no. 7, pp. 3537-3541, 2012.

[14] D. J. Ludick, U. Jakobus, and M. Vogel, "A tracking algorithm for the eigenvectors calculated with characteristic mode analysis," presented at *The 8th European Conference on Antennas and Propagation (EuCAP 2014)*, 2014.

[15] Z. Miers and B. K. Lau, "Wide band characteristic mode tracking utilizing far-field patterns," *IEEE Antennas and Wireless Propagation Letters*, 2015.

[16] B. D. Raines, "Systematic Design of Multiple Antenna Systems Using Characteristic Modes," Ph.D., Philosophy in the Graduate School of the Ohio State University, The Ohio State University, 2011.

[17] H. Qihong, G. Ziping, K. Hengyu, and W. Xianrong, "An embedded omnidirectional conformal antenna based on theory of characteristic modes," *Journal of Electronics & Information Technology*, vol. 38, pp. 2977-2981, 2016.

Analysis of Transient Scattering from a PEC Coated with Thin Dispersive Dielectric Layer

Y. L. Hu [1], Q. S. Man [1], D. Z. Ding [2], and R. S. Chen [2]

[1] The 28th Research Institute of China Electronics Technology Group Corporation, Nanjing, 210007, China

[2] Nanjing University of Science and Technology, Nanjing, 210094, China
dzding@njust.edu.cn

Abstract ─ A marching-on-in-time (MOT) based time domain thin dielectric sheet (TDS) method is proposed for analyzing the transient electromagnetic scattering from the perfect electrically conducting (PEC) body coated with thin dispersive material. The sources in the thin dielectric layer are all replaced by the current densities of PEC. A recursive convolution method is utilized to deal with the dispersive properties. The performance of accuracy and stability are investigated numerically.

Index Terms ─ Dispersive dielectric, marching-on-in-time, thin dielectric sheet, transient electromagnetic scattering.

I. INTRODUCTION

Analysis of transient electromagnetic scattering from the thin dispersive dielectric coated perfect electrically conducting (PEC) has been paid considerable attention due to its wide range of applications. For instance, thin dispersive dielectric materials are often utilized to reduce radar cross section (RCS) in military. Many numerical methods are available for such analysis accurately. Compared with differential equation method, time domain integral equation (TDIE) method is a better way for open domain transient scattering analysis because the truncated boundary condition is needless. For the coated PEC structure, time domain volume-surface integral equation (TD-VSIE) [1]-[3] and time domain surface integral equation (TD-SIE) [4]-[5] are both valid. However, both methods will consider the unknowns of dielectric materials, and with the increasing electrical size of target, the available computational resource will be swamped quickly, which is troublesome. When the thickness of the coated dielectric layer is thin enough (in the third part, several numerical results are proposed to demonstrate that reasonable accuracy can be achieved when the thickness of the dielectric is less than 0.09 wavelength at the highest frequency of the incident wave), the TDS approximation is a remarkable choice, all the sources in the thin dielectric coated on the closed PEC part are represents in the terms of current densities on PEC surface. The unknowns of the dielectric parts can be saved, and its efficiency has been proven [6]-[11].

In this paper, a modified MOT based approximation time domain TDS method is proposed. Compare with the conventional method presented in [11], which can only be used to compute the non-dispersive medium. The proposed method extended the applied range to analyze the transient electromagnetic scattering problems from thin dispersive material coated PEC structure. The practicality of the time domain TDS method is improved. Rao-Wilton-Glisson (RWG) basis function and time shifted Lagrange interpolant are chosen for the expansion in space and time domain. The sources in the thin dispersive material layer are all replaced by the current densities on PEC surface, so the spatial unknowns can be only considered on PEC surface. With the number of unknowns reduced markedly, the computational resource will also be saved. Here, a recursive convolution scheme [12] is introduced to handle the dispersive relationship efficiently. The investigation of performance for the proposed scheme is given in numerical results.

This paper is organized as follows. In Section II, the basic theory and formulations of time domain TDS method are presented. Several numerical results are given to demonstrate the accuracy, stability and efficiency of the proposed method in Section III. Conclusions are summarized in Section IV.

II. THEORY AND FORMULATIONS

Consider a transient incident wave $\mathbf{E}^{\text{inc}}(\mathbf{r},t)$ illuminate upon an arbitrarily shaped closed PEC structure coated with an isotropic, nonmagnetic and dispersive thin dielectric layer. The geometry of the

Submitted On: October 7, 2016
Accepted On: October 4, 2017

composite structures is shown in Fig. 1.

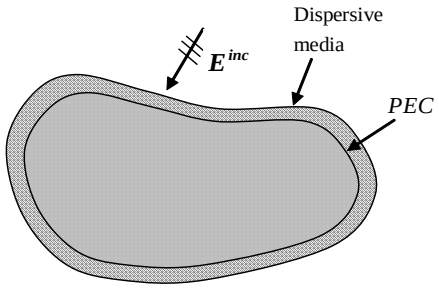

Fig. 1. Geometry of composite structure.

Enforcing the boundary condition on PEC surface *S*, time domain electric field integral equation can be expressed as:

$$\left[\mathbf{E}^{\text{inc}}(\mathbf{r},t)+\mathbf{E}^{\text{sca}}(\mathbf{r},t)\right]_{\tan}=0 \quad \mathbf{r}\in S. \tag{1}$$

Here, the time domain scattering electric field $\mathbf{E}^{\text{sca}}(\mathrm{r},t)$ can be expressed as [11]:

$$\begin{aligned}\mathbf{E}^{sca}(\mathbf{r},t)&=\mathbf{E}^{sca}_{pec}(\mathbf{r},t)+\mathbf{E}^{sca}_{die}(\mathbf{r},t)\\&=-\frac{\mu_0}{4\pi}\frac{\partial}{\partial t}\int_S\frac{\mathbf{J}_s(\mathbf{r}',t-R/c)}{R}ds'-\frac{1}{4\pi\varepsilon_0}\nabla\int_S\frac{\rho_s(\mathbf{r}',t-R/c)}{R}ds'\\&-\frac{\mu_0}{4\pi}\frac{\partial}{\partial t}\int_V\frac{\mathbf{J}_{pol}(\mathbf{r}',t-R/c)}{R}dv'\\&-\frac{1}{4\pi\varepsilon_0}\nabla\left[\begin{array}{l}\int_S\frac{\rho_{pol,down}(\mathbf{r}',t-R/c)}{R}ds'\\+\int_{S^\Delta}\frac{\rho_{pol,up}(\mathbf{r}',t-R/c)}{R}ds^{\Delta\prime}\end{array}\right],\end{aligned} \tag{2}$$

where $\mathbf{E}^{sca}_{pec}$ and $\mathbf{E}^{sca}_{die}$ denote the scattering field generated from PEC and dispersive dielectric, respectively. S^Δ is the upper surface of dielectric, *V* is the volume element of dielectric. $\mathbf{J}_s$ and ρ_s are the surface current and charge on the conductor. ρ_{pol} and $\mathbf{J}_{pol}$ are polarization charge and current of the dielectric layer, respectively.

The relationship between $\mathbf{J}_s$ and ρ_s on the conductor can be deduced from the current continuity condition as:

$$\rho_s(\mathbf{r},t)=-\int_{-\infty}^{t}\nabla\cdot\mathbf{J}_s(\mathbf{r},t')dt' \quad \mathbf{r}\in S. \tag{3}$$

As shown in Fig. 2, the relationship between $\mathbf{J}_{pol}$ and ρ_{pol} at the boundary of different materials can be expressed as:

$$\left[\mathbf{J}_{pol,1}(\mathbf{r},t)-\mathbf{J}_{pol,2}(\mathbf{r},t)\right]\cdot\mathbf{n}(\mathbf{r})=-\partial_t\rho_{pol}(\mathbf{r},t). \tag{4}$$

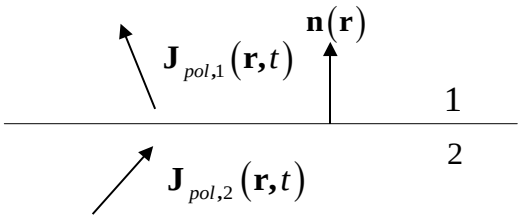

Fig. 2. The interface between two different materials.

If the part 1 is dielectric domain, and part 2 is PEC domain, (4) could change to:

$$\mathbf{J}_{pol}(\mathbf{r},t)\cdot\mathbf{n}(\mathbf{r})=-\partial_t\rho_{pol,down}(\mathbf{r},t). \tag{5}$$

Similarly, if the part 1 is free space, part 2 is dielectric domain, we have that,

$$\mathbf{J}_{pol}(\mathbf{r},t)\cdot\mathbf{n}(\mathbf{r})=\partial_t\rho_{pol,up}(\mathbf{r},t). \tag{6}$$

In the volume of dispersive dielectric, we have:

$$\begin{aligned}\mathbf{J}_{pol}(\mathbf{r},t)&=\partial_t\mathbf{D}(\mathbf{r},t)-\varepsilon_0\partial_t\mathbf{E}(\mathbf{r},t)\\&=\partial_t\mathbf{D}(\mathbf{r},t)-\varepsilon_0\partial_t\left[\gamma(t)\otimes\mathbf{D}(\mathbf{r},t)\right],\end{aligned} \tag{7}$$

where $\mathbf{D}$ denotes the electric flux density. $\gamma(t)$ is the medium susceptibility and defined in [12]. Substituting the normal boundary condition on PEC surface:

$$\mathbf{n}(\mathbf{r})\cdot\mathbf{D}(\mathbf{r},t)=\rho_s(\mathbf{r},t), \tag{8}$$

to (7) and utilizing the relationship between $\mathbf{J}_s$ and ρ_s mentioned in (3), the relationship between $\mathbf{J}_{pol}$ and $\mathbf{J}_s$ can be obtained as:

$$\begin{aligned}\mathbf{J}_{pol}(\mathbf{r},t)&=-\left[\nabla\cdot\mathbf{J}_s(\mathbf{r},t)\right]\cdot\mathbf{n}(\mathbf{r})\\&+\varepsilon_0\left\{\gamma(t)\otimes\left[\nabla\cdot\mathbf{J}_s(\mathbf{r},t)\right]\right\}\cdot\mathbf{n}(\mathbf{r})\end{aligned}. \tag{9}$$

Utilizing the relationship of (9) to (5) and (6), $\rho_{pol}(\mathbf{r},t)$ is then obtained by following equations:

$$\begin{aligned}\rho_{pol,down}(\mathbf{r},t)&=\int_{-\infty}^{t}\left[\nabla\cdot\mathbf{J}_s(\mathbf{r},t')\right]dt'\\&-\varepsilon_0\left\{\gamma(t)\otimes\left[\int_{-\infty}^{t}\nabla\cdot\mathbf{J}_s(\mathbf{r},t')dt'\right]\right\}\end{aligned}, \tag{10}$$

$$\begin{aligned}\rho_{pol,up}(\mathbf{r},t)&=-\int_{-\infty}^{t}\left[\nabla\cdot\mathbf{J}_s(\mathbf{r},t')\right]dt'\\&+\varepsilon_0\left\{\gamma(t)\otimes\left[\int_{-\infty}^{t}\nabla\cdot\mathbf{J}_s(\mathbf{r},t')dt'\right]\right\}\end{aligned}. \tag{11}$$

According to the TDS theory, the sources of thin dispersive materials are all replaced by the current densities of PEC surface. Substituting (2), (9), (10) and (11) to (1), TD-EFIE can be converted to:

$$\left\{\begin{array}{l}\dfrac{\mu_0}{4\pi}\int_S \dfrac{\partial_t \mathbf{J}_s(\mathbf{r},t-R/c)}{R}ds-\dfrac{1}{4\pi\varepsilon_0}\nabla\int_S\int_{-\infty}^{t-R/c}\dfrac{\nabla\cdot\mathbf{J}_s(\mathbf{r},t')}{R}dt'ds\\ +\dfrac{\mu_0}{4\pi}\int_V\left\{\begin{array}{l}\dfrac{-\partial_t\left[\nabla\cdot\mathbf{J}_s(\mathbf{r},t-R/c)\right]}{R}\\ +\dfrac{\varepsilon_0\partial_t\left\{\gamma(t)\otimes\left[\nabla\cdot\mathbf{J}_s(\mathbf{r},t-R/c)\right]\right\}}{R}\end{array}\right\}\cdot\mathbf{n}(\mathbf{r})dv\\ +\dfrac{1}{4\pi\varepsilon_0}\nabla\int_S\int_{-\infty}^{t-R/c}\dfrac{\nabla\cdot\mathbf{J}_s(\mathbf{r},t')}{R}dt'ds\\ -\dfrac{1}{4\pi}\nabla\int_S\dfrac{\left\{\gamma(t)\otimes\left[\int_{-\infty}^{t-R/c}\nabla\cdot\mathbf{J}_s(\mathbf{r},t')dt'\right]\right\}}{R}ds\\ -\dfrac{1}{4\pi\varepsilon_0}\nabla\int_{S^\Delta}\int_{-\infty}^{t-R/c}\dfrac{\nabla\cdot\mathbf{J}_s(\mathbf{r},t')}{R}dt'ds^\Delta\\ +\dfrac{1}{4\pi}\nabla\int_{S^\Delta}\dfrac{\left\{\gamma(t)\otimes\left[\int_{-\infty}^{t-R/c}\nabla\cdot\mathbf{J}_s(\mathbf{r},t')dt'\right]\right\}}{R}ds^\Delta\end{array}\right\}_{\tan}$$
$$=\mathbf{E}^{inc}_{\tan}(\mathbf{r},t). \tag{12}$$

Here, the recursive convolution scheme [12] is applied. In order to solve (12) conveniently, a new parameter $\mathbf{P}(\mathbf{r},t)$ is defined as:

$$\mathbf{P}(\mathbf{r},t)=\gamma(t)\otimes\mathbf{J}_s(\mathbf{r},t). \tag{13}$$

Now, $\mathbf{P}(\mathbf{r},t)$ and $\mathbf{J}_S(\mathbf{r},t)$ are expanded with spatial and temporal basis functions as follows:

$$\mathbf{P}(\mathbf{r},t)=\sum_{n=1}^{N_S}\sum_{j=1}^{N_t}P_{j,n}T_j(t)\mathbf{f}_n^s(\mathbf{r}). \tag{14}$$

$$\mathbf{J}_s(\mathbf{r},t)=\sum_{n=1}^{N_S}\sum_{j=1}^{N_t}J_{j,n}T_j(t)\mathbf{f}_n^s(\mathbf{r}). \tag{15}$$

Here, RWG [13] basis functions $\mathbf{f}_n^s(\mathbf{r})$ are used as the spatial expansion basis functions. High order time shifted Lagrange interpolant $T(t)$ [14] is used for time expansion, and the order is chosen to be 4. N_S is the number of unknowns. N_t is the number of time steps.

Substituting (13), (14), (15) into (12), and referencing the treatments of convolution operations discussed in [12], after applying the Galerkin and point testing procedures in the space and time domains, respectively, the system of equations can be written as:

$$\tilde{Z}_0 I_i^d=V_i-\sum_{j=1}^{i-1}\tilde{Z}_j I_{i-j}^d+\sum_{j=1}^{i-1}Z_j^p I_{i-j}^p+\breve{Z}\breve{I}_{i-1}, \tag{16}$$

where,

$$I_i^d=\left[J_{i,1},\cdots,J_{i,N_S}\right], \tag{17}$$

$$I_i^p=\left[P_{i,1},\cdots,P_{i,N_S}\right], \tag{18}$$

$$\breve{I}_{i-1}=\left[\breve{P}_{i-1,1},\cdots,\breve{P}_{i-1,N_S}\right], \tag{19}$$

$$\tilde{Z}_{j,mn}=\begin{cases}Z^d_{j,mn}-Z^p_{0,mn}\beta^d_{j,n} & 0\le j\le K\\ Z^d_{j,mn} & j>K\end{cases}\left(m,n=1,2,3,\cdots,N_S\right), \tag{20}$$

$$Z^d_{i-j,mn}=\frac{\mu_0}{4\pi}\int_S\mathbf{f}_m^s(\mathbf{r})\cdot\left\{\int_S\frac{\sum_{n=1}^{N_S}\mathbf{f}_n^s(\mathbf{r}')\partial_\tau T_j(i\Delta t-R/c)}{R}ds'\right\}ds$$
$$-\frac{\mu_0}{4\pi}\int_S\mathbf{f}_m^s(\mathbf{r})\cdot\left\{\int_V\frac{\sum_{n=1}^{N_S}\left[\nabla'\cdot\mathbf{f}_n^s(\mathbf{r}')\right]\partial_\tau T_j(i\Delta t-R/c)}{R}\cdot\mathbf{n}(\mathbf{r}')dv'\right\}ds$$
$$-\frac{1}{4\pi\varepsilon_0}\int_S\mathbf{f}_m^s(\mathbf{r})\cdot\left\{\nabla\int_{S^\Delta}\frac{\sum_{n=1}^{N_S}\left[\nabla'\cdot\mathbf{f}_n^s(\mathbf{r}')\right]\partial_\tau^{-1}T_j(i\Delta t-R/c)}{R}ds^{\Delta'}\right\}ds$$
$$\left(m,n=1,2,3,\cdots,N_S\right), \tag{21}$$

$$\breve{Z}_{mn}=Z^p_{0,mn}\quad\left(m,n=1,2,3,\cdots,N_S\right), \tag{22}$$

$$Z^p_{i-j,mn}=\varepsilon_0\frac{1}{4\pi\varepsilon_0}\int_S\mathbf{f}_m^s(\mathbf{r})\cdot\left\{\nabla\int_S\frac{\sum_{n=1}^{N_S}\left[\nabla'\cdot\mathbf{f}_n^s(\mathbf{r}')\right]\partial_\tau^{-1}T_j(i\Delta t-R/c)}{R}ds'\right\}ds$$
$$-\varepsilon_0\frac{\mu_0}{4\pi}\int_S\mathbf{f}_m^s(\mathbf{r})\cdot\left\{\int_V\frac{\sum_{n=1}^{N_S}\left[\nabla'\cdot\mathbf{f}_n^s(\mathbf{r}')\right]\partial_\tau T_j(i\Delta t-R/c)}{R}\cdot\mathbf{n}(\mathbf{r}')dv'\right\}ds$$
$$-\varepsilon_0\frac{1}{4\pi\varepsilon_0}\int_S\mathbf{f}_m^s(\mathbf{r})\cdot\left\{\nabla\int_{S^\Delta}\frac{\sum_{n=1}^{N_S}\left[\nabla'\cdot\mathbf{f}_n^s(\mathbf{r}')\right]\partial_\tau^{-1}T_j(i\Delta t-R/c)}{R}ds^{\Delta'}\right\}ds$$
$$\left(m,n=1,2,3,\cdots,N_S\right), \tag{23}$$

$$V_{i,m}=\int_S\mathbf{f}_m^s(\mathbf{r})\cdot\mathbf{E}^{inc}(\mathbf{r},i\Delta t)ds\quad\left(m=1,2,3,\cdots,N_S\right), \tag{24}$$

K denotes the order of temporal basis function. The parameters β^d and $\breve{I}$ are both the intermediate variables, which are used to represent the material property and recursive convolution, respectively. The definitions of them are both expounded in [12].

III. NUMERICAL RESULTS

In order to demonstrate the validity of the proposed scheme, three numerical examples for Debye, Drude and Lorentz materials will be presented in this section. The incident wave is the modulated Gaussian plane wave and defined as:

$$\mathbf{E}^{inc}(\mathbf{r},t)=\hat{\mathbf{p}}^{inc}\cos[2\pi f_0(t-\mathbf{r}\cdot\hat{\mathbf{k}}^{inc}/c)]\times\exp[-0.5(t-t_p-\mathbf{r}\cdot\hat{\mathbf{k}}^{inc}/c)^2/\sigma^2]. \tag{25}$$

Here, f_0, $f_{\max}$ and f_{bw} denote the center frequency, maximum frequency and bandwidth of the incident

wave, respectively. $f_{\max} = f_0 + f_{bw}/2$. $\hat{\mathbf{k}}^{inc}$ and $\hat{\boldsymbol{p}}^{inc}$ are the incident and polarization directions.

To test the accuracy and late-time stability of the proposed method, a Debye material coated PEC sphere is considered. The radius of coated PEC sphere is 0.8m, and the thickness is 0.05m, 0.07m, 0.09m, respectively. The incident wave is modulated with $f_0 = 165\,\text{MHz}$, $f_{bw} = 270\,\text{MHz}$, $\hat{\mathbf{k}}^{inc} = \hat{\boldsymbol{z}}$, $\hat{\boldsymbol{p}}^{inc} = \hat{\boldsymbol{x}}$, $\sigma = 6/(\pi f_{bw})$. The number of total unknowns is 3834. The static relative permittivity $\varepsilon_{r,s}$ of the coated layer is 4.2, the permittivity of the medium at infinite frequency $\varepsilon_{r,\infty}$ is 1, and the relaxation time is $t_0 = 5\times10^{-9}s$. The time step Δt is $0.05Lm$, total time is $3000\Delta t$. In order to verify the precision of the proposed scheme further, root mean square (RMS) error is introduced, the parameter of RMS error is defined as:

$$\text{RMS} = \sqrt{\sum_{i=1}^{n} \left| f_{c,i} - f_{r,i} \right|^2 \Big/ \sum_{i=1}^{n} \left| f_{r,i} \right|^2}, \qquad (26)$$

where $f_{c,i}$ are the values of bi-static RCS which are computed by the proposed TDS scheme, and $f_{r,i}$ are the reference Mie series values, n is the number of observed angles. The RMS values of different thickness are shown in Fig. 3, it can be found that the accuracy of the proposed method at the most frequencies is ensured when the thickness of coated layer is no more than 0.09 wavelength of $f_{\max}$. The bi-static RCS curves of the coated sphere with 0.07m layer are shown in Fig. 4, which agree well with the exact Mie solutions. From the magnitude of time domain current coefficient shown in Fig. 5, it can be observed that the late-time stability is also ensured.

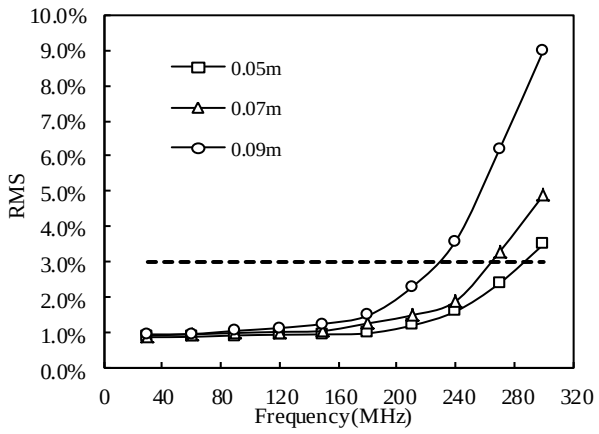

Fig. 3. RMS values of different thickness.

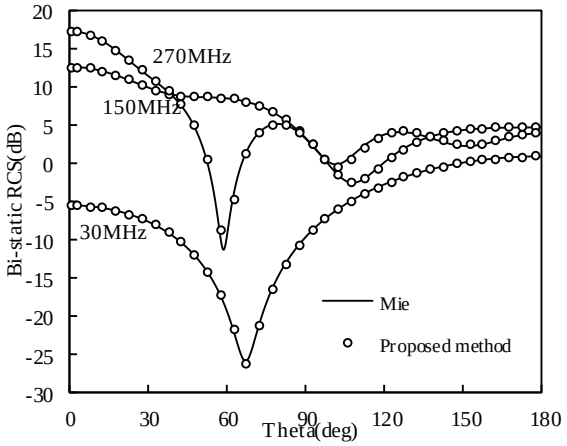

Fig. 4. Bi-static RCS ($\phi = 0^\circ$) of the coated sphere structure at 30, 150, and 270 MHz.

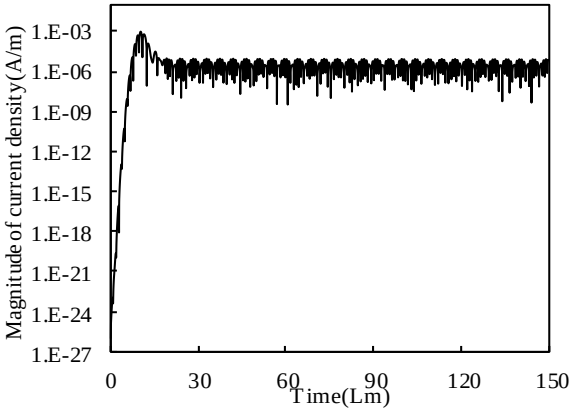

Fig. 5. Magnitude of time domain current coefficient at (0.001971m, -0.797540m, -0.062647m).

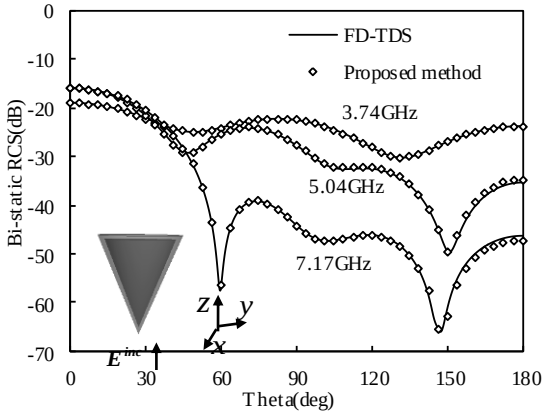

Fig. 6. Bi-static RCS ($\phi = 0^\circ$) of the coated cone structure at 3.74, 5.04, and 7.17 GHz.

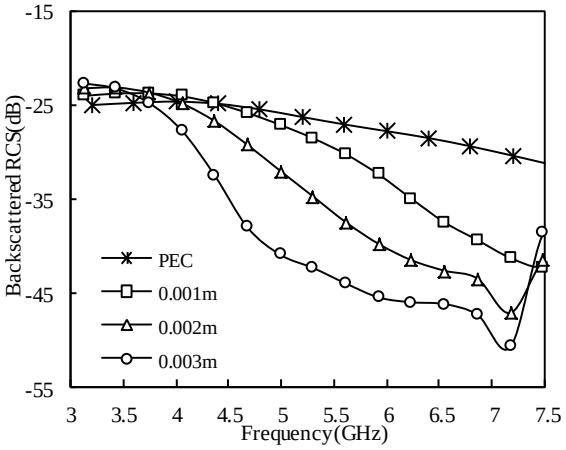

Fig. 7. The comparisons of backscattered RCS with different thickness.

Next, considering the scattering from a coated cone structure, and the coated layer is modeled as a Drude medium with $\varepsilon_{r,\infty}=1$, collision frequency $\delta_p=8\times10^9\,s^{-1}$, plasma frequency $\omega_p=8\times10^9\,s^{-1}$. The radius of inner PEC cone is 0.02m and the height is 0.06m. The thickness of coated dielectric layer is 0.001m, 0.002m, 0.003m, respectively. The center frequency of incident wave is 5.5 GHz, bandwidth is 5 GHz. The time step Δt is $0.01875Lm$, total time is $500\Delta t$. The unknown number of this object is 2376. It is a considerable reduction compared with TD-VSIE [3], which has 15806 unknowns. The bi-static RCS curves of the coated cone with 0.002m layer at different frequencies obtained after the discrete Fourier transform are shown in Fig. 6. Compared with its frequency domain counterpart, it is apparent that there is a good agreement between them. Moreover, the curves of backscattered RCS with different thickness are shown in Fig. 7, the stealth performance of coated structure is evident when compared with the PEC cone, and the performance will be more obvious with the increase of thickness.

At last, an airplane model coated with Lorentz material is considered, as shown in Fig. 8. The dimension of it is $x\times y\times z=2.56m\times1.32m\times6m$. The coating's thickness is 0.02m. For this composite coated structure, the modeling of the coated layer is troublesome. If the TD-VSIE method is used to analyze it, the modeling of the coated layer is inevitable. However, the proposed method is used, the modeling process is simple. For analyzing the electromagnetic scattering from this composite structure by the proposed method, the time step Δt is $1/20\,Lm$, total time is $600\Delta t$. The incident wave is modulated with $f_0=165\,\mathrm{MHz}$, $f_{bw}=270\,\mathrm{MHz}$, $\hat{\mathbf{k}}^{inc}=-\hat{\boldsymbol{z}}$, $\hat{\boldsymbol{p}}^{inc}=-\hat{\boldsymbol{x}}$, $\sigma=3/(\pi f_{bw})$ and $t_p=15\sigma$. The number of total unknowns is 4782. The damping coefficient δ_p of the coated layer is $1\times10^8\,s^{-1}$, resonant frequency ω_p is $1.2\times10^8\,s^{-1}$, static permittivity $\varepsilon_{r,s}=2.8$, $\varepsilon_{r,\infty}=1$. Figure 9 shows the curves of bi-static RCS at different frequencies. Good agreement is obtained again when compared with corresponding frequency domain method, and the ability of analyzing complex target by the proposed method is proven.

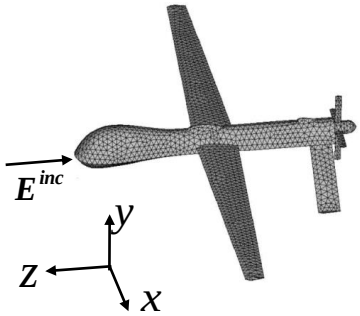

Fig. 8. Geometry of an airplane model.

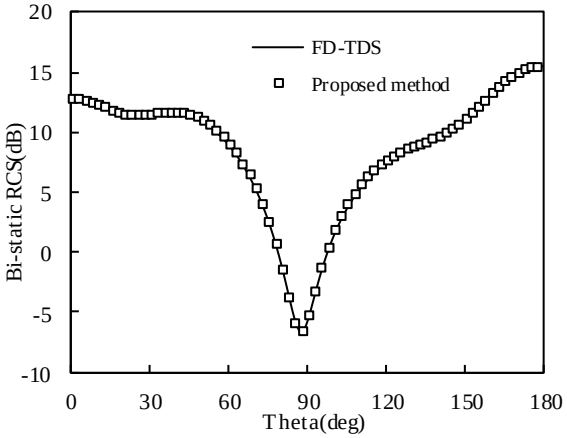

(a)

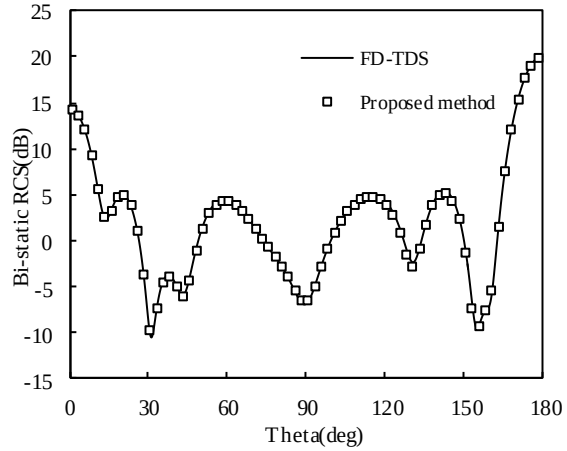

(b)

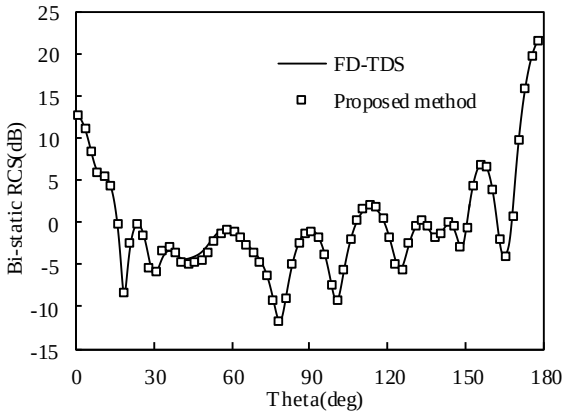

(c)

Fig. 9. (a) Bi-static RCS ($\phi = 0^\circ$) of the coated airplane structure at 54 MHz, (b) bi-static RCS ($\phi = 0^\circ$) of the coated airplane structure at 153 MHz, and (c) bi-static RCS ($\phi = 0^\circ$) of the coated airplane structure at 252 MHz.

IV. CONCLUSION

In this paper, a modified MOT based TD-TDS method is proposed, it extends the practicality of conventional time domain TDS method to analyze the transient electromagnetic scattering from the conductors coated with thin dispersive dielectric. Because the sources in the thin dispersive material layer are all replaced by the current densities on PEC surface, the number of unknowns will be reduced markedly. From the numerical results, the accuracy and stability of the proposed scheme are ensured, and the ability of analyze the coated stealth structure is demonstrated.

ACKNOWLEDGEMENT

We would like to thank the support of Natural Science Foundation under Grant 61522108, Grant 61431006, Grant 61371037, and Grant 61271076, and Ph.D. Programs Foundation of Ministry of Education of China of 20123219110018.

REFERENCES

[1] K. Aygün, B. Shanker, and E. Michielssen, "Fast time domain characterization of finite size microstrip structures," *Int. J. Num. Mod Elect. Net. Dev. & Fields*, vol. 15, no. 6, pp. 439-457, 2002.

[2] A. E. Yılmaz, J. M. Jin, and E. Michielssen, "A parallel FFT accelerated transient field-circuit simulator," *IEEE Trans. Microw. Theory Tech.*, vol. 53, no. 9, pp. 2851-2865, 2005.

[3] Y. L. Hu and R. S. Chen, "Analysis of scattering from composite conducting dispersive dielectric objects by time-domain volume-surface integral equation," *IEEE Trans. Antennas Propag.*, vol. 64, no. 5, pp. 1984-1989, 2016.

[4] S. M. Rao and T. K. Sarkar, "Numerical solution of time domain integral equations for arbitrarily shaped conductor/dielectric composite Bodies," *IEEE Trans. Antennas Propag.*, vol. 50, no. 12, pp. 1831-1837, 2002.

[5] B. H. Jung, T. K. Sarkar, and Y. S. Chung, "Solution of time domain PMCHW formulation for transient electromagnetic scattering from arbitrarily shaped 3-D dielectric objects," *Prog. Electromagn.*, vol. 45, pp. 291-312, 2004.

[6] M. A. Khayat and D. R. Wilton, "Electromagnetic scattering from arbitrarily shaped conducting bodies coated with thin dielectric materials," *Proc. IEEE APS/URSI Int. Symp.*, Jan. 2004.

[7] I. T. Chiang and W. C. Chew, "A coupled PEC-TDS surface integral equation approach for electromagnetic scattering and radiation from composite metallic and thin dielectric objects," *IEEE Trans. Antennas Propag.*, vol. 54, no. 11, pp. 3511-3516, Nov. 2006.

[8] J. Hu, L. Lei, Z. Nie, and S. He, "Fast solution of electromagnetic scattering from thin dielectric coated PEC by MLFMA and successive overrelaxation iterative technique," *IEEE Microw. Wireless Compon. Lett.*, vol. 19, no. 2, pp. 762-764, Dec. 2009

[9] S. He, Z. Nie, and J. Hu, "Numerical solution of scattering from thin dielectric-coated conductors based on TDS approximation and EM boundary conditions," *Prog. Electromagn.*, vol. 93, pp. 339-354, 2009.

[10] S. F. Tao and R. S. Chen, "Electromagnetic scattering analysis of the conductor coated by multilayer thin materials," *IEEE Antennas Wirel. Propag. Lett.*, vol. 12, pp. 1033-1036, 2013.

[11] G. S. Cheng, Z. H. Fan, S. F. Tao, and R. S. Chen, "An efficient solution for the transient electromagnetic scattering from a conductor coated by multilayer thin materials," *IEEE Antennas Wirel. Propag. Lett.*, vol. 14, pp. 1673-1676, 2015.

[12] G. Kobidze, J. Gao, B. Shanker, and E. Michielssen, "A fast time domain integral equation based scheme for analyzing scattering from dispersive objects," *IEEE Trans. Antennas Propag.*, vol. 53, no. 3, pp. 1215-1226, Mar. 2005.

[13] S. M. Rao, D. R. Wilton, and A. W. Glisson, "Electromagnetic scattering by surfaces of arbitrary shape," *IEEE Trans. Antennas Propag.*, vol. 30, no. 3, pp. 409-418, May 1982.

[14] B. Shanker, M. Y. Lu, J. Yuan, and E. Michielssen, "Time domain integral equation analysis of scattering from composite bodies via exact evaluation of radiation fields," *IEEE Trans. Antennas Propag.*, vol. 57, no. 5, pp. 1506-1520, May 2009.

RFID Humidity Sensor Tag for Low-cost Applications

Amjad Ali [1], Syeda I. Jafri [1], Ayesha Habib [1], Yasar Amin [1,2], and Hannu Tenhunen [2,3]

[1] ACTSENA Research Group
University of Engineering and Technology (UET), Taxila, 47050, Pakistan
eng_amjad16@yahoo.com, irum.jafri@umt.edu.pk, ayesha.habib@uettaxila.edu.pk

[2] iPack VINN Excellence Center
Royal Institute of Technology (KTH), Isafjordsgatn 39, Stockholm, SE-16440, Sweden
yasar.amin@uettaxila.edu.pk

[3] TUCS, Department of Information Technology
University of Turku, Turku, 20520, Finland
hannu@kth.se

Abstract ─ This article presents a low-cost, flexible, chipless Radio Frequency Identification (RFID) tag for humidity monitoring applications. The tag exhibits moisture sensing feature within a compact geometrical dimension of 20mm x 17.6mm. The design is loaded with 12 resonators, where each resonator represents 1 bit in the frequency domain. For the designed 12-bit tag, 11 inverted C-shaped resonators are dedicated for encoding 11-bit information in their spectral signature.

An integrated meandered-shaped resonator, covered with moisture sensitive Kapton® HN film, functions as a 1-bit moisture sensor. It is deployed for monitoring relative humidity (RH) levels, simultaneously. The passive RFID tag is realized on Taconic TLX-0 and has an operational bandwidth of 2.62 GHz. Furthermore, the design is modeled and analyzed for multiple substrates. The performance of the sensor tag for various humidity levels indicates that it is a potential solution for inexpensive sensing applications.

Index Terms ─ Moisture sensor, radar cross section, relative humidity, RFID.

I. INTRODUCTION

Radio Frequency Identification (RFID) is a wireless data collecting method deployed for automatic identification of distant targets. Billions of items are anticipated to use RFID tags for recognition in near future [1]. This technology has found its applications in identification [2], security and access control, health monitoring systems [3] and asset tracking [4].

Internet of Things (IoT) is an emerging technology which connects multiple smart objects to internet via wired or wireless networks [5]. Wireless sensor networks and RFID constitutes the IoT system. Recent advancements in RFID technology have facilitated their deployment in IoT [6].

The existing RFID technology is categorized as chip-based RFID and chipless RFID. The chip-based RFID tag consists of a silicon chip, used for data encoding, connected to a transceiver antenna. The presence of microelectronic chip makes the system costly and complex [7]. Therefore, research efforts are made to reduce the cost and complexity of individual tags. Passive RFID technique is the ultimate solution for low-cost system design. Integrating passive sensing feature makes RFID tags attractive for various application-specific utilities [8]. The sensing parameters may include temperature, pressure, methane sensing [9], moisture, crack, and strain sensing, etc. Relative humidity (RH) monitoring is an important physical parameter for drugs and food storage, water detection in damaged walls, archives, and buildings [10]. Therefore, the market has a demand for low-cost, reliable and robust RH sensors. Re-transmission based RFID tags perform moisture monitoring by detecting the change in the phase/amplitude of the retransmitted signal. However, limited coding capacity and restricted number of terminating sensors impose the restriction for sensing of multiples nodes simultaneously [11]. To overcome these limitations, frequency-signature based RFID tags with enhanced coding capacity and miniaturized structure are presented in [12-15]. RH monitoring is achieved by the variations resulted in electromagnetic footprint of the tag. Various moisture sensitive materials, e.g., polyvinyl alcohol, gelatin, dextrin and Kapton® HN film are deployed for RH sensing. These polymers show dielectric or conductive variations with humidity levels. Humidity sensor reported in [12] uses hygroscopic, polyvinyl alcohol (PVA), which absorbs moisture and a shift in the

Submitted On: March 14, 2017
Accepted On: October 24, 2017

resonance frequency is observed. A sensor tag designed on paper substrate exhibits moisture sensitivity [13]. A stepped impedance resonator covered with Kapton® HN film polyamide for humidity monitoring in ubiquitous environment is proposed in [14]. A humidity sensor based on polyvinyl alcohol film polyamide as a sensing material is reported in [15].

In this paper, a miniaturized passive RFID tag is presented. Moisture sensing is integrated in the tag by deploying Kapton® HN film. Section II introduces the RFID tag design, followed by data encoding principal in Section III. The detailed sensing mechanism and results are presented in Section IV and Section V respectively. Section VI reflects the conclusion.

II. GEOMETRICAL CONFIGURATION

Based on the data encoding mechanism, the frequency signature tags can be categorized into 're-transmission' or 'backscattered' tags. The re-transmission tags consist of a transceiver antenna and resonators for ID encoding [16]. In the backscattered RFID tags, the structure is excited by an incident plane wave. Each tag generates a unique electromagnetic (EM) response when the plane wave is incident upon it. The information encoded in backscattered signal is evaluated as radar cross section (RCS). This mechanism is used in the presented sensor tag design.

The proposed RFID tag is designed on substrate Taconic TLX-0 having relative permittivity ε_r=2.45 and loss tangent tan δ=0.0019 and a thickness of 0.5mm. The total dimension of the tag is 20mm x 17.6mm. Resonance at a particular frequency is achieved by etching a slot in copper sheet of thickness 0.035mm. The resonator length l corresponding to the desired frequency $\boldsymbol{f}$ is calculated by using the following set of equations:

$$c = f\,\lambda, \tag{1}$$

$$\lambda_g = \lambda\sqrt{\frac{2}{1+\varepsilon_r}}, \tag{2}$$

$$l = \frac{\lambda_g}{4}, \tag{3}$$

where λ indicates the calculated wavelength at central frequency, λ_g is guided wavelength, ε_r is relative permittivity and c is the speed of light in free space.

Initially, a single inverted C-shaped slot is designed and optimized by using Equations (1)–(3). The same design approach is followed to achieve 11-bit encoding RFID tag by using eleven inverted C-shaped slots. The outermost slot R_1 produces a resonance at the lowest frequency, whereas, the inner slot R_{11} resonates at highest frequency. For sensing purpose, a meandered S-shaped structure is incorporated inside the repetitive inverted C-shaped resonators as shown in Fig. 1. The width of individual slots is kept 0.3mm which allows ease of fabrication using the conventional PCB technology.

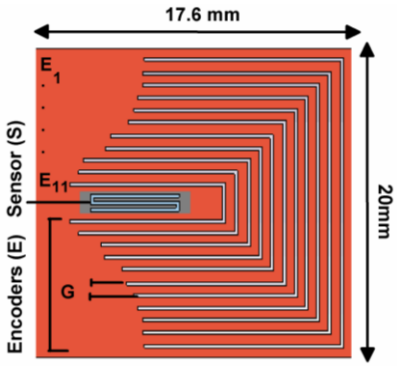

Fig. 1. The proposed RFID sensor tag.

It is observed that if two adjacent slots are placed in close vicinity, then the mutual coupling becomes significant and results in a distorted spectral signature. The effect of noise is minimized by introducing "guard bands" between consecutive resonances. A spectral separation of 200 MHz is maintained between all resonances to eliminate the impact of coupling. This can be controlled by the length l and the separation G between the adjacent slots. Each slot is of different length responsible to produce resonance at particular frequency. The optimized dimensions of RFID tag are summarized in Table 1.

Table 1: Dimensions of RFID tag

Resonator	Length l (mm)	Frequency f (GHz)	Gap	Gaps G (mm)
R_1	41.6	2.98	G_1	0.7
R_2	39.6	3.22	G_2	0.5
R_3	35.8	3.47	G_3	0.6
R_4	33.4	3.72	G_4	0.6
R_5	31.1	3.99	G_5	0.6
R_6	29	4.26	G_6	0.5
R_7	28	4.55	G_7	0.6
R_8	26.2	4.79	G_8	0.7
R_9	26	5.01	G_9	0.6
R_{10}	23.4	5.31	G_{10}	0.55
R_{11}	21.8	5.6	G_{11}	0.7
S	16.2	6.5		

III. DATA ENCODING MECHANISM

The simulations are carried out in commercially available EM software CST MICROWAVE STUDIO® (CST MWS). The tag is excited by using horizontally polarized plane wave. RCS probes are placed at a d = 50mm to observe the backscattered encoded signal. If D is the maximum dimension of the tag and λ is wavelength calculated at central frequency, then far-field distance is calculated by using Equation (4):

$$d = \frac{2D^2}{\lambda}. \tag{4}$$

The tag comprising of only C-shaped encoder slots is simulated and its RCS is studies. Eleven distinct bits, distributed over a frequency range of 2.62 GHz, ranging from 2.98 GHz to 5.60 GHz, are achieved.

A. Multiple ID combinations

The proposed 11-bit ID encoder tag can produce 2^{11} different combinations using logic '1' and '0' which corresponds to presence or absence of a data bit respectively. Figure 2 shows the spectral signature of RFID tag sending all '1'.

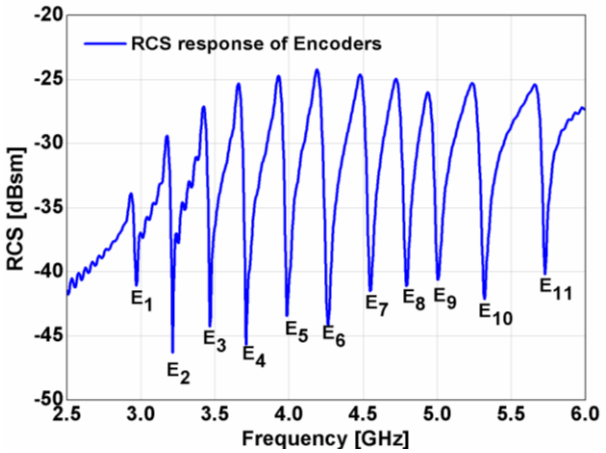

Fig. 2. The RCS response of 11-bit encoder tag.

Different data combinations can be achieved by altering the physical structure of the tag. Figure 3 shows three independent tag IDs '101111111111', '11101111111' and '11111111111'. The RCS comparison in Fig. 3 shows when a slot from a particular position is removed then only the logic state corresponding to that resonator is changed from '1' to '0'. The remaining resonators continue to resonate on the same frequencies.

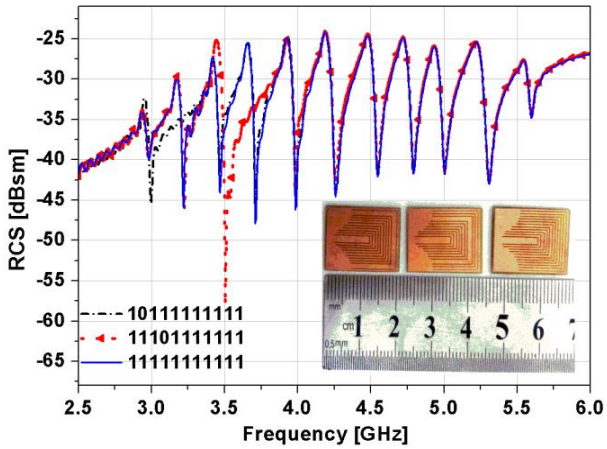

Fig. 3. Shorted tag structures and their RCS.

B. Performance analysis of different tags

Initially, the tag is designed on Taconic TLX-0 substrate with copper as a radiating material having thickness 0.035mm. Furthermore, the tag is designed and analyzed on low-cost substrates, Rogers RT Duroid 5880 and Polyethylene Terephthalate (PET). The comparison for multiple substrates is presented in Fig. 4, without altering the geometrical parameters of the designed tag presented in Table. 1.

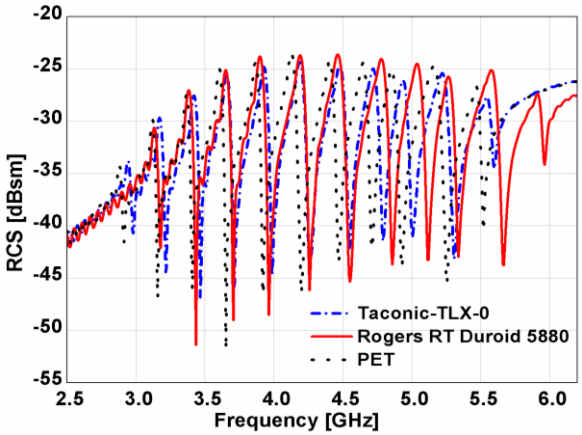

Fig. 4. RCS response for different substrates.

1) Taconic TLX-0

The properties and analysis for Taconic TLX-0 substrate are presented in Section A. It can be seen in Fig. 4 that the overall bandwidth of designed tag is 2.62 GHz, where most significant bit (MSB) produces a resonance at 2.98 GHz, and least significant bit (LSB) resonates at 5.6 GHz.

2) Rogers RT Duroid 5880

The same prototype is designed on Rogers RT Duroid 5880 substrate with a dielectric constant ε_r=2.33, loss tangent tan δ=0.0002 and thickness 0.254mm. The complete band of operation is 2.77 GHz, where MSB resonates at 3.19 GHz, and LSB resonates at 5.96 GHz depicted by Fig. 4.

3) Polyethylene Terephthalate (PET)

The presented RFID tag is designed on a thin, low-cost substrate, PET, to incorporate the flexibility feature. The substrate has a thickness of 0.255mm, dielectric constant εr=3.2 and loss tangent tan δ=0.022. The analysis presented in Fig. 4 shows that the tag designed on PET requires the minimum frequency band for data encoding. In this case, the MSB is observed at 2.91 GHz, and LSB is present at 5.52 GHz.

The comparison of multiple substrates proves that the tag designed on PET substrate provides the best solution in term of flexibility and cost. Another prominent feature of the PET-based tag is the efficient

band utilization. It uses a spectrum of 2.61 GHz to data.

IV. HUMIDITY MONITORING

The integration of a sensing mechanism in RFID tag enables it to provide information about the state of identified object. Relative humidity *RH* is an important parameter for various moisture sensitive applications such as drugs storage, cold storage for a large quantity of food, etc. For this purpose Kapton® HN film with loss tangent tan δ=0.0026, dielectric constant ε_r=3.5 and thickness 0.1mm is used as a hygroscopic sensitive polymer. Its relative permittivity varies with the slight variations in humidity level. Kapton® HN film possesses linear dielectric change with humidity [17] given by Equation (5):

$$\varepsilon_r = 3.05 + 0.008 \times RH. \quad (5)$$

For sensing purpose, a meandered S-shaped structure has been proposed inside the repetitive inverted C-shaped resonators. The S-shaped structure is covered with an adhesive tape of Kapton® HN dielectric film of thickness 0.1mm. The presented sensor tag has compact size and efficient band utilization.

The moisture sensitive nature of the film introduces drift in the resonance frequency of the slot, as indicated in Fig. 5. The sensing trend of the moisture tag in an ambient environment is investigated for different humidity levels. The resonance frequency is shifted to lower values with the increase in %RH. When the humidity level is incremented from 30% to 100%, the resonance is drifted from 6.7 GHz to 6.55 GHz. An overall shift of 150 MHz in the frequency spectrum is observed for the variations in %RH. However, the bits generated by the encoder slots remain unaffected by the change in the sensor resonance frequency.

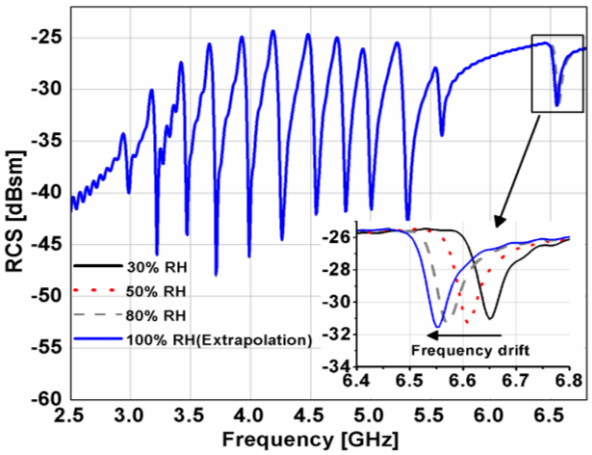

Fig. 5. RCS response of the sensor tag.

The additional sensing functionality in the designed RFID tag equips a conventional package with intelligence to monitor environmental humidity variations and inform the customer about product condition. Henceforth, the sensor integration enables the deployment of the proposed design for various Internet of Things (IoT) and smart sensing applications. A comparison of presented research and previously proposed work [12-14] is shown in Table 2.

Table 2: Comparison of designed tag

Feature	Ref. [12]	Ref. [13]	Ref. [14]	Present Work
Substrate	Taconic TLX-0	Taconic TLX-0	Taconic TLX-0	PET, Roger 5880, Taconic TLX-0
Size (mm)	17x7.5	15x6.8	50x3.45	17.6x20
Trans. bits	4	6	4	12
Flexibility	No	No	No	Yes
Sensing	Yes	Yes	Yes	Yes

V. RESULTS AND DISCUSSION

The proof of concept RFID tag is fabricated on Taconic TLX-0 substrate. The experimental setup deployed, is shown in Fig. 6.

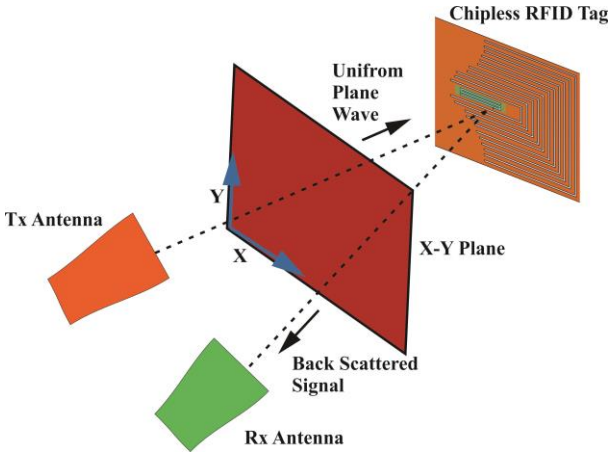

Fig. 6. Experimental setup.

It consists of two horn antennas; Tx is used to illuminate the chipless RFID tag with an incident plane wave, whereas the backscattered response observed by the antenna Rx. The two port vector network analyzer (VNA) R&S®ZVL13is used inside the climate chamber Weiss Technik WK11-180 to investigate the variations in the frequency response of the sensor tag for various humidity levels.

The experimental setup represented by the block diagram in Fig. 6 is used to calibrate the results. A comparison between the computed and measured results is shown in Fig. 7. It can be seen that the measured results are in good agreement with the simulated results.

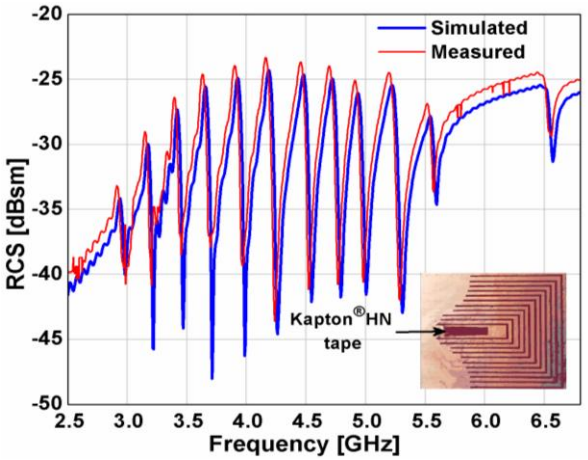

Fig. 7. Computed and measured results.

V. CONCLUSION

A passive RFID tag for 12-bit information encoding is proposed. It provides an inexpensive solution for RH monitoring in wireless communication. The prototype is designed and analyzed on Taconic TLX-0, Rogers RT Duroid 5880 and flexible Polyethylene Terephthalate (PET). In the proposed design, the slots are arrayed so that mutual coupling can be avoided among the resonators and optimized lengths of slots yield the resonances in a squeezed band. Kapton® HN adhesive film is used as sensing material. A shift in resonant frequency is observed with the variation in humidity levels. Therefore, the proposed tag is a potential candidate for data encoding and humidity monitoring for low-cost applications.

ACKNOWLEDGMENT

This work was financially supported by Vinnova (The Swedish Governmental Agency for Innovation Systems) and University of Engineering and Technology Taxila, Pakistan through the Vinn Excellence Centers program and ACTSENA Research Group funding, respectively.

REFERENCES

[1] M. M. Khan, F. A. Tahir, M. F. Farooqui, A. Shamim, and H. M. Cheema, "3.56-bits/cm^2 compact inkjet printed and application specific chipless RFID tag," *IEEE Antennas Wireless Propag. Lett.*, vol. 15, pp. 1109-1112, 2016.

[2] A. Toccafondi, C. D. Giovampaola, P. Braconi, and A. Cucini, "UHF-HF RFID integrated transponder for moving vehicle identification," *ACES Journal*, vol. 25, no. 6, June 2010.

[3] N. Javed, A. Habib, Y. Amin, J. Loo, A. Akram, and H. Tenhunen, "Directly printable moisture sensor tag for intelligent packaging," *IEEE Sensors J.*, vol. 16, no. 16, pp. 6147-6148, Aug. 2016.

[4] O. M. Haraz, M. Ashraf, S. Alshebili, M. R. AlShareef, and H. M. Behairy, "Design of UWB chipless RFID tags using 8-bit open circuit stub resonators," *17th International Symposium on Antenna Technology and Applied Electromagnetics (ANTEM)*, Montreal, QC, pp. 1-2, 2016.

[5] J. Gubbi, R. Buyya, S. Marusic, et al., "Internet of things (IoT): A vision, architectural elements, and future directions," *Future Generation Computer Systems*, vol. 29, no. 7, pp. 1645-1660, 2013. DOI: 10.1016/j.future.2013.01.010

[6] A. A. Fuqaha, M. Guizani, M. Mohammadi, et al., "Internet of things: A survey on enabling technologies, protocols, and applications," *IEEE Communications Surveys & Tutorials*, vol. 17, no. 4, pp. 2347-2376, 2015. DOI: 10.1109/COMST.2015.2444095

[7] T. Noor, A. Habib, Y. Amin, J. Loo, and H. Tenhunen, "High-density chipless RFID tag for temperature sensing," *Electronics Letters*, vol. 52, no. 8, pp. 620-622, 2016.

[8] A. Habib, M. A. Azam, Y. Amin, and H. Tenhunen, "Chipless slot resonators for IoT system identification," *IEEE International Conference on Electro Information Technology (EIT)*, Grand Forks, ND, 2016.

[9] J. Liu and P. B. Li, "Palladium decorated SWCNTs sensor for detecting methane at room temperature based on UWB-RFID," *ACES J.*, vol. 31, no. 8, pp. 989-996, Aug. 2016.

[10] E. M. Amin, N. Karmakar, and B. Winther-Jensen, "Polyvinyl-alcohol (PVA)-based RF humidity sensor in microwave frequency," *Progress In Electromagnetics Research B*, vol. 54, pp. 149-166, 2013.

[11] Y. Feng, L. Xie, Q. Chen, and L. R. Zheng, "Low-cost printed chipless RFID humidity sensor tag for intelligent packaging," *IEEE Sensors Journal*, vol. 15, no. 6, pp. 3201-3208, June 2015.

[12] E. M. Amin, J. K. Saha, and N. C. Karmakar, "Smart sensing materials for low-cost chipless RFID sensor," *IEEE Sensors Journal*, vol. 14, no. 7, pp. 2198-2207, July 2014.

[13] E. M. Amin, M. S. Bhuiyan, N. C. Karmakar, and B. Winther-Jensen, "Development of a low cost printable chipless RFID humidity sensor," *IEEE Sensors J.*, vol. 14, no. 1, pp. 140-149, Jan. 2014.

[14] E. M. Amin, M. Emran, and N. C. Karmakar, "Development of a low cost printable humidity sensor for chipless RFID technology," *RFID-Technologies and Applications (RFID-TA), IEEE International Conference*, 2012.

[15] D. Lu, Y. Zheng, M. Schüßler, A. Penirschke, and R. Jakoby, "Highly sensitive chipless wireless relative humidity sensor based on polyvinyl-alcohol film," *IEEE Antennas and Propagat.*

Society International Symposium (APSURSI), Memphis, TN, pp. 1612-1613, 2014.

[16] R. A. A. Rodrigues, E. C. Gurjão, and F. M. de Assis, "Radar cross-section and electric field analysis of backscattering elements of chipless RFID tag," *IEEE RFID Technology and Applications Conference (RFID-TA)*, Tampere, pp. 103-108, 2014.

[17] Kapton®HN Polyimide film datasheet. Available: http://www2.dupont.com/Kapton/en_US/

Amjad Ali is currently pursuing his M.S. in Telecommunication Engineering from University of Engineering and Technology Taxila, Pakistan. He did his B.Sc. in Electrical Telecommunication Engineering from COMSATS Institute of Information Technology, Islamabad, Pakistan. He worked on wireless cooperative communication and its implementation on USRP kits funded by ICT & RND, Pakistan. He is also a Member of ACTSENA Research Group.

Syeda Irum Jafri is a Faculty Member in Electrical Engineering Department, University of Management & Technology, Lahore. She is working towards her Ph.D. with the ACTSENA Research Group, University of Engineering and Technology, Taxila. Her current research interests include antenna design, microwave engineering and RFID technology.

Ayesha Habib is working as a Research Scholar at Telecommunication Engineering Department, University of Engineering and Technology Taxila, Pakistan. She has completed her M.Sc. in Telecommunication Engineering and Technology Taxila, Pakistan. In the same year she has joined ACTSENA Research Group as a Research Scholar and is pursuing her Ph.D. in Chipless RFID domain. She is also a Student Member of IEEE.

Yasar Amin is Chairman and Associate Professor of Telecommunication Engineering Department, University of Engineering and Technology Taxila, Pakistan. He is the Founder of ACTSENA Research Group at UET Taxila, Pakistan. He did his M.Sc. in Electrical Engineering in 2003 with specialization in System-on-Chip Design from Royal Institute of Technology (KTH), Sweden. His Ph.D. is in Electronic and Computer Systems from Royal Institute of Technology, Sweden, with the research focus on printable green RFID antennas for embedded sensors, while has MBA in Innovation and Growth from Turku School of Economics, University of Turku, Finland. He has done several specialized courses from Stanford University, California, USA and Massachusetts Institute of Technology (MIT), USA. He has supervised over 15 M.Sc. thesis, and presently supervising 8 doctoral thesis. He is presently serving as leading Guest Editor at two International Journals and an active Reviewer of more than a dozen well reputed International journals. Amin is a Member of IEEE, IET, ACM and ACES.

Hannu Tenhunen is Chair Professor of Electronic Systems at Royal Institute of Technology (KTH), Stockholm, Sweden. Tenhunen has held Professor position as Full Professor, Invited Professor or Visiting Honorary Professor in Finland (TUT, UTU), Sweden (KTH), USA (Cornel U), France (INPG), China (Fudan and Beijing Jiaotong Universities), and Hong Kong (Chinese University of Hong Kong), and has an honorary doctorate from Tallinn Technical University. He has been the director of multiple national large-scale research programs or being an initiator and director of national or European graduate schools. He has actively contributed to VLSI and SoC design in Finland and Sweden via creating new educational programs and research directions, most lately at European level as being the EU-level Education Director of the new European flagship initiative European Institute of Technology and Innovations (EIT), and its Knowledge and Innovation Community EIT ICT Labs.

Modal Analysis of Different Stator Configurations to Mitigate Electromagnetically Excited Audible Noise and Vibrations of Switched Reluctance Motors

Selma Čorović, Rok Benedetič, and Damijan Miljavec

Department of Mechatronics, Laboratory for Electrical Machines, Faculty of Electrical Engineering
University of Ljubljana, SI1000 Ljubljana, Slovenia
selma.corovic@fe.uni-lj.si, rok.benedetic@gmail.com, damijan.miljavec@fe.uni-lj.si

Abstract ─ The primary objective of this paper was to investigate different stator configurations of switched reluctance motors (SRM) in order to mitigate electromagnetically exited audible noise and vibration. We analyzed natural frequencies of different SRM stator configurations by virtue of modal analysis theory. The three-dimensional numerical modeling of SRM stator geometry was performed by using finite element method. Based on the output results, we propose the solutions on how to select an appropriate stator configuration in order to increase its natural frequencies beyond the resonant operational frequency, and thus, to mitigate the resulting audible noise and vibration. The numerical and analytical results are successfully compared to the published data.

Index Terms ─ Electromagnetic force, finite element analysis, modal analysis, natural frequencies, noise and vibration, switched reluctance machines.

I. INTRODUCTION

A quest for energy efficiency, reliability and cost effectiveness has fostered research and development of switched reluctance motors (SRM) due to the fact that they are comparable or more advantageous over their counterparts [1,2]. Numerous studies demonstrated that the SRM may be competitive electric drive system candidate in different automotive and aerospace applications where high-performance and variable-speed is required [1-5]. In addition, the SRM and the SRM drive systems are receiving considerable attention from academia and industry [6-8]. However, among the major drawbacks that prevent the SRM from being more prominent in many industrial and other applications are acoustic noise and vibrations.

Theoretical analysis predicted and experimental measurements of airborne audible acoustic noise confirmed that dominant component of the SRM acoustic noise and vibration signal is emitted from the machine's stator [9]. It has been found that pronounced acoustic noise occurs when the frequencies of exiting stator radial magnetic forces acting on itself coincide with its natural frequencies. In particular, the level of acoustic noise and vibration strongly depends on the geometry design and material properties of the stator configuration of switched reluctance motors. Therefore, the stator configuration need to be carefully planned and designed within the pre-construction stage of the SRM machine. It has been demonstrated that the acoustic noise and vibrations can be successfully predicted with analytical and numerical mathematical models of the SRM, which were validated with experimental measurements [12-15]. For example, the issue of acoustic noise production have been addressed by varying the combination of stator–rotor poles [10]. The influence of windings and end-bells has also been studied on a commercial SRM configuration with 8/6 stator vs. rotor pole ratio [9]. However, although a large body of literature already exists on the analysis of acoustic noise and vibration of the SRM, an optimum SRM configuration is still a subject of scientific investigation [2,9-14].

The primary objective of this study is to mitigate the electromagnetically exited audible noise and vibration of SRM by altering the natural frequencies of different 3-phase SRM configurations. This study is focused on the natural frequencies for the most critical modal shapes of the small size SRM stator configurations (i.e., up to few kW [12]) by virtue of modal analysis theory. First, the natural frequencies of 3-phase SRM stator SRM configurations with different ratios between stator vs. rotor pole number are numerically analyzed based on 3D finite element modeling. Second, the impact of the SRM stator geometry modifications on its natural frequencies was studied by increasing the numbers of stator poles, by changing the thickness of the stator yoke and by adding the spacers and the end-bells to the analyzed stator geometry. The influence of the stator poles geometry modification on the natural frequencies of the resulting stator geometry was also investigated and new stator geometries are proposed. Finally, the numerical results

Submitted On: May 10, 2017
Accepted On: October 17, 2017

of 3D simulations were compared to the analytical calculations based on Jordan's law. Based on the obtained results the solutions are proposed on how to design an appropriate stator geometry in order to increase its natural frequencies beyond the resonant vibration frequency, and consequently to avoid or mitigate the undesirable acoustic noise.

II. THEORETICAL CONSIDERATION

In our present study we focused on the magnetically excited vibration and acoustic noise of small size (i.e., up to few kW [12]) 3-phase switched reluctance motors by means of modal analysis theory. We investigated the impact of different SRM stator geometry modifications on their natural frequencies and the corresponding modal shapes that are responsible for the majority of vibration and acoustic noise. The stators of SRMs with three different ratios between the number of stator poles N_s vs. number of rotor poles are investigated: N_s/N_r = 6/4, 8/6 and 12/8. (Note: The number of the SRM stator poles is equal to the number of the SRM stator teeth).

The maximum noise of the switched reluctance motors is produced when the harmonics of the excitation frequencies of the magnetic radial force $f_{exc}(n)$ coincide with the natural frequencies of the SRM stator. The excitation frequencies $f_{exc}(n)$ in Hz for harmonic numbers n can be calculated according to Equation (1) [12]:

$$f_{exc}(n) = n \cdot f_p = \frac{n \cdot N_{rp} \cdot \omega_m}{60}, \quad (1)$$

where n is harmonic number (n = 1, 3, 5,….), f_p is the fundamental frequency of the phase current in Hz, N_{rp} is the number of the machine rotor poles and the ω_m is the rotational speed of the machine in rotations per minute.

The most critical modes of vibration of small size machines [12] are the first several modal shapes m (typically m = 0, m = 2, m = 4), while for the medium and large size machines also higher vibrational modal shapes (m > 4) may become also important. The contribution of the modal shapes to the acoustic noise and vibration depend on the stator/rotor configuration of the SRM. Specifically, for the 3-phase SRM with the ratio 6/4 and 8/6 the second-order cylindrical mode, also termed in this case as fundamental mode m = 2 is predominant due to the fact that two opposite stator poles are excited simultaneously. Thus, the radial force acts on the stator between these two poles and further on mechanically ovalises the circumference of the stator's yoke. The 3-phase SRM with N_s/N_r ratio 12/8 the fourth-order mode m = 4 causing double oval deformation (i.e., double ovalisation) on the stator's circumference, due to the fact that four opposite stator poles are excited simultaneously. In this case, m = 4 is responsible for the majority of the emitted acoustic noise and vibration. In this study the most critical modal shapes and the corresponding natural frequencies for 6/4, 8/6 and 12/8 SRM configurations are calculated and compared by virtue of modal analysis.

The determined natural frequencies and mode shapes are solutions of an eigenvalue problem [14, 18] described by a general system of equations of motion, which assumes free vibration and ignores the dumping, Equation (2):

$$\left\{[H] - (\omega)^2[M]\right\} \cdot \{X\} = \{0\}, \quad (2)$$

where [H] and [M] are stiffness matrix and the mass matrix, respectively. The square roots of the eigenvalues are the natural frequencies ω (in radians/sec) of the SRM stator structure. The natural frequencies f in cycles/sec are than calculated as $f=\omega/2\pi$. The eigenvectors {X} represent the mode shapes – the shape assumed by the SRM stator structure when vibrating at frequency f.

The modal analysis of 3D SRM stator structures was performed by numerically solving the Eq. (2) using a commercial finite element based software package Autodesk Inventor Professional 2016 and Matlab R2013a. All numerical simulations were run on a computer platform with 2.7 GHz of CPU speed and 3GB of RAM. The accuracy of the numerical results was controlled by the selection of number of finite elements within the model. The final density of finite element mesh was created by increasing the number of elements until the results of the calculated natural frequencies changed less than 0.5%, and thus the numerical error was negligible. However, it should be noted that the models with high finite element number (high quality of finite element mesh) require significant computational time and computer resources.

Within the final part of the study the natural frequencies of the studied baseline SRM stator geometries were also analytically calculated by employing Jordan's law [14,17] in order to find out wheatear it can be used as a more rapid but approximate solution for calculation of natural frequencies of SRM. The analytical results were then compared to the numerically calculated natural frequencies of the SRM stators in 3D (the geometry data are taken from Table 1 with M270-35A material properties). According to the Jordan's law [14,17] the natural frequency for zero modal shape (m = 0) of the stator can be calculated with Equation (3) [14,17]:

$$f_0 = \frac{1}{2 \cdot \pi} \cdot \sqrt{\frac{E}{\rho \cdot R_c^{\,2} \cdot \Delta_m}}, \quad (3)$$

where E is Young's modulus of the stator core material, ρ is the density of the material composing the stator core, R_c is the mean stator yoke radius, and the Δ_m is the corrective factor [14] that accounts for the effect of the stator poles' mass on the stator natural frequencies. The corrective factor Δ_m can be calculated by Equation (4) [14]:

$$\Delta_m = \frac{m_{sy} + N_s \cdot m_{sp}}{m_{sy}}, \quad (4)$$

where the m_{sy} and m_{sp} stand for the stator yoke mass and the stator pole mass, respectively, whereas the N_s is the number of the stator poles.

According to the Jordan's law [14,17], the natural frequencies for modal shapes $m \geq 2$ are expressed with Equation (5):

$$f_m = \frac{f_0 \cdot w_{sy} \cdot m \cdot \left(m^2 - 1\right)}{2 \cdot \sqrt{3} \cdot R_c \cdot \sqrt{m^2 + 1}}, \quad (5)$$

where f_0 is natural frequency for zero modal shape, w_{sy} is the thickness of the stator yoke, m is the number of the modal shape ($m \geq 2$), and R_c is the mean stator radius without considering the stator poles. The Equations (3) and (5) are derived for 2D structures that represent an approximation of the electrical machine stator with a ring (the stator teeth (i.e., poles) are taken into account by introducing the corrective factor Δ_m (Equation (4)).

III. RESULTS AND DISSCUSION

A. Verification of 3D numerical modeling

Within the first part of the study a preliminary 3D model numerical analysis was done based on the on the reference SRM configuration geometry and its material properties taken from the literature [9,15]. The stator configuration (the SRM with N_s/N_r = 8/6 and the ribbed frame (i.e., stator housing)) of the reference SRM model [9] is based on the modal analysis theory and on experimental validation performed using a shaker-accelerometer system. In order to verify the accuracy of our 3D numerical results, we compared the results of our numerical simulations to the results from the reference study [9]. The 3D model of the SRM stator (N_s = 8) with the ribbed frame geometry used as a reference model for numerical results verification (the model geometry was built according to the dimensions of the model developed in [9]) is shown in Fig. 1 (a). The dimensions are given in millimeters. The 2D view in the central XY cross section of the SRM stator only is shown in Fig. 1 (b). The geometrical parameters in the Fig. 1 (b), the stator yoke thickness w_{sy}, the height of the stator pole h_p (i.e., the stator tooth), the width of the stator pole w_{sp}, the pole arc of stator $ß$, stator outer radius R_{so}, the yoke inner radius R_{sy}, the stator bore radius R_{si} and the length of stator L. According to [9], the values of the geometrical parameters are w_{sy} = 11.4 mm, h_p = 30 mm, w_{sp} = 16.9 mm, $ß$ = 20.2°, R_{so} = 89.8 mm, R_{sy} = 78.4 mm, R_{si} = 48.18 mm, and L = 151 mm. According to [9], the stator was modelled as a ferromagnetic material with the Young's elasticity modulus $E = 2.07*10^{11}$ N/m^2, while the material for the stator frame is cast iron with $E = 1.65*10^{11}$ N/m^2. The mass density of both materials is 7800 kg/m^3.

The calculated natural frequencies for m = 2 and m = 4 obtained in this study were 1331 Hz and 4237 Hz, respectively (as shown in Figs. 2 (a) and 2 (b)). These two frequencies differed from the calculated and measured natural frequencies in [9] by 1.3% and 2.8% for the modal shape 2 and 4, respectively. Thus, a good agreement was obtained between our results and the results previously obtained from [9]. This small difference can be attributed to the difference in geometry of the modeled geometry dimensions that were not available to us from [9]. Namely, the geometry of ribs at the bottom part of the stator frame (present in [9]) was omitted in the model developed in this study. Based on this comparison the preliminary numerical models built in this study were verified. Based on compared results we concluded that the preliminary mode can be successfully used and extended for further analysis performed in this study.

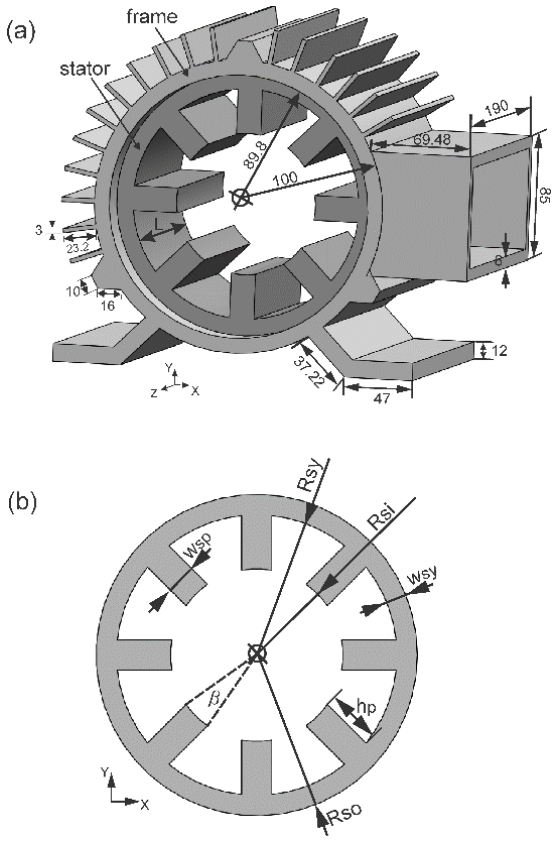

Fig. 1. (a) The 3D model of the SRM stator (N_s = 8) with the ribbed frame geometry used as a reference model for numerical results verification (the model geometry was built according to the dimensions of the model developed in [9]; the dimensions are given in millimeters), and (b) the 2D view in XY cross section of the SRM model with the geometrical parameters.

The numerical results are shown in Fig. 2. The results (i.e., the deflection profiles at the calculated natural frequencies) are displayed in central XY cross-section plane of the 3D finite element models. The grayscale color bar shows relative movement/displacement profile from the minimum (light gray) to maximum (black) value as a result of numerical modal analysis performed

in Autodesk Inventor software we used in our study. The white color in figures represents the stator area where no movement/displacement occurs. The color chart shows relative movement/displacement values based on which the modal shapes are formed. Therefore, the units are not applicable (they have no actual physical value), since the mode shapes values are relative. (Note: This is also valid for the results shown in the Fig. 6 and Fig. 8.)

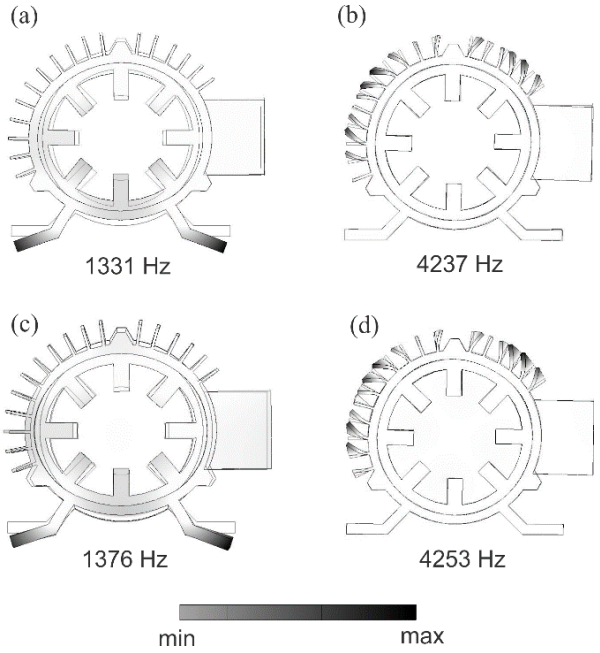

Fig. 2. The calculated deflection profiles and the corresponding frequencies of SRM stators with ribbed frame without end-bells: (a) 1331 Hz and (b) 4237 Hz; and with end-bells: (c) 1376 Hz and (d) 4523 Hz.

The second modal shape (f = 1331 Hz) of the modeled assembly of the SRM stator with ribbed frame is shown in Fig. 2 (a). From the Fig. 2 (a) it can be seen that at lower natural frequency the stator deforms according to the second modal shape, while the stator frame remains still. It is interesting to note that at higher natural frequencies (f = 4237 Hz) the stator remains still while the mechanical vibration and deformation of the stator frame ribs considerably increases, as shown in Fig. 2 (b). In addition, in order to increase the stiffness of the stator geometry the end-bell geometry (illustrated Fig. 5 (b) was also added to the baseline stator geometry and the natural frequencies of the whole assembly were calculated. The calculated and visualized results for the stator assembly with one end-bell are displayed in Figs. 2 (c) and 2 (d). The calculated numerical results shown in Figs. 2 (c) and 2 (d) indicate that if the end-bells are added to the analyzed assembly the vibration of the whole assembly is somewhat constrained, resulting in increase of the natural frequency as compared to the stator assembly without the end-bell. Due to the presence of end-bell the SRM assembly is expected to emit the vibration of higher frequencies compared to the stator assembly without the end-bell. Interestingly, at higher frequencies the ribs of the stator frame starts to vibrate, and thus the mechanical noise and vibration is emitted predominantly due to the frame.

B. Influence of SRM stator geometry modification on its natural frequencies

The SRM stator geometries (with N_s = 6, 8 and 12) given in Fig. 3 served as reference/baseline models for all further geometry modifications and corresponding natural frequency calculations.

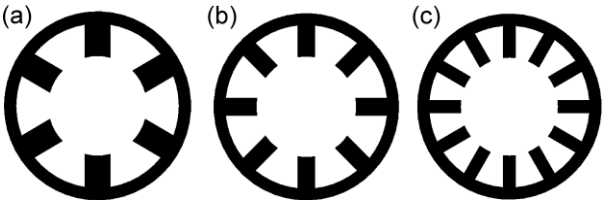

Fig. 3. The XY view of the SRM stators with: (a) N_s = 6, (b) N_s = 8, and (c) N_s = 12.

The XY view of the SRM stators geometry with Ns = 6, 8 and 12 is given in Fig. 3 (a), Fig. 3 (b) and Fig. 3 (c), respectively.

Table 1: Dimensions of the analyzed SRM stators

N_s	6	8	12
w_{sp}	25.82 mm	15.64 mm	13.05 mm
ß	30°	18°	15°
R_{so}	95 mm		
R_{sy}	82.5 mm		
L	114 mm		
w_{sy}	12.5 mm		
R_{si}	50 mm		
h_p	32 mm		

The width of the stator pole and the stator pole arc were adjusted to each of the stator geometry according to the design recommendations for the SRM stator sizing [15]. The stator was modeled as a solid/bulk material without taking into account the laminations. The used material for the stator yoke is M270-35A. The dimensions of the SRM stators geometries analyzed in this study are listed in Table 1.

Within this part of the study, the influence of modification of the stator yoke thickness w_{sy} and the height of the stator poles (i.e., stator teeth) h_p on the stator natural frequencies was numerically investigated. The parameterization of the SRM stator geometry was carried out by modifying the stator yoke thickness and height of the stator pole with respect to the dimension

of the baseline model dimensions w_{sy} = 12.5 mm and h_p = 32 mm by increments of 0.5 mm. In this way the functional dependency of the studied SRM natural frequencies f [Hz] on yoke thickness f(w_{sy}) and pole height f(h_p) was obtained, as shown in Fig. 4. The numerical simulations show that the increase in height of the stator's pole h_p results in decrease of natural frequency for all studied SRM stator configurations as shown in Fig. 4 (a) and Fig. 4 (b). On the other hand, the Figs. 4 (a) and 4 (b) show that higher number of stator poles (i.e., 6/4 vs. 8/6) yields higher natural frequency of the SRM stator configuration. As for the parameterization of the stator yoke thickness, the SRM stator natural frequencies increased with the increase of the stator yoke thickness Fig. 4 (c) and Fig. 4 (d). This is in agreement with previous findings which demonstrated that undesirable vibrations of the SRM machines can be reduced by employing relatively thick stator yokes to minimize deflection, which in turn increases the mechanical stiffness of the machine [17].

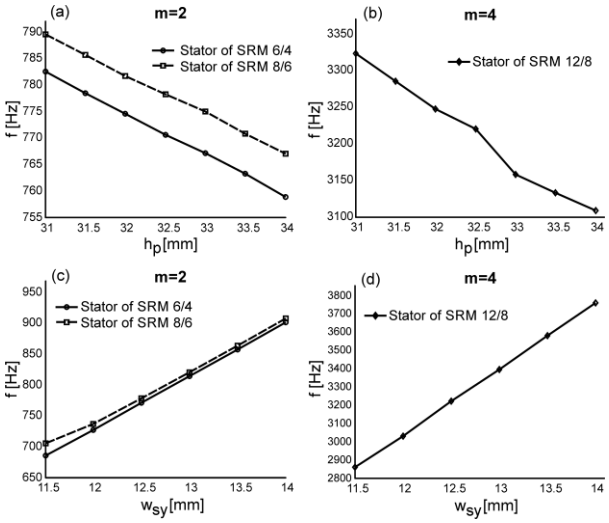

Fig. 4. The calculated relationships: (a) f(h_p) and (b) f(w_{sy}) for the SRM designs with N_s = 6 and N_s = 8, and (c) f(h_p) and (d) f(w_{sy}) for the SRM design with N_s = 12.

Furthermore, the increase of natural frequencies of SRM configuration by adding the aluminum spacers between the stator poles and the end-bells is also numerically calculated. The geometry and placement of the spacers and the end bells added to the reference/ baseline SRM geometries (from Fig. 3) are shown in Fig. 5 (a) and Fig. 5 (b), respectively.

The number of stator poles in SRM designs depends on the number of the excitation voltage phases used (i.e., three phases are needed for the 6/4 SRM design, four phases are needed for the 8/6 SRM; the 6/4 design is two times repeated in the 12/8 design) [15]. The thickness of the spacers inserted between the stator poles depends on the available space within the stators' slots (as well as on the properties of the windings, fill factor, current density and B(H) characteristic of the stator material). In this study the width of the spacers is 5 mm, while the width of the end-bell is 10 mm, Fig. 5. The number of spacers is equal to number of stator poles. Since the end-bells represent the bearing housing, their dimensions thus need to be calculated according to the bearing dimensions. When calculating the end-bell dimensions it is also important to achieve a high enough mechanical strength of the SRM housing in order to efficiently support the mechanical loadings of the shaft. In order to precisely calculate the natural frequencies a 3D numerical modeling need to be used by taking into account the material and geometrical properties of the SRM stator structure.

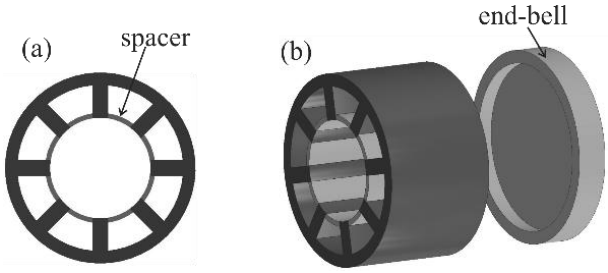

Fig. 5. Geometry and placement of: (a) the spacers between poles, and (b) the spacers between poles and the end-bell added to the baseline geometry of the SRM stators. The width of the spacers is 5 mm. The width of the end-bell is 10 mm.

The results of 3D numerical calculations of stator motion profiles in ZX cross section plane at circumferential mode shapes m = 2 (for SRMs 6/4 and 8/6) and m = 4 (for SRM 12/8) and the corresponding natural frequencies are shown in Fig. 6. The results are displayed in increasing order of the calculated natural frequencies. The calculated natural frequencies and the deflection profiles of the baseline SRM stators with N_s = 6, N_s = 8 and N_s = 12 are shown Figs. 6 (a), 6 (b) and 6 (c). The numerical results show the natural frequencies can be increased by adding the end-bells to the stators as shown in Figs. 6 (d), 6 (e) and 6 (f).

The natural frequencies can be further increased by adding the spacers between the stator poles (Figs. 6 (g), 6 (h) and 6 (i)). The integration of the spacers and end-bell together yields the highest increase in natural frequencies as shown in Figs. 6 (j), 6 (k) and 6 (l). The increase in natural frequencies of the stators due to different stator modifications with respect to the natural frequencies of the reference stator models with N_s = 6, N_s = 8 and N_s = 12 is evaluated and compared in Table 2. The natural frequency (f) of the modified stators is divided by the natural frequency of the reference stator model (f_0) (i.e., factor f/f_0 in Table 2). The factor f/f_0 is

calculated for the stators with one end-bell (no spacers), with spacers (and no end-end-bells), with one end-bell and spacers, two end-bells (and no spacers) and with two end-bells and spacers. As shown in Table 2, the integration of two end-bells and spacers yields the highest increase in natural frequencies (i.e., by factors 3.97, 4.15 and 2.44).

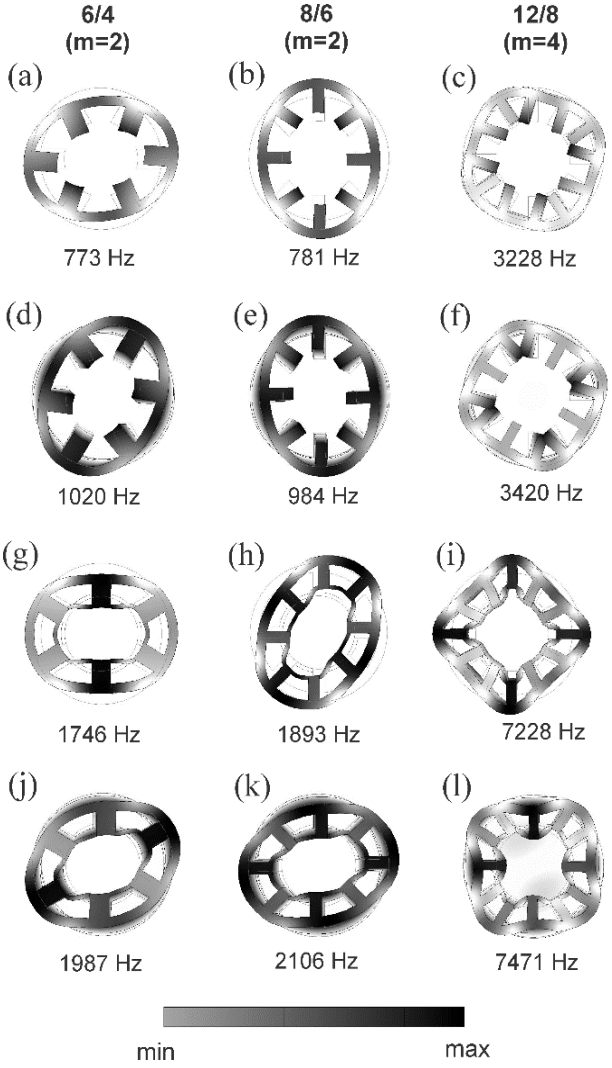

Fig. 6. Comparison of 3D numerical modeling results for the SRM stators with N_s = 6, 8 and 12.

In conclusion, the results of 3D numerical modeling (Fig. 6 and Table 3) demonstrate that the stator modifications such as integration of spacers and/or end-bells constraint the intensity of the stators' motion and significantly increase the natural frequencies of the SRM stators. This may in turn result in reduction of undesirable noise and vibration that may be produced by the SRM.

Table 2: Natural frequencies of the modified SRM stator models (f) with respect to the natural frequencies of the reference/baseline SRM stator models (f_0) with N_s = 6, 8 and 12

SRM 6/4		SRM 8/6		SRM 12/8	
m = 2		m = 2		m = 4	
(Hz)	f/f_0	(Hz)	f/f_0	(Hz)	f/f_0
Reference Stator (f_0):					
773	1	781	1	3228	1
With One End-bell (f):					
1020	1.32	984	1.26	3420	1.06
With Spacers (f):					
1746	2.26	1893	2.42	7228	2.24
With One End-bell and Spacers (f):					
1987	2.58	2106	2.70	7472	2.31
With Two End-bells (f)					
2496	3.23	2595	3.32	7785	2.41
With Two End-bells and Spacers (f):					
3068	3.97	3241	4.15	7878	2.44

C. Influence of stator pole geometry modifications on natural frequencies

Within the third part of the study, the influence of modification of stator pole geometry (i.e., stator teeth) on the natural frequencies of the SRM stator was numerically investigated. The stator geometry modifications were done on the SRM stator with N_s = 12. Three different modifications of the reference/baseline stator pole geometry (shown in Fig. 7 (a)) were done as follows: the first modification of the baseline stator pole was a trapezoidal pole (Fig. 7 (b)), the second one was trapezoidal pole with a circumference (Fig. 7 (c)) and the third one was a trapezoidal pole with a circumference of pole and the pole's root (Fig. 7 (d)). The geometrical modifications with respect to the reference/baseline geometry are marked with red color in Fig. 7. The results of numerical modeling are displayed in order of increasing natural frequency for different studied geometries in Fig. 8.

The numerical results in Fig. 8 show that the natural frequencies of the stator can be altered by modifying the stator pole geometry. The highest natural frequency as compared to the reference/baseline model (shown in Fig. 8 (a)) is obtained with the trapezoidal pole with a circumference of pole and pole's root as shown in Fig. 8 (d) (i.e., from 3228 Hz to 3593 Hz). These results can be particularly useful for the SRM designs which require higher input currents and thus more space for the windings with a larger cross section area of the wire. Similar increase in natural frequency by modifying the stator pole geometry can be obtained in other SRM configurations (e.g., 6/4 and 8/6 SRM stator designs). However, the geometrical modifications of the poles

need to be selected according to the desired winding fill factor and the stator magnetic load ability.

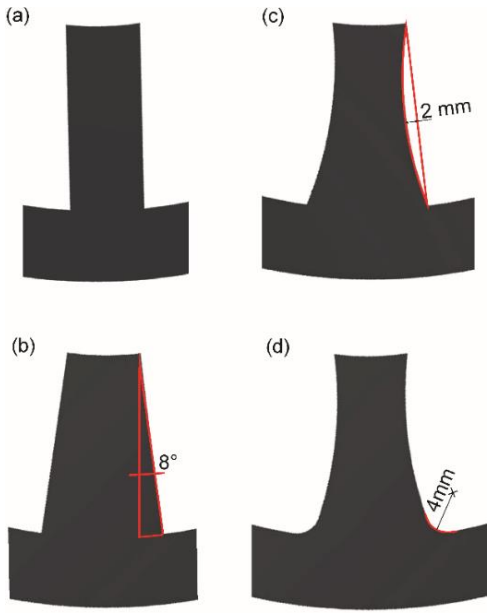

Fig. 7. The reference/baseline stator pole geometry the SRM 12/8 (a) and the modified stator poles (b) trapezoidal pole; (c) trapezoidal pole with a circumference, and (d) trapezoidal pole with a circumference of pole and the pole's root.

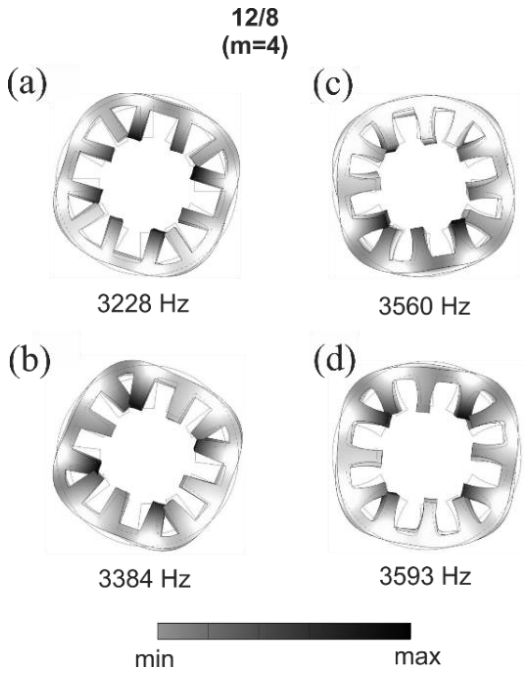

Fig. 8. Numerical results: (a) the reference/baseline stator pole geometry, (b) trapezoidal pole, (c) trapezoidal pole with a circumference, and (d) trapezoidal pole with a circumference of pole and pole's root.

D. Comparison between numerical and analytical results

Within the final part of the study the natural frequencies of the studied baseline SRM stator geometries were also analytically calculated by employing Jordan's law (Equations (2), (3) and (4)). The analytical results (i.e., calculated natural frequencies of the stators approximated with cylindrical rings in 2D) are compared to the numerically calculated natural frequencies of the SRM stators in 3D (Table 3).

Table 3: Comparison between numerical and analytical results

N_s and m	Analyt. (Hz)	Numer. (Hz)	Difference (%)
$N_s = 0$, $m = 2$	962	982	2
$N_s = 0$, $m = 4$	5218	5174	0.85
$N_s = 6$, $m = 2$	736	773	5
$N_s = 8$, $m = 2$	768	781	1.8
$N_s = 12$, $m = 4$	3991	3228	23

The smallest difference is obtained between the numerical model of hollow cylinder (stator without poles $N_s = 0$) and the analytical solution (with the corrective factor $\Delta_m = 0$) (i.e., 2% and 0.85% for $m = 2$ and $m = 4$, respectively). However, this model can result in erroneous calculations of natural frequencies if used as an approximation for the SRM stators with teeth/poles (e.g., f = 733 Hz for the SRM ($N_s = 6$, $m = 2$) vs. f = 962 Hz for the SRM ($N_s = 0$, $m = 2$), Table 3).

As for the stator models with poles, better agreement was obtained between numerical and analytical results for the modal shapes $m = 2$ (the difference between the numerical and analytical results was 5% and 1.8%, for 6/4 and 8/6 SRM, respectively) as compared to the results calculated for modal shapes $m = 4$ for 12/8 SRM stators (the difference between the numerical and analytical results was 23%). The comparison between the analytical and numerical results (Table 3) implies that analytical solution obtained by using Jordan's law (if the corrective factor is taken into account) is good enough to be used as a rapid, but rough estimation of natural frequencies of the SRM stators for modal shapes $m = 2$. A precise calculation of natural frequencies requires a detailed 3D numerical modeling by considering all geometrical and material properties.

The difference between the analytical and numerical results occurs due to the fact that the analytical results are obtained using Jordan's law which describes the natural frequency of a cylindrical ring which approximates the geometry of the SRM with multiple poles in 2D, while the numerical calculation are performed for the SRM stator geometry in 3D [14]. Better agreement between the two sets of results can be obtained by considering solutions of extended Jordan's law [14], or more complex analytical models [12,14].

IV. CONCLUSION

The natural frequencies and thus the level of acoustic noise and vibration strongly depend on geometrical properties of the SRM stator which need to be carefully planned and designed within the pre-construction stage. This study proposes the solutions on how to select an appropriate stator SRM geometry in order to increase its natural frequencies beyond the operational frequencies, and thus to mitigate the electromagnetically excited noise and vibration of the SRM. The natural frequencies of different SRM stator configurations were numerically and analytically investigated by virtue of modal analysis theory. The obtained results are successfully verified based on the previously published theoretical and experimental data.

The obtained results demonstrate that the natural frequencies of the SRM stator can be increased, and thus the noise and vibration can be mitigated by performing the following stator modifications: 1) by increasing the number of the stator pole, 2) by decreasing the height of the stator pole, 3) by increasing the thickness of the stator yoke, 4) by inserting the spacers between the poles, 5) by adding the end-bells, and 6) by modification of the stator pole geometry. On the other hand, the numerical simulations show that the increase in height of the stator's poles results in decrease of natural frequency.

Based on the comparison between the numerical and analytical results it can be concluded that that analytical solution by using Jordan's law is good enough to be used as a rapid first estimation of natural frequencies for the modal shape $m = 2$. However, for precise calculation of natural frequencies the detailed 3D numerical analysis considering all geometrical and material properties of SRM need to be used.

The results obtained in this study can provide useful guidelines for further experimental testing and design of SRM machines as well as for other types of electrical machines. Namely, the results can be successfully used in further investigations on the undesirable noise and vibration emitted from the SRM which could also consider the whole stator assembly comprising the windings, the insulation components as well as the stator laminations needed for axial modal shape analysis. In addition, further investigation of adequate SRM configurations can also involve different optimization procedures; the results obtained in this study can therefore be successfully used as input data into the optimization algorithms. To conclude, the findings provided in this study can have important implication in efficient machine design planning and manufacturing process of a SRM with significantly reduced magnetically excited noise and vibration.

ACKNOWLEDGEMENT

This study was conducted within the project entitled Premium Efficiency Class Electrical Motors with ID L2-8187 (C). The authors acknowledge the project (Premium Efficiency Class Electrical Motors, ID L2-8187 (C)) was financially supported by the Slovenian Research Agency.

REFERENCES

[1] M. Yilmaz, "Limitations/capabilities of electric machine technologies and modeling approaches for electric motor design and analysis in plug-in electric vehicle applications," *Renew Sust. Energ. Rev.*, vol. 52, pp. 80-99, 2015.

[2] M. Takiguchi, H. Sugimoto, N. Kurihara, and C. Chiba, "Acoustic noise and vibration reduction of SRM by elimination of third harmonic component in sum of radial forces," *IEEE Trans. Energy Convers*., vol. 30, pp. 883-891, 2015.

[3] T. J. E. Miller, "Optimal design of switched reluctance motors," *IEEE T. Ind. Electron*., vol. 49, pp. 15-27, 2002.

[4] R. Krishnan, D. Blanding, A. Bhanot, A. M. Staley, and N. S. Lobo, "High reliability SRM drive system for aerospace applications," In: *The 29th Annual Conference of the IEEE Industrial Electronics Society (IECON 2003)*, Roanoke, VA, USA: IEEE, pp. 1110-1115, 2-6 Nov. 2003.

[5] S. Haghbin, A. Rabiei, and E. Grunditz, "Switched reluctance motor in electric or hybrid vehicle applications: A status review," In: *The 8th IEEE Conference on Industrial Electronics and Applications (ICIEA 2013)*, Melbourne, Australia: IEEE, pp. 1017-1022, 19-21 June 2013.

[6] Z. Xu, D. H. Lee, and J. W. Ahn, "Design and operation characteristics of a novel switched reluctance motor with a segmental rotor," *IEEE T. Ind. Appl*., vol. 52, pp. 2564-2572, 2016.

[7] S. Song, S. Chen, and W. Liu, "Analytical rotor position estimation for SRM based on scaling of reluctance characteristics from torque-balanced measurement," *IEEE T. Ind. Electron*., vol. 64, pp. 3524-3536, 2017.

[8] W. Wang, M. Luo, E. Cosoroaba, B. Fahimi, and M. Kiani, "Rotor shape investigation and optimization of double stator switched reluctance machine," *IEEE T. Mag.*, vol. 51, pp. 8103304, 2015.

[9] W. Cai, P. Pillay, and Z. Tang, "Impact of stator windings and end-bells on resonant frequencies and mode shapes of switched reluctance motors," *IEEE T. Ind. Appl.*, vol. 38, pp. 1027-1036, 2002.

[10] P. C. Desai, M. Krishnamurthy, N. Schofield, and A. Emadi, "Novel switched reluctance machine configuration with higher number of rotor poles than stator poles: Concept to implementation," *IEEE T. Ind. Appl.*, vol. 57, pp. 649-659, 2010.

[11] C. Lin and B. Fahimi, "Prediction of acoustic noise in switched reluctance motor drives," *IEEE T. Energy Conver.*, vol. 29, pp. 250-258, 2014.

[12] M. N. Anwar and I. Husain, "Radial force

calculation and acoustic noise prediction in switched reluctance machines," *IEEE T. Ind. Appl.*, vol. 36, pp. 1589-1597, 2000.

[13] T. Lachman, T. R. Mohamad, and G. L. A. Onyango, "Analytical methods for prediction of acoustic noise generation in switched reluctance motors," In: *IEEE International Conference on Robotics, Intelligent Systems and Signal Processing*, Changsha, Hunan, China: IEEE, pp. 226-231, 8-13 Oct. 2003.

[14] J. P. Lecointe, R. Romary, J. F. Brudny, and T. Czapla, "Five methods of stator natural frequency determination: Case of induction and switched reluctance machines," *Mech. Syst. Signal Pr.*, vol. 18, pp. 1133-1159, 2004.

[15] R. Krishnan, *Switched Reluctance Motor Drives: Modeling, Simulation, Analysis, Design, and Applications*. Boca Raton, FL, USA: CRC Press, 2001.

[16] H. Jordan, *Geräuscharme Elektromotoren: Lärmbildung und Lärmbeseitigung bei Elektromotoren*. Essen: Girardet, 1950.

[17] S. A. Long, Z. Q. Zhu, and D. Howe, "Vibration behavior of stators of switched reluctance machines," *IET Electr. Power App.*, vol. 148(3), pp. 257-264, 2001.

[18] B. T. Wang and D. K. Cheng, "Modal analysis of mdof system by using free vibration response data only," *Journal of Sound and Vibration*, vol. 311, pp. 737-755, 2008.

Selma Čorović received her Ph.D. degrees from the Faculty of Electrical Engineering, University of Ljubljana and from the University of Paris XI, France. She is as an Assistant Professor with the Department of Mechatronics, Faculty of Electrical Engineering at the University of Ljubljana. Her research interests include coupled analysis, modeling and optimization of electrical machines (generators, motors, transformers and actuators) and electromagnetics and mechanics in biomedical engineering.

Rok Benedetič received the B.Sc. degree in Electrical Engineering from University of Ljubljana, Slovenia, in 2016. His research interests include analysis and modeling of electrical machines.

Damijan Miljavec is a Full Professor with the Department of Mechatronics and is the Head of Laboratory for Electrical Machines, Faculty of Electrical Engineering, University of Ljubljana. His research interests include analysis, modeling, design and optimization of conventional and unconventional electric machines, design of actuators, introduction of new materials, EMC characteristics of electric machines and coupled analysis in electrical machines. He has co-authored several papers published in SCI indexed scientific journals, several papers in conference proceedings and one international patent.

Shielding Effectiveness Improvement of Non-Metallic Transparent Enclosures Using Gold Nano-Layer Deposition

Moharram Ghiyasvand [1], Mohammad Naser-Moghadasi [1], Abbas A. Lotfi-Neyestank [2], and Alireza Nikfarjam [3]

[1] Department of Electrical and Computer Engineering, Science and Research Branch
Islamic Azad University, Tehran, 14778-93885, Iran
m.ghiyasvand@srbiau.ac.ir, mn.moghaddasi@srbiau.ac.ir

[2] Department of Electrical Eng., Yadegar-e-Imam Khomeini (RAH) Shahre Rey Branch
Islamic Azad University, Tehran, 18155-144, Iran
aalotfi@ieee.org

[3] Faculty of New Sciences & Technologies
University of Tehran, Tehran, 14176-14418, Iran
a.nikfarjam@ut.ac.ir

Abstract ─ In this paper we present the results of a simple optically transparent enclosure with efficient electromagnetic shielding. Firstly, Indium Tin Oxide (ITO) enclosures are designed for simultaneously providing high transmittance within a visible range and good shielding effectiveness (SE), where weight reduction, small size, and transparency are challenges. In the next step, gold Nano-layer films of various thicknesses are deposited on the patterned ITO glass using the thermal evaporation method. Then, by making a trade-off between optical transparency and SE, an optimized gold film thickness is selected. To assess the proposed approach, the final experimental results of copper, ITO, and gold deposited enclosures are compared. The results showed that a 9nm gold deposited ITO enclosure, provides efficient electromagnetic shielding better than the ITO enclosure (about 15 dB better at the resonance frequency and much closer to the copper enclosure) and at the same time, acceptable optical transparency.

Index Terms ─ Deposition, gold Nano-layer, shielding effectiveness, transparent enclosure.

I. INTRODUCTION

Today, the growth of wireless communications, such as satellites and Wi-Fi connections, electromagnetic shielding of high frequencies is needed. Electrical and electronic devices are commonly housed into metallic enclosures to reduce emissions or improve their immunity. From the viewpoint of electromagnetic compatibility due to the existence of slots and apertures for signal and power cable penetration and heat dissipation, the shielding efficiency of electromagnetic enclosures is degraded [1]. The ability of an electromagnetic enclosure to reduce the effect of undesired emission is represented by shielding effectiveness (SE). SE is defined as the ratio of field strength in the absence of an enclosure to the presence of an enclosure [2]. Metallic enclosures with apertures have been studied extensively in other previous work [3, 4]. Also, analytical models have been developed for a fast and accurate estimation of the metallic enclosures SE [5-7]. Nonetheless, a metallic enclosure cannot be considered as a good candidate for electromagnetic shielding, where weight, size reduction, and transparency are challenging.

Although meta-material slabs can provide good shielding with a reduced weight and size as well as can be tailored to obtain frequency selectivity [8], they are challenging especially when an optimum condition between optical transparency and SE is necessary.

Recent attempts to find transparent materials with high SE and good optical transparency have led to technological solutions [9] for applications such as displays of electronic devices, monitors, electrical panels, fashion electronic devices and integration with solar cells in Nano and cube satellites. Transparent enclosures can be realized on transparent conductive films, such as Indium tin oxide (ITO), fluorine-doped tin oxide, and silver-coated polymer film. Among the transparent conductors, ITO is more desirable as it offers a reasonable trade-off between optical transparency and minimum electrical resistivity [10-12]. However, the practical application of transparent ITO enclosures has been limited by their lower SE rather than metallic enclosures [13]. In recent years, a lot of effort has been

Submitted On: June 20, 2017
Accepted On: October 4, 2017

made to fabricate transparent composite films with high SE. This has led to the usage of nanoparticle materials. For example graphene based composites have been used to obtain better SE for transparent conductive films [14-16]. The authors in [17] have attached a monolayer CVD graphene film on quartz substrate to a transparent ITO enclosure. Although, result of the proposed enclosure has demonstrated better electromagnetic shielding, this graphene loaded ITO enclosure has been considered entirely closed as there were no apertures in it. So, its practical application has been reduced dramatically.

In this paper, we provide a practical and simple solution to improve the SE of the transparent ITO enclosure with a circular aperture. In the first step, CST simulations are used to find the SE of ITO enclosures. Then, an optimum gold Nano-layer thickness is selected to make a trade-off between SE and the optical transparency of gold deposited ITO enclosure. Finally, in order to demonstrate the effectiveness of the method, performance results of copper, ITO glass, and gold Nano-layer deposited enclosures are compared.

This paper is organized as follows: In Section II, we discuss the characteristics of transparent conductors and the design and analysis of transparent enclosures is presented. In Section III, the fabrication of transparent ITO enclosure is described. Gold Nano-layer deposition using thermal evaporation technique is described in Section IV. Also, the selection of optimum gold Nano-layer thickness is presented in this section. Measurement results of copper, ITO and gold Nano-layer deposited enclosures are provided in Section V. The conclusion is given in Section VI.

II. TRANSPARENT ENCLOSURE

A. Transparent conductive films

In studies involving optically transparent conductive films, the performance of different materials has been assessed, among which, ITO is highly regarded. ITO is an n-type semiconductor with a wide energy gap (more than 3.5 eV) that offers a good trade-off between high optical transparency and minimum electrical resistivity in the visible light spectrum. An ITO film without layering on a substrate can be considered a good conductor to use in an enclosure, if its sheet resistance R_{sh} is low to restrict the ohmic losses and its thickness is high enough to limit skin depth losses. The optical transparency of the ITO film is estimated by using (1) [18]:

$$T \cong e^{-\frac{2T_c}{\delta}}, \tag{1}$$

where, T_c is the conductive film thickness and δ is the skin depth for visible wavelengths. According to [19], the sheet resistance of the ITO film can be obtained by using (2), where ρ is the resistivity of the ITO film:

$$R_{sh} = \frac{\rho}{T_c}. \tag{2}$$

One can see from (1), that a higher optical transparency needs thinner films while (2) shows that lower sheet resistance requires thicker films. In this paper, in order to determine the effects of gold deposition, we have used a 160nm thick ITO film with high optical transparency of about 89% and sheet resistance of 10 Ω⁄sq.

B. Transparent enclosure design

The Robinson et al. model is a simple analytical model based on transmission line theory that can be used for SE estimation of metallic enclosures with infinite conductivity. It has been developed for practical metallic enclosures with finite conductivity [20]. It still cannot analyse transparent enclosures accurately, due to its inability to take into account multi-layer panel effects. In this paper, we used three layer transparent panels including transparent dielectric (such as Glass, PET polymer sheet, and Plexiglas) and conductive transparent films (see Fig. 1). Hence, to analyse transparent enclosures, we have performed a 3D full wave electromagnetic analysis using the CST Microwave Studio based on the Finite Integration Technique and setting the proper characteristics of the materials constituting the enclosure.

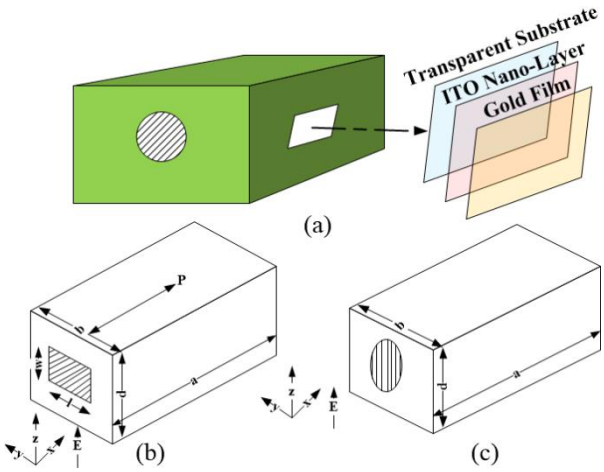

Fig. 1. Transparent enclosure: (a) panel configuration, (b) rectangular aperture, and (c) circular aperture.

SE is the most important factor in metallic enclosure performance while, optical transparency as well as the SE factor should also be considered in transparent enclosures. Therefore, by making a trade-off between these two factors, optimized ITO and glass thickness selection is necessary. So, based on CST optimization tools and Equations (1)–(2), we have selected optimum thicknesses of layers. As a result, we have selected

160nm thick ITO films that are mounted on a transparent dielectric substrate to make two-layer transparent panels. Such transparent enclosures with various dimensions, substrate thickness, and apertures (see Table 1) has been simulated and exposed to the normal incident of the plane wave. The electric field has been calculated in the center of enclosures. Also, for a better comparison between SE of transparent and metallic enclosures, copper enclosures with the same dimensions, apertures and thickness (equal to the substrate thickness) have been analysed, too.

Table 1: Characteristics of ITO Enclosures

Sample	Substrate	Substrate Thickness	Enclosure Dimensions
1	PET Polymer	0.18mm	100mm × 100mm × 100mm
2	Plexiglas	1mm	300mm × 120mm × 300mm
3	Glass	1.5mm	90mm × 40mm × 90mm
4	Glass	2.2mm	100mm × 50mm × 100mm

SE results of ITO enclosures have been given in Fig. 2. One can see there is a significant difference between the SE of ITO and copper enclosures. Therefore, in practical applications, ITO enclosure shielding performance should be improved as will be discussed in the Section V.

III. ITO GLASS ENCLOSURE FABRICATION

Based on previous results, one can see that an ITO enclosure with square and circular aperture has better SE than one with a rectangular aperture (similar to a metallic one) [20, 21]. As observed in Fig. 2, as the thickness of enclosures is increased, the SE difference between transparent and metallic cases is higher. However, in practical application of transparent enclosure, the thickness should be lower than 2 mm, because of weight and size challenges. Hence, in order to consider the worst case, we have chosen 2.2 mm thick borosilicate glass as a substrate for transparent panels. Additionally, in order to simplify the manufacturing process (cutting and drilling); we have taken ITO enclosures with a circular aperture. Without any damages to the generality of the work, we have considered ITO enclosure dimensions of 100mm × 50mm × 100mm with a circular aperture radius of 5mm. 150nm thick ITO films have been deposited on the substrates using RF sputtering deposition technique.

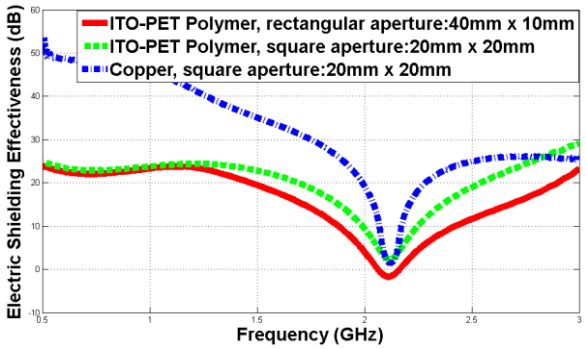

(a)

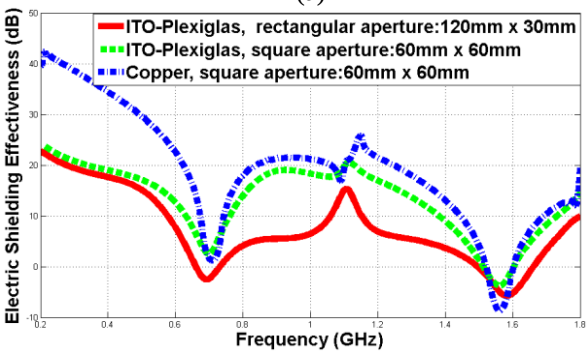

(b)

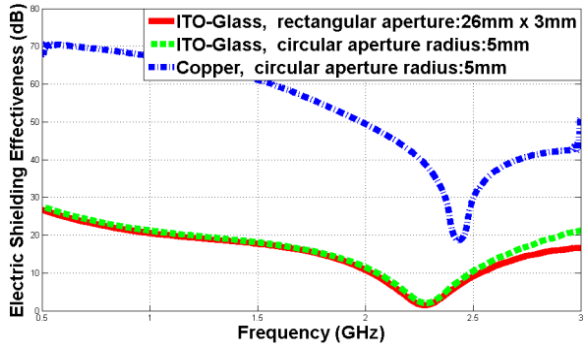

(c)

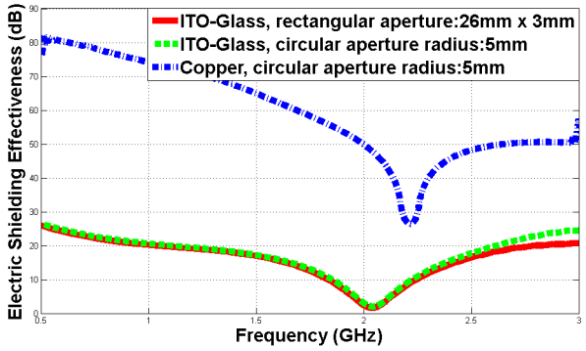

(d)

Fig. 2. SE calculation of transparent enclosures with various panels and dimensions: (a) sample 1, (b) sample 2, (c) sample 3, and (d) sample 4.

In order to maintain conductivity at the edges of the enclosures, panels are connected by a silver paste internally and glue strips of copper externally (see sample A, Fig. 3).

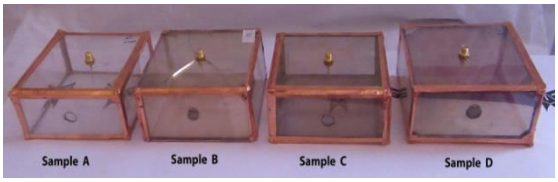

Fig. 3. Transparent enclosures have been fabricated using various transparent panels (see Table 2).

IV. GOLD NANO-LAYER DEPOSITED ITO ENCLOSURE

A. Gold Nano-layer deposition

As predicted in previous section, based on our measurement results (as observed in Fig. 4), the SE of ITO glass enclosure is very low compared to the metallic enclosure (with the same dimensions, aperture and the thickness equal to the substrate thickness).

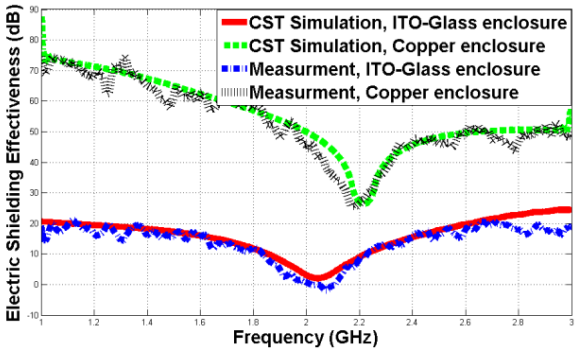

Fig. 4. SE Comparison of copper and ITO enclosures with the same dimensions, thickness and aperture.

To improve the SE, we used gold Nano-layers that homogenously deposited on the ITO glass panels, using thermal evaporation technique. We choose gold due to its good oxidation resistance, low penetration depth, and high electrical conductivity. This method is based on reducing the surface resistance of the panels to obtain a better conductor and therefore good SE. One technique is to use multilayer conductors. In such a case, several layers are placed in parallel, one on top of the other, and therefore the overall sheet resistance is decreased as observed in (3) [19]:

$$\frac{1}{R_{sh-Total}} = \frac{1}{R_{sh-ITO}} + \frac{1}{R_{sh-Gold}}, \qquad (3)$$

where, R_{sh-ITO} and $R_{sh-Gold}$ are the sheet resistances of the ITO film and gold Nano-layer, respectively.

B. Thermal evaporation deposition technique

Thermal evaporation is utilized extensively to deposit Nano-layer films of materials on the substrates in semiconductor production. In this paper, gold Nano-layer films of various thicknesses have been deposited on the ITO glass panels by this technique. The process has been performed at an atmospheric pressure of 1e-5 and supply current of 100A. Before deposition, the panels were cleaned by rinsing them in a detergent solution and later in deionized water. They were finally dried with N_2 gas.

C. Selection the optimum thickness of gold film

Here we propose a practical approach to improve SE, based on gold Nano-layer deposition on the patterned ITO glass panels, the configuration of which has been shown in Fig. 1. The first step is to make a trade-off between SE and optical transparency, and the second step is the selection of the appropriate gold Nano-layer thickness. Therefore, gold Nano-layers of various thicknesses in the range of 3nm to 19nm have been deposited on the patterned ITO glass using the thermal evaporation technique.

Results from optical transparency measurements show that thicknesses higher than 13nm lead to very low transparency of about 50% (Fig. 5). On the other hand, based on the results of our simulation and also Equation (3), thicknesses lower than 3nm cannot improve SE, effectively.

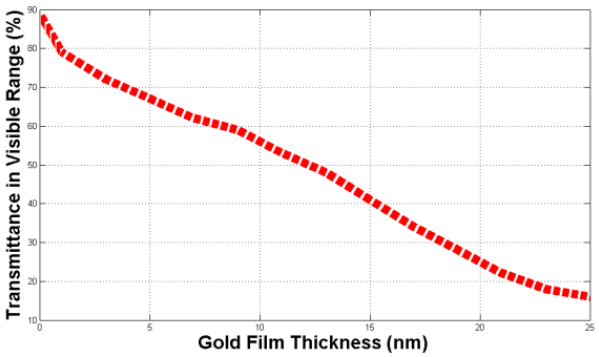

Fig. 5. Optical transparency results of gold deposited ITO glass panels at 550 nm wavelength, versus gold film thickness.

In the final step, 5nm, 7nm, and 9nm gold deposited panels were selected to fabricate transparent enclosures. As mentioned in Section IV, to connect the edges, gold deposited ITO glass panels were connected using silver glue internally and copper adhesive tape externally. Fabricated transparent enclosures can be seen in Fig. 3. Also, panels used in these enclosures have been described in Table 2.

Table 2: Transparent panel samples

Sample	Panel Layers	Layer Thicknesses
A	ITO-Glass	160nm - 2.2mm
B	Gold-ITO-Glass	5nm - 160nm - 2.2mm
C	Gold-ITO-Glass	7nm - 160nm - 2.2mm
D	Gold-ITO-Glass	9nm - 160nm - 2.2mm

V. RESULT AND DISCUSSION

A. Measurement

The SE of transparent enclosures was measured within a frequency range of 1 GHz to 3 GHz in an EMC chamber. A standard horn antenna was used to radiate electromagnetic waves, and an electric field measurement probe has been placed at the center of the enclosure (Fig. 6). The SE results of transparent enclosures have been shown in Fig. 7 (a).

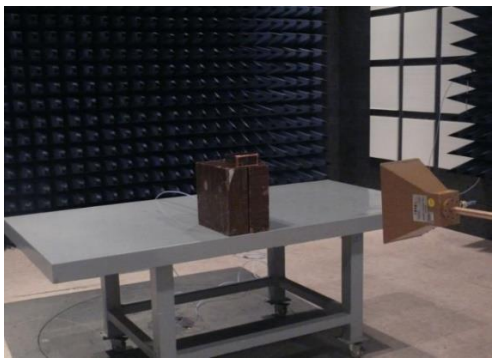

Fig. 6. SE measurement setup in EMC chamber.

Also, the optical properties of the composite panels are characterized by spectrophotometry.The transmittance spectra can be recorded within the 300nm–1000nm range by a spectrophotometer for normal incidence. The optical transparency measurements for the mentioned panels, shown in Fig. 7 (b), were conducted using a high resolution optical spectrometer in the optical laboratory.

B. Discussion

ITO glass enclosures can provide proper shielding and good transparency, simultaneously, but as discussed in the previous section its SE should still be improved to obtain SE closer to metallic enclosures. A homogenous deposition base on gold Nano-layer has been proposed in this paper.To assess the performance of the improvement method, a 2.2mm thick copper enclosure with the same dimensions and aperture (equal to the ITO enclosures) has been fabricated and measured too. The performance results of copper, ITO glass, and gold deposited ITO glass enclosures are compared in Fig. 8 (a) and Fig. 8 (b). As predicted by analysis results, measurement results show that, gold Nano-layer deposition increases the SE significantly and reduces optical transparency which verifies the theoretical relationships (1) to (3).

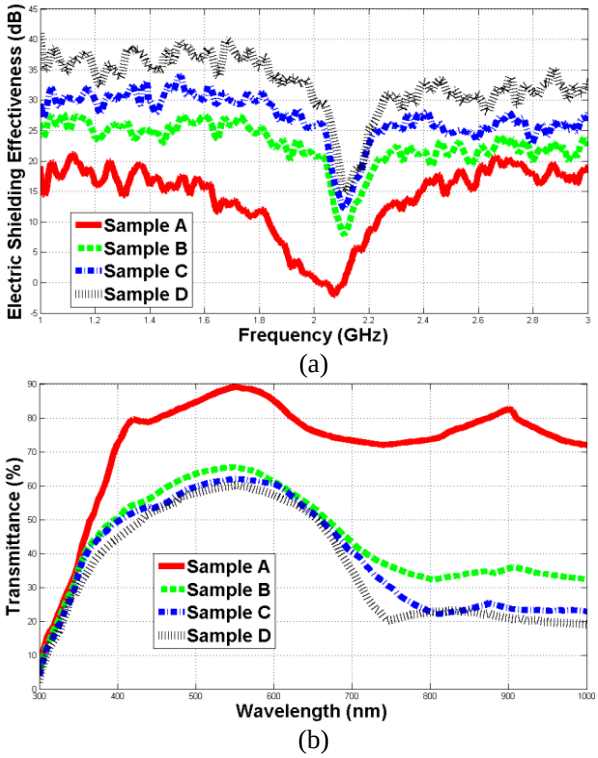

Fig. 7. Performance of transparent enclosures: (a) measured SE, and (b) measured optical transparency.

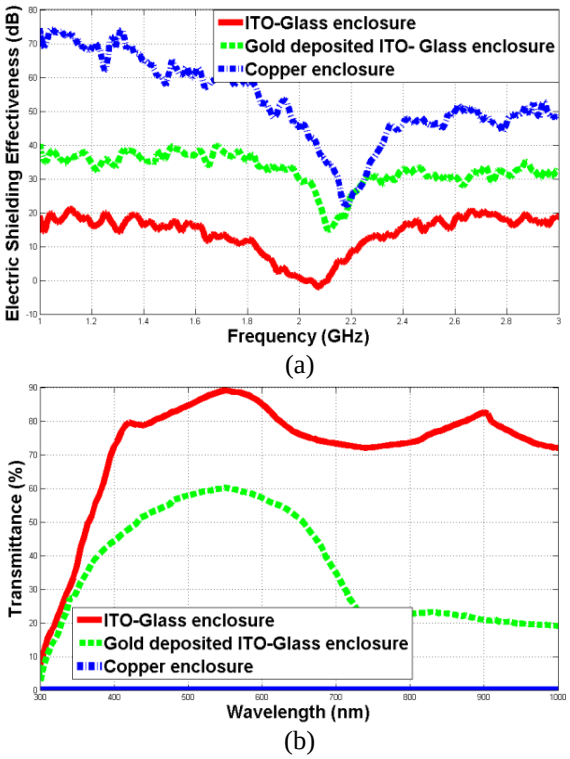

Fig. 8. Performance comparison between transparent and metallic enclosures: (a) SE and (b) optical transparency.

Therefore, optimized performance for transparent enclosures has been obtained by making a trade-off between SE and optical transparency factors. From the results, it can be inferred that while ITO glass enclosure does not have desirable SE, 9nm gold Nano-layer deposited ITO glass enclosure has more than 15 dB better SE at the resonance frequency (and much closer to the SE of metallic enclosure) as well as acceptable optical transparencies for practical applications (about 60% transmittance in 550nm wavelength), while a copper enclosure cannot provide any transmittance in the visible range. As shown in this paper, the proposed method has been used for 2.2mm enclosure (which is usually the worst case for transparent applications). This method improves the SE of ITO glass enclosures more efficiently (compared to the metallic enclosure performance), especially when the thickness of the enclosure walls is reduced.

VI. CONCLUSION

Metallic enclosures cannot be good candidates for electromagnetic shielding, where weight, size reduction, and transparency are challenging.

In this paper, we have proposed gold-ITO enclosures that can overcome mentioned challenges. Since an ITO enclosure cannot provide the desirable SE, in this paper we have proposed a practical solution to improve the performance of transparent enclosures. Gold Nano-layer films of various thicknesses were deposited on the patterned ITO glass panels to achieve better SE. Finally, by making a trade-off between SE and optical transparency, the optimum thickness of gold Nano-layer was selected. To assess the performance improvement method, copper, ITO, and gold deposited ITO enclosures have been compared. The results showed that a transparent enclosure with 9nm gold Nano-layer deposited ITO glass panels provides efficient SE and the same time acceptable transmittance within a visible range, while metallic enclosures cannot overcome transparency challenges. The proposed technique can improve the SE of ITO glass enclosures efficiently, especially when the thickness of the enclosure walls is reduced.

REFERENCES

[1] M. Bahadorzade and A. A. Lotfi-Neyestanak, "A novel and efficient technique for improving shielding effectiveness of a rectangular enclosure using optimized aperture load," *Elektronika IR Elektrotechnika*, vol. 18, no. 10, pp. 89-92, June 2012.

[2] M. P. Robinson, T. M. Benson, C. Christopoulos, J. F. Dawson, M. D. Ganley, A. C. Marvin, S. J. Porter, and D. W. P. Thomas, "Analytical formulation for the shielding effectiveness of enclosures with apertures," *IEEE Trans. on EMC*, vol. 40, pp. 240-248, 1998.

[3] R. Araneo and G. Lovat, "Fast MOM analysis of the shielding effectiveness of rectangular enclosures with apertures, metal plates and conducting objects," *IEEE Trans. on EMC*, vol. 51, no. 2, pp. 274-283, 2009.

[4] A. C. Marvin, J. F. Dawson, S. Ward, L. Dawson, J. Clegg, and A. Weissenfeld, "A proposed new definition and measurement of the shielding effect of equipment enclosures," *IEEE Trans. on EMC*, vol. 46, no. 3, pp. 459-468, 2004.

[5] E. Liu, P. A. Du, W. Liu, and D. Ren, "Accuracy analysis of shielding effectiveness of enclosures with apertures: A parametric study," *IEEE Trans. on EMC*, vol. 56, no. 6, pp. 1396-1403, 2014.

[6] E. Liu, P. Du, and B. Nie, "An extended analytical formulation for fast prediction of shielding effectiveness of an enclosure at different observation points with an off-axis aperture," *IEEE Trans. on EMC*, vol. 56, no. 3, 2014.

[7] T. R. SureshKumar, C. Venkatesh, P. Salil, and B. Subbarao, "Transmission line approach to calculate the shielding effectiveness of an enclosure with double-layer frequency selective surface," *IEEE Trans. on EMC*, vol. 57, no. 6, 2015.

[8] D. Seetharamdoo, M. Berbineau, A. C. Tarot, and K. Mahdjoubi, "Evaluating the potential shielding properties of periodic meta-material slabs," *in* 2009 *Proc. IEEE Europe International Symposium*, pp. 1-4, 2009.

[9] M. S. Sarto, R. L. Voti, F. Sarto, and M. C. Larciprete, "Nanolayered lightweight flexible shields with multidirectional optical transparency," *IEEE Trans. on EMC*, vol. 47, no. 3, pp. 602-611, August 2005.

[10] M. R. Haraty, M. Naser-Moghaddasi, A. A. Lotfi-Nyestanak, and A. Nikfarjam, "Circular ring optically transparent antenna for ultra-wideband applications," *ACES Journal*, vol. 30, no. 2, pp. 208-212, February 2015.

[11] M. R. Haraty, M. Naser-Moghaddasi, A. A. Lotfi-Nyestanak, and A. Nikfarjam, "Transparent flexible antenna for UWB application," *ACES Journal*, vol. 13, no. 11, pp. 1426-1430, December 2016.

[12] M. R. Haraty, M. Naser-Moghaddasi, A. A. Lotfi-Nyestanak, and A. Nikfarjam, "Improving the efficiency of transparent antenna using gold Nano layer deposition," *IEEE Antennas and Wireless Propagation Letters*, vol. 15, pp. 4-7, 2016.

[13] A. Tamburrano, S. Greco, G. D. Bellis, A. G. D'Aloia, and M. S. Sarto, "Transient shielding performances against UWB pulses of transparent enclosures loaded with Nano-composites for resonances damping," *in* 2012 *Proc. IEEE Europe International Symposium on EMC*, pp. 1-6, 2012.

[14] Y. Chen, H. B. Zhang, Y. Huang, Y. Jiang, W. G. Zheng, and Z. Z. Yu, "Magnetic and electrically

conductive epoxy/grapheme/carbonyl iron Nano-composites for efficient electromagnetic interference shielding," *Composite Sci. and Tech.*, vol. 118, pp. 178-185, September 2015.

[15] Y. Chen, Y. Wang, H. B. Zhang, X. Li, C. X. Gui, and Z. Z. Yu, "Enhanced electromagnetic interference shielding efficiency of polystyrene/ graphene composites with magnetic Fe3O4 nanoparticles," *Carbon*, vol. 82, pp. 67-76, February 2015.

[16] X. Xia, Y. Wang, Z. Zhong, and G. J. Weng, "A theory of electrical conductivity, dielectric constant, and electromagnetic interference shielding for lightweight graphene composite foams," *Journal of Applied Physics*, vol. 120, pp. 085102, 2016.

[17] Y. T. Zhao, B. Wu, Y. Zhang, and Y. Hao, "Transparent electromagnetic shielding enclosure with CVD grapheme," *Applied Physics Letters*, vol. 109, pp. 103507, September 2016.

[18] A. Porch, D. V. Morgan, and R. M. Perks, "Electromagnetic absorption in transparent conducting films," *Journal of Applied Physics*, vol. 95, no. 9, pp. 4734-4737, May 2004.

[19] F. Colombel, E. Motta Cruz, X. Castel, M. Himdi, G. Legeay, and S. Vigneron, "Ultrathin metal layer, ITO film and ITO/Cu/ITO multilayer towards transparent antenna," *IET Sci. Meas. and Tech.*, vol. 3, no. 3, pp. 229-234, 2009.

[20] F. T. Belkacem, M. Bensetti, A. G. Boutar, D. Moussaoui, M. Djennah, and B. Mazari, "Combined model for shielding effectiveness estimation of a metallic enclosure with apertures," *IET Sci. Meas. and Tech.*, vol. 5, no. 3, pp. 88-95, 2011.

[21] M. A. Khorrami, P. Dehkhoda, R. Moini, and S. H. H. Sadeghi, "Fast shielding effectiveness calculation of metallic enclosures with apertures using a multiresolution method of moments technique," *IEEE Trans. on EMC*, vol. 52, no. 1, pp. 230-235, 2010.

Moharram Ghiyasvand was born in Malayer, Iran (1980). He received his B.Sc. degree in Electrical Eng. (2002) and M.Sc. degree in Communication Eng. (2005) from Tarbiat Moddares Unversity, Tehran, Iran. Since 2011, he has been working towards his Ph.D. degree at Islamic Azad University, Science & Research Branch in Tehran, Iran. His main areas of research interests are Microwave circuits & antennas and Electromagnetic absorbing and shielding materials.

Mohammad Naser-Moghadasi was born in Saveh, Iran (1959). He received his B.Sc. degree (1985) from the Leeds Metropolitan University, UK and his Ph.D. (1993) from University of Bradford, UK. He was offered then a two years Post Doc. to pursue research on Microwave cooking of materials at University of Nottingham, UK. From 1995, he joined Islamic Azad University, Science & Research Branch. His main areas of research interests are Microwave antennas and RF MEMS. He is Member of the Institution of Engineering and Technology and the Institute of Electronics, Information and Communication Engineering (IEICE).

Abbas Ali Lotfi-Neyestanak was born in Tehran, Iran. He received his B.Sc. degree (1993), M.Sc. degree (1997) and Ph.D. degree (2004) from Iran University of Science and Technology (IUST) Tehran, Iran. Currently, he is collaborating with the Department of Electrical Engineering, University of Waterloo, Ontario, Canada. His main areas of research interest are Microwave circuits and antennas, EMC and Optimization methods in electromagnetic. He is a Senior Member of IEEE.

Alireza Nikfarjam was born in Tehran in 1975. He obtained his B.Sc. and M.Sc. degrees in Electronics both in Iran in 1998 and 2001, respectively. He obtained his Ph.D. in Micro-electronics from K. N. Toosi University of Technology (2007), Tehran, Iran. He joined the Sharif University of Technology in Tehran as Post-Doctoral Researcher to work on Nano-sensors (2009). Then he joined the Faculty of New Sciences and Technologies of University of Tehran as Assistant Professor (2011). His research interests are, MEMS & NEMS and Organic Electronics.

Characterization of 4 Element Compact Microstrip Patch Antenna Array for Efficient Null Steering

B. Kaur, A. Marwaha, and S. Rani

Department of Electronics and Communication Engineering
Sant Longowal Institute of Engineering and Technology, Longowal, Punjab-148106, India
baljinderkaursidhu@rediffmail.com, marwaha_anupma@yahoo.co.in, surekhagarg9@gmail.com

Abstract ─ Null steering in radiation pattern of linear antenna array is essential for minimizing degradation in signal-to-noise ratio performance due to undesired interference. High directivity and miniaturization are other key factors for proficient design of antenna arrays. Thus, the development of small sized antenna elements with high directivity is strategic point of interest. Consequently, the four element bowtie patch antenna array has been designed and simulated using IE3D software, and compared with conventional rectangular patch antenna array. Null steering is performed by varying element excitations in isotropic antenna array, rectangular patch antenna array and bowtie patch antenna array with main emphasis on position and depth of nulls to analyze the radiation characteristics of the designed models. The mutual coupling effects at different inter-element spacings are also presented for both the designed arrays. It has been observed that using bowtie patches as the element in the array brings about comparatively more effective null steering, and enhances the performance of the array as compared to the conventional rectangular patches.

Index Terms ─ Antenna array, isotropic elements, mutual coupling, non-isotropic elements, null steering, Schelkunoff polynomial method.

I. INTRODUCTION

The demand for extended functionalities provided by wireless communications has risen beyond all expectations over the last decade. With the growing demand for wireless communications, the need for better coverage, improved capacity and higher transmission has risen. In wireless communication systems, null steering is of great significance for rejecting unwanted interference while receiving the desired signal. Null steering in antenna radiation pattern finds its applications in radar, sonar and many communication systems for minimizing degradation in signal-to-noise ratio performance due to undesired interference [1]. Further, the electromagnetic interferences between radiating elements in an antenna array, is expressed by the modification of the surface currents distribution. This phenomenon, called mutual coupling, depends on the antenna type and the distance between its elements. The coupling between the elements of antenna array has a great importance in the design of antenna arrays, because it may cause a change in the radiation pattern.

Methods of null steering in antenna arrays including controlling the amplitude-only, phase only, position only and complex amplitude, i.e., amplitude and phase both have been extensively used for isotropic antenna arrays. Null steering by controlling the complex weights involves larger degree of freedom, which makes it the most effective but also most costly method because of the controllers used for phase shifters and variable attenuators for each array element [2]. Moreover, the computational time to find the values of element amplitudes and phases also increases with the increase in number of elements in the array [3]. The phase-only and position-only nulling methods are inherently non-linear and, thus cannot be solved by analytical methods without any approximation. The nulling equations for phase only control can be linearized by assuming that the phase perturbations are small, but it cannot be used to place nulls at symmetric location with respect to the main beam. Methods based on non-linear optimization techniques [4] have been proposed for steering the nulls symmetrically with respect to the main beam, but the resultant patterns of these methods have significant pattern distortion because of large phase perturbations used. Moreover, null steering with small phase perturbations results in increased side lobe level (SLL) in the direction symmetric to nulling direction with respect to the main beam [5]. The nulls can be steered in symmetrical directions with respect to the main beam by element position control method using a mechanical driving system such as servomotors [6]. Null steering with amplitude-only control, make use of a set of variable attenuators to adjust the element amplitudes. The number of attenuators and the computational time are halved, if the element amplitudes have even symmetry about the centre of the array [7].

Submitted On: July 7, 2017
Accepted On: October 4, 2017

There has been a lot of research work being carried out on null steering of antenna array of isotropic elements using various optimization techniques such as Genetic Algorithm (GA), Simulated Annealing (SA), Particle Swarm Optimization (PSO), Artificial Bee Colony (ABC), Tabu Search Optimization, Bacterial Foraging Algorithm, Backtracking Search Optimization Algorithm [2, 8-12] and many more. All these methods have their own advantages and drawbacks, but have been less explored for null steering of arrays of non-isotropic elements. Choudhari et al. have used Schelkunoff polynomial method (SPM) for phase controlled null steering of microstrip patch antenna array and found it to be an effective analytic approach to synthesize the null controlled patterns [13]. Dwivedi and Banerjee have applied SPM in combination with PSO for null steering of array of isotropic elements [14]. Much of the work on null steering has been implemented for isotropic antenna arrays. However, there has been relatively little effort in analyzing the use of non-isotropic antenna elements in the array design. An antenna element to be used in array environments should have small size and broad patterns. The scanning performance of an array is generally determined by the element spacing which, in turn, is limited by the element size, hence, the physical size of the element is an important consideration in the design of an array. The better approach to address these issues is to explore the design and analysis of antenna array of non-isotropic antenna elements.

In this paper, a performance comparison of null steering of isotropic antenna array and non-isotropic linear antenna arrays consisting of rectangular and bowtie patches is presented. The nulls are imposed in the direction of interference by using Schelkunoff polynomial method for controlling the excitation amplitudes of array elements instead of phase and position control due to their limitations as discussed above. Hence, a Matlab code has been generated to derive the excitation amplitudes for isotropic and non-isotropic elements and the data is then utilized in the design of 4-element isotropic and non-isotropic microstrip patch antenna array for demonstrating the null steering of the designed antenna arrays.

II. DESIGN SPECIFICATIONS OF ARRAY AND COPLANAR WAVEGUIDE FEED SECTION

Antenna array size reduction has attracted increasing interest in wireless communication so as to reduce the total size of devices. One way to reduce the total size of an array antenna is to place elements of an antenna array close to each other. But the factor called mutual coupling that effects the radiation pattern, depends on inter element spacing and causes undesirable effects on antenna characteristics [15]. Therefore, the selection of appropriate design parameters is prerequisite for performance evaluation of the designed models. The process of antenna array design involves the selection of elements and geometry of array, and the determination of the excitations of array elements required for achieving desired radiation characteristics with prescribed location of the major lobe and nulls, SLL, and beamwidth [16].

As reported in literature the antenna pattern synthesis can be classified into several categories. One of these groups requires antenna patterns with narrow beams and low side lobes. This guarantees the radiating or receiving energy to be more focused in specific directions. Various techniques such as the binomial method, Dolph–Chebyshev method, and Taylor line-source are proposed to serve this purpose.

Another group requires that the antenna patterns exhibit a desired distribution in the entire visible region, which is also referred to as beam shaping. A typical example is the design of a sector beam pattern, which allows the antenna array to have a wider angular coverage. This is usually accomplished by using the Fourier transform technique and the Woodward–Lawson method.

A third group usually requires that the antenna patterns possess nulls in desired directions. This property is widely used in smart antenna systems to eliminate the interference from specific noise directions. The Schelkunoff polynomial method is an effective approach to synthesize the null controlled patterns.

Although existing designs offer excellent performance, many other considerations such as miniaturization of antennas and increased directivity have become important due to the increasing demand for small antennas as a result of the rapid development in wireless communications. The bowtie antenna originally proposed by Lodge demonstrates these benefits [17].

Considering the performed investigation in wideband antenna categories, two antenna geometry types: rectangular and bowtie patch antennas have been selected for present study. Both the rectangular patch antenna and bowtie patch antenna shown in Fig. 1 (i) have been designed to operate at resonant frequency of 4.9 GHz. The substrate material that is used is FR4 with dielectric constant 4.4, thickness of 1.6 mm and loss tangent 0.02. The essential parameters for the design of the two antennas, calculated using analytical equations given in [18] and [19] are presented in Table 1.

The coplanar waveguide antenna feeding operates well in wideband frequency to field matching and impedance transforming and they can also be printed on single side of the substrate. For the antenna arrays being studied, the 50 ohm CPW transmission line has been designed with metal strip width $2a = 1.8$ mm and gap dimension of 0.22 mm, calculated using equations given in [20]. The width of CPW feeding structure is

similar to the width of the patch. For rectangular patch antenna L_g = 12.9 mm and W_g = 8.18 mm. For bowtie patch antenna L_g = 8 mm and W_g = 3.88 mm.

Table 1: Dimensions of antenna elements

Antenna Element	Dimensions	
Rectangular Patch	Length of rectangular patch (L)	14.06 mm
	Width of rectangular patch (W)	18.6 mm
	Area	261.52 mm^2
Bowtie Patch	L/2	7.07 mm
	W	10 mm
	W_C	1.0 mm
	S	10 mm
	Area	55 mm^2

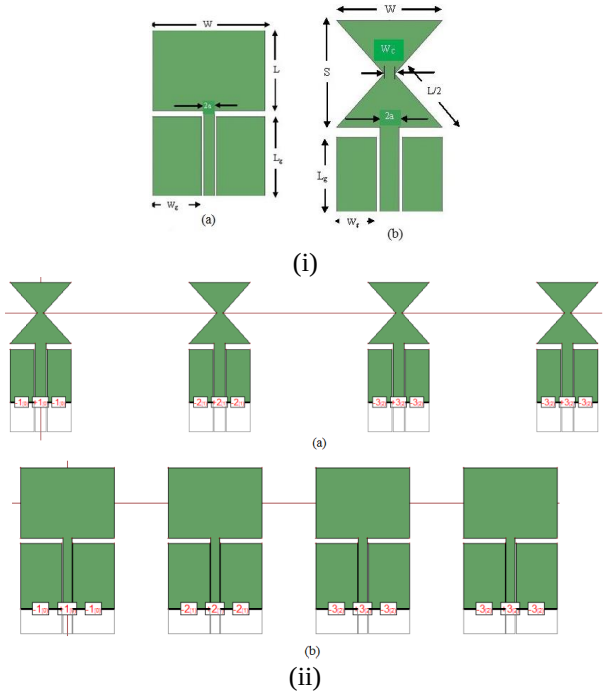

Fig. 1. (i) Geometries of CPW fed: (a) rectangular patch antenna, and (b) bowtie patch antenna. (ii) Geometry of 4-element: (a) bowtie patch antenna array, and (b) rectangular patch antenna array.

The theoretical calculations are verified by simulating the antenna in IE3D software and thereafter arrays of 4-elements with inter element spacing of 29.18 mm (λ/2) are designed and simulated.

III. ARRAY SYNTHESIS USING SCHELKUNOFF POLYNOMIAL METHOD

The null controlled patterns can be generated using Schelkunoff polynomial method [16]. The method is used to calculate the elements excitations from the required number of nulls and their positions taken as input. The array factor for an N-element array with equal spacing, non-uniform amplitude, and progressive phase excitation, is given by:

$$AF = \sum_{n=1}^{N} a_n e^{j(n-1)(kd\cos\theta+\beta)} = \sum_{n=1}^{N} a_n e^{j(n-1)\psi}, \quad (1)$$

where,
N = number of elements;
a_n = amplitude weight at element n;
$\Psi = kd\cos\theta + \beta$;
$k = 2\pi/\lambda$ = wave number;
λ = signal wavelength;
d = spacing between the elements;
θ = an incidence angle of signal from the array normal;
β = progressive phase.

The array factor of an N-element array is a polynomial of degree N−1 and therefore it has N − 1 zeros. By proper placement of the zeros on the z-plane, a desired array factor can be designed.

Let $Z = e^{j\psi} = e^{j(kd\cos\theta+\beta)}$,

$$AF = \sum_{n=1}^{N} a_n Z^{(n-1)} = a_1 + a_2 Z + a_3 Z^2 + \ldots + a_N Z^{(N-1)}, \quad (2)$$

The above equation is simply a polynomial in the complex variable z. Recall that a polynomial of order N has N zeros which may be complex. The polynomial for the AF above is of order N-1 zeros. If the zeros are numbered starting from one, the zeros will be 1, 2, ..., N-1. The AF is then rewritten as:

$$AF = a_n(Z - Z_1)(Z - Z_2)(Z - Z_3)\ldots(Z - Z_{(N-1)}), \quad (3)$$

where Z_1, Z_2, Z_3 … Z_{n-1} are roots of the polynomial. The roots Z_n of the polynomial can be positioned on, inside or outside the unit circle. The roots Z_n that lie on the unit circle contribute to the nulls in the radiation pattern in the fixed directions θ_1, θ_2, θ_3 … θ_{N-1}, and a_1, a_2 … a_n are the corresponding element excitations which can be obtained by equating (2) and (3).

Hence, we can choose the zeros Z_n to be whatever we want corresponding to the nulls θ_n as:

$$Z_n = e^{j(kd\cos\theta n+\beta)},$$

and then figure out what the weights a_n should be to give us the same pattern.

IV. RESULTS AND DISCUSSION

For investigating the null placement in non isotropic antenna array, the proposed array geometries (Fig. 1 (ii)) of bowtie microstrip patch and rectangular microstrip patch elements shown in Fig. 1 (i) have been designed and simulated using IE3D on a personal computer with Intel Core i7 processor running at 3.40 GHz with 4 GB RAM, and the performance of the

two has been evaluated for different amplitude ratios.

Based on Schellkunoff polynomial method, in 4 element array 3 nulls can be oriented along direction of interference. In this work it is intended to impose two nulls at the peaks of the two side lobes (θ_1 = 45° and θ_2 = −45°) and the third null at 155° by changing the amplitude ratio to 0.395:1:1:0.395 as calculated by Schelkunoff polynomial method.

The elevation pattern gain plots shown in Fig. 2 (i) and Fig. 3 depict the symmetric patterns with respect to the main beam because of the element-amplitude's symmetry around the center element of the array. Hence, null placement at one side of the main beam results in occurrence of an image null at the other side of the main beam.

In all the three cases, three nulls have been steered to 45°, −45° and 155° by controlling only the element amplitudes as calculated using Equations (2) and (3). With the change in amplitude, the side lobe level decreases from −12.29 dB to −25.34 dB for rectangular antenna array and from −13.31 dB to −25.5 dB for bowtie antenna array. For rectangular antenna array the NDL decreases from −16.57 dB to −27.14 dB at 45°. Null steering is achieved better in bowtie antenna array with considerable decrease in NDL from −22.59 dB to −31.75 dB.

The 2D radiation patterns of the two arrays obtained for different amplitudes are shown in Fig. 2 (ii) and Fig. 4. It can be clearly observed from the 2D radiation patterns that nulls have been successfully steered to desired location by changing the amplitude as obtained by Schelkunoff polynomial method. Further the maximum gain of the major lobe decreases from 6.76 dBi to 6.3 dBi for bowtie antenna array, whereas for rectangular antenna array it decreases from 7.92 dBi to 7.3 dBi.

It can be observed that null steering has been successfully achieved for both the isotropic and non-isotropic patch arrays. The comparative analysis on the basis of position and depth of nulls is presented in Table 2. It can be clearly depicted from the Fig. 2 (i) and Fig. 3 that the pattern symmetry is retained in all the three cases. For isotropic antenna array, the nulls have been steered to 45°, −45° and 155° with significant decrease in the depth of nulls. For the rectangular and bowtie patch antenna arrays, the two nulls have been successfully steered towards the peaks of the two side lobes (45° and −45°) except for the third nulling location steered towards the peak of the side lobe at 135° instead of 155°.

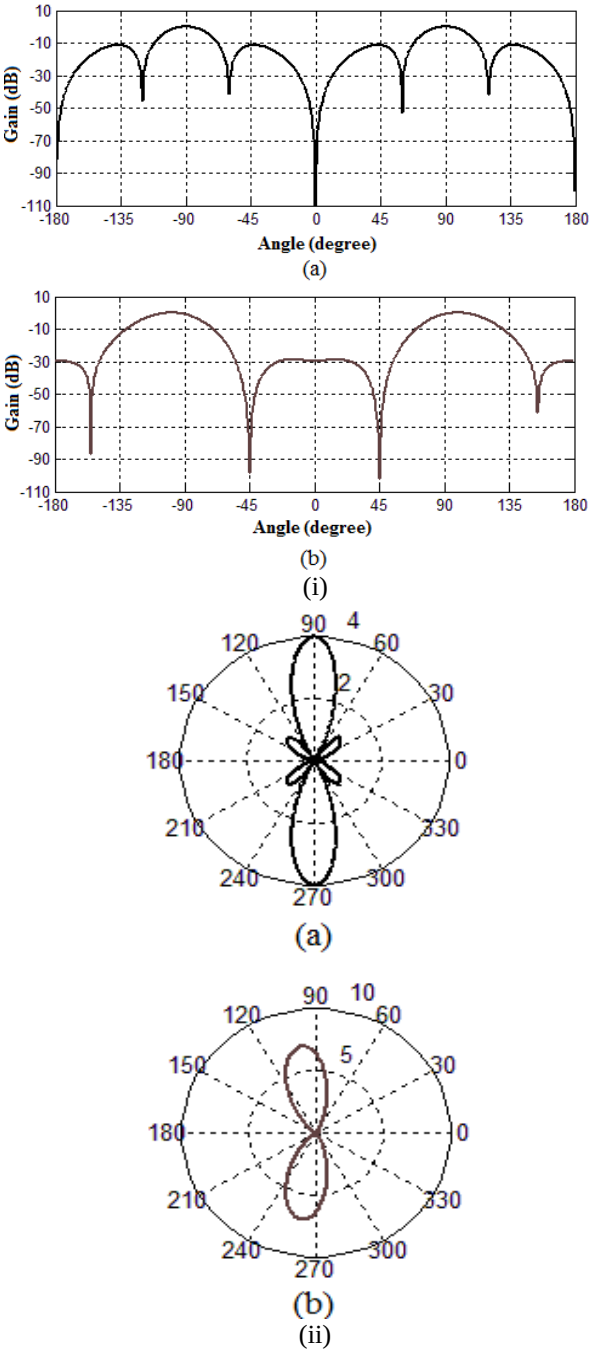

Fig. 2. (i) Gain versus angle plots of 4-element isotropic antenna array with: (a) amplitude 1:1:1:1 and (b) amplitude 0.395:1:1:0.395. (ii) 2D radiation patterns of 4-element isotropic antenna array with: (a) amplitude 1:1:1:1 and (b) amplitude 0.395:1:1:0.395.

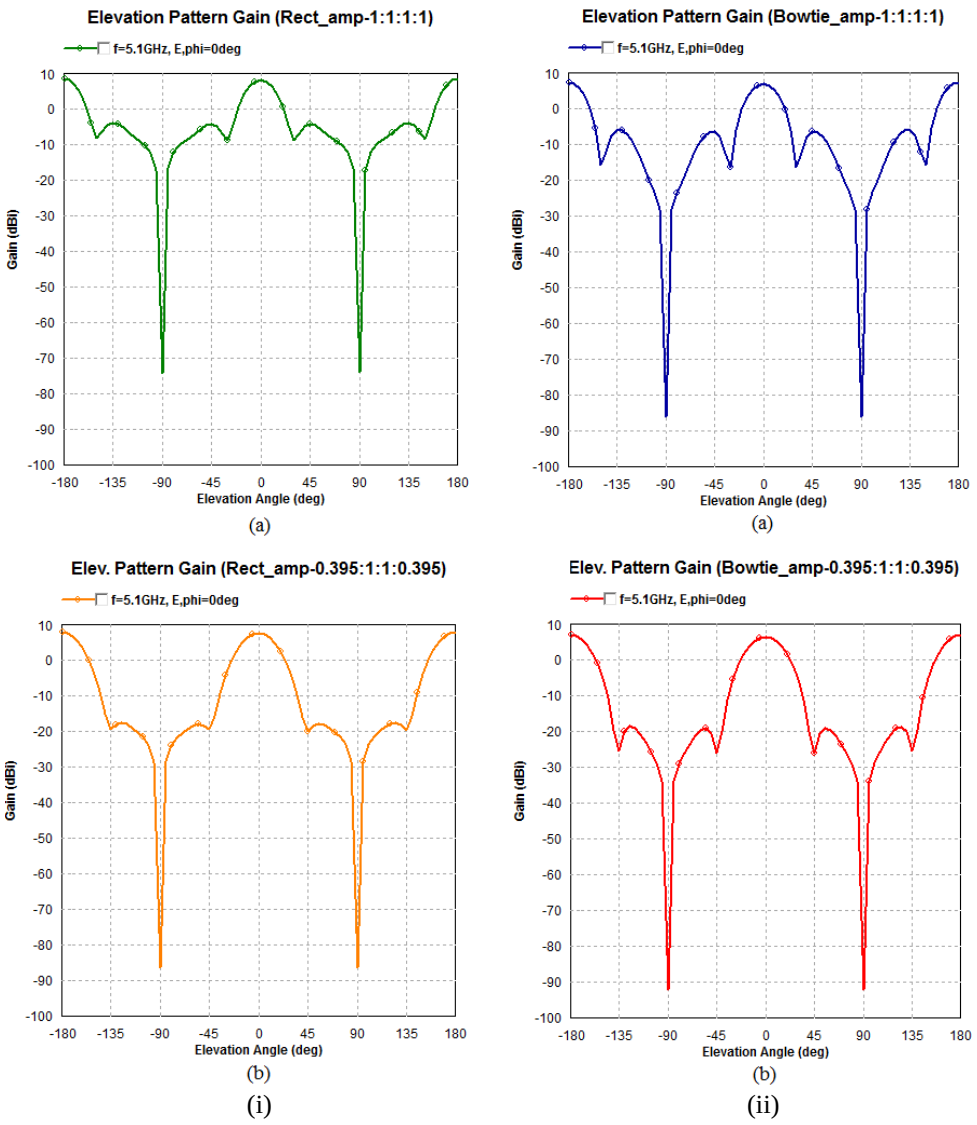

Fig. 3. Gain versus angle plots of (i) 4-element rectangular patch antenna array with: (a) amplitude 1:1:1:1 and (b) amplitude 0.395:1:1:0.395; (ii) 4-element bowtie patch antenna array: (a) amplitude 1:1:1:1 and (b) amplitude 0.395:1:1:0.395.

Table 2: Position and depth of nulls in radiation pattern of 4x1 isotropic and non-isotropic antenna array for different amplitudes

Antenna Element	Amplitude Ratio	Null 1		Null 2		Null 3	
		Position	Depth (dB)	Position	Depth (dB)	Position	Depth (dB)
Isotropic	1:1:1:1	60°	-55	-60°	-40	120°	-40
	0.395:1:1:0.395	45°	-105	-45°	-100	155°	-60
Rectangular	1:1:1:1	30°	-16.57	-30°	-16.49	150°	-16.14
	0.395:1:1:0.395	45°	-27.14	-45°	-26.81	135°	-26.59
Bowtie	1:1:1:1	30°	-22.59	-30°	-22.16	150°	-22.16
	0.395:1:1:0.395	45°	-31.75	-45°	-31.74	135°	-31.39

As can be seen from the plots shown in Figs. 4 and 5 for both the designed antenna arrays, i.e., rectangular as well as bowtie, when we change amplitude ratio to 0.395:1:1:0.395, the gain at 155 º and -155º undergo a slight variation; i.e., from -5.6 dB to -1.08 dB for bowtie antenna array and shows a variation from -4.2 dB to -0.15 dB for rectangular antenna array. However, for both the arrays the gain changes significantly at 135º and -135º as the nulls present at 149º and -149º have got steered towards 135º and -135º, i.e., the direction of maxima of minor lobes (direction of interference).

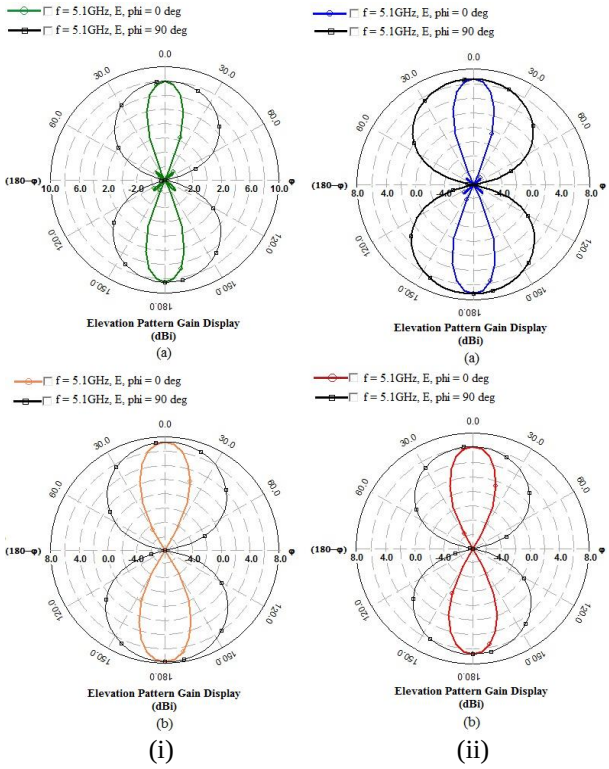

Fig. 4. 2D radiation patterns of (i) 4-element rectangular patch antenna array with: (a) amplitude 1:1:1:1 and (b) amplitude 0.395:1:1:0.395; (ii) 4-element bowtie patch antenna array with: (a) amplitude 1:1:1:1 and (b) amplitude 0.395:1:1:0.395.

Effect of mutual coupling have to be introduced while designing antenna array because in practical arrays this effect changes radiation pattern significantly. Coupling effect produced due to elements interaction while all the elements in array are excited causes elements pattern alter from isolated pattern [21]. Hence, it is important to investigate mutual coupling effect to calculate optimum inter-element spacing and IE3D is a good platform to analyze this effect [22]. To explore the mutual coupling effect, an analysis of the variation of S_{12} with respect to inter-element spacing has been presented in Table 3 and the plots are shown in Fig. 5.

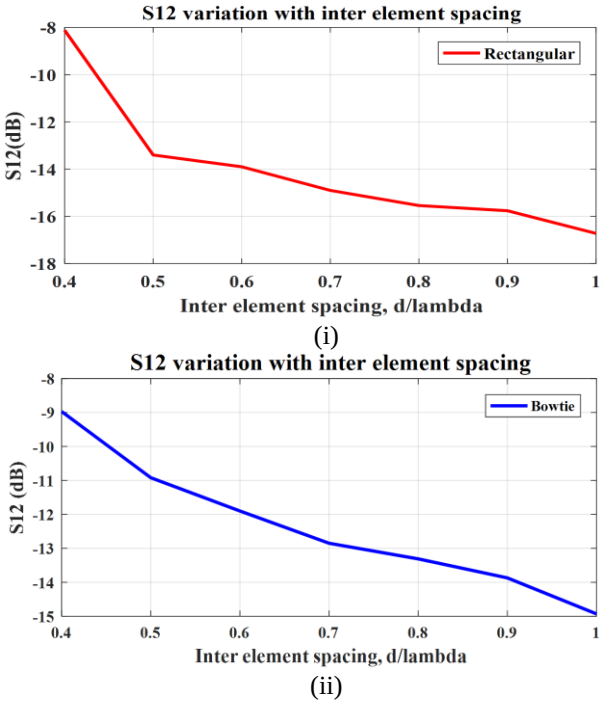

Fig. 5. Mutual coupling of: (i) 4-element rectangular patch antenna array, and (ii) 4-element bowtie patch antenna array.

It is observed from the variation of S_{12} as a function of inter element spacing, that the mutual coupling gets reduced with increase in the element spacing. Furthermore, both the curves plotted in Fig. 5 shows a significant variation in S_{12} for the change in spacing from 0.4λ to 0.5λ. Whereas the variation gets reduced beyond 0.5λ as depicted by the gradual slope of the two curves, thus indicating half wavelength distance to be the optimum one.

The comparative analysis performed for non-isotropic antenna arrays of rectangular and bowtie patches indicates better performance exhibited by the bowtie antenna array not only in terms of occupied area but also improved radiation characteristics. The dimensions of the two elements given in Table 1 show that the area of bowtie patch is 55 mm^2 which is approximately 80% less than that of rectangular patch which leads to much reduced computational time of 31 min 58 sec for bowtie array, whereas the execution takes 10 hr 2 min 29 sec for rectangular array performed on Intel Core™ i7, 3.40 GHz processor. Further, from the performance comparison detailed in Table 3, it can be seen that the value of S_{11} at the optimum spacing (λ/2) for bowtie antenna array is −20.57 dB, whereas for rectangular antenna array it is −13.72 dB.

Table 3: S_{11} and S_{12} for different inter element spacing

Element Excitation (Amplitude Ratio) = 0.395:1:1:0.395						
Inter Element Spacing	4 Element Bowtie Array			4 Element Rectangular Array		
	Resonant Frequency (GHz)	At Resonant Frequency		Resonant Frequency (GHz)	At Resonant Frequency	
		S_{11} (dB)	S_{12} (dB)		S_{11} (dB)	S_{12} (dB)
0.4λ	5.15	-17.97	-8.97	4.43	-21	-8.12
0.5 λ	5.12	-20.57	-10.92	4.93	-13.72	-13.4
0.6 λ	5.02	-22.13	-11.9	4.61	-12.19	-13.9
0.7 λ	4.93	-19.67	-12.85	5.53	-16.2	-14.9
0.8 λ	5.07	-17.24	-13.31	5.17	-16.10	-15.54
0.9 λ	5.12	-18.66	-13.87	4.98	-15.74	-15.76
1 λ	5.08	-20.36	-14.93	4.83	-13.73	-16.72

V. CONCLUSION

Null steering in antenna array of isotropic and non-isotropic elements has been presented in this paper. The algorithm for amplitude controlled null steering of linear antenna array using Schelkunoff polynomial method has been developed in MATLAB. The simulation results demonstrate that by using Schelkunoff method the null steering has been effectively attained in 4-element rectangular antenna array and bowtie antenna array to obtain the desired radiation pattern with nulls imposed at the direction of interferences. The single element bowtie antenna offers the advantage of reduced area but it also achieves high directivity. Further, the results show that using bowtie patches as the element in the array brings about comparatively more effective null steering, and enhances the performance of the array as compared to the conventional rectangular patches, with a decrease in SLL and NDL to −25.47 dB and −31.75 dB respectively, with a significant reduction of the area of the array, which is desirable for application where small antennas are required. It has been observed that the mutual coupling between elements decreases substantially with significant variation at half wavelength spacing.

REFERENCES

[1] K. Guney and S. Basbug, "Interference suppression of linear antenna arrays by amplitude-only control using a bacterial foraging algorithm," *Progress In Electromagnetics Research*, vol. 79, pp. 475-497, 2008.

[2] H. Steyskal, R. A. Shore, and R. L. Haupt, "Methods for null control and their effects on the radiation pattern,"*IEEE Trans. Antennas Propagat*., vol. AP-34, pp. 404-409, 1986.

[3] K. Guney and M. Onay, "Amplitude-only pattern nulling of linear antenna arrays with the use of bees algorithm," *Progress In Electromagnetics Research*, vol. 70, pp. 21-36, 2007.

[4] R. A. Shore, "Nulling at symmetric pattern location with phase-only weight control," *IEEE Trans. Antennas Propagat*., vol. AP-32, pp. 530-533, 1984.

[5] H. Steyskal, "Simple method for pattern nulling by phase perturbation," *IEEE Trans. Antennas Propagat*., vol. AP-31, pp. 163-166, 1983.

[6] W. P. Liao and F. L. Chu, "Array pattern nulling by phase and position perturbations with the use of the genetic algorithm," *Microwave and Optical Tech. Lett*., vol. 15, pp. 251-256, 1997.

[7] H. M. Ibrahim, "Null steering by real-weight control-a method of decoupling the weights," *IEEE Trans. Antennas Propagat*., vol. AP-39, pp. 1648-1650, 1991.

[8] A. Tennant, M. M. Dawoud, and A. P. Anderson, "Array pattern nulling by element position perturbation using genetic algorithm," *Electron. Lett*., vol. 30, pp. 174-176, 1994.

[9] M. V. Lozano, J. A. Rodriguez, and F. Ares, "Recalculating linear array antennas to compensate for failed elements while maintaining fixed nulls," *J. Electromagn. Waves Appl*., vol. 13, pp. 397-412, 1999.

[10] M. M. Khodier and C. G. Christodoulou, "Linear array geometry synthesis with minimum sidelobe level and null control using particle swarm optimization," *IEEE Trans. Antennas Propagat*., vol. AP-53, pp. 2674-2679, 2005.

[11] A. Walia and M. S. Patterh, "Antenna array failure correction using optimization techniques," *Int. J. of Adv. R. Comp. Sc. Software Engg*., vol. 3, pp. 764-769, 2013.

[12] K. Guney and A. Durmus, "Pattern nulling of linear antenna arrays using backtracking search optimization algorithm," *Int. J. Antenn. and Propag*., pp. 1-10, 2015.

[13] S. Choudhari, K. P. Ray, and S. Kulkarni, "Design and development of 4 element linear microstrip patch antenna array with null steering by phase control," *IEEE International Conference on Sustainable Energy and Intelligent Systems*, Chennai, India, pp. 645-649, July 2011.

[14] V. V. Dwivedi and S. Banerjee, "Linear array synthesis using schelkunoff polynomial method and particle swarm optimization," *IEEE International Conference on Advances in Computer Engineering and Applications*, Ghaziabad, India, pp. 727-730, March 2015.

[15] S. Dhamankar and S. Lopes, "Mutual coupling reduction techniques in microstrip patch antennas: A survey," *Int. R. J. Engg. Tech*., vol. 3, pp. 1064-1069, 2016

[16] C. A. Balanis, *Antenna Theory: Analysis and Design*. Wiley, New York, USA, 2005.
[17] H. G. Schantz, "A brief history of UWB antennas," *IEEE Aerosp. Electron. Syst. Mag*., vol. 19, pp. 22-26, 2004.
[18] C. A. Balanis, *Antenna Theory*. Wiley, New York, USA, 2010.
[19] J. George, M. Deepukumar, C. Aanandan, P. Mohanan, and K. Nair, "New compact microstrip antenna," *Electron. Lett*., vol. 32, pp. 508-509, 1996.
[20] C. P. Wen, "Coplanar waveguide directional couplers," *IEEE Trans. Microwave Theory Tech.*, vol. 18, pp. 318-322, 1970.
[21] H. Steyskal and J. S. Herd, "Mutual coupling compensation in small array antennas," *IEEE Trans. Antennas Propagat*., vol. AP-38, pp. 1971-1975, 1990.
[22] F. Tokan and F. Gunes, "Mutual coupling compensation in non uniform antenna arrays using inter-element spacing restrictions," *The Applied Computational Electromagnetics Society J*., vol. 26, pp. 596-602, 2011.

Baljinder Kaur obtained her B.Tech. (Electronics and Communication Engineering) from PTU Jalandhar in 2002 & M.Tech. in (Electronics and Communication Engineering) from SLIET Longowal, in 2012. Presently she is pursuing Ph.D. (Full time Research Scholar) in Dept. of Electronics & Comm. Engg. from SLIET Longowal. Her research interests include microstrip patch and fractal antennas and antenna arrays. She has worked as Faculty for 13 years.

Anupma Marwaha is Associate Professor in Electronics & Comm. Engg. Dept. at SLIET Longowal, Punjab. She did her B.E. & M.Tech. in Electronics & Comm. Engg. in 1990 and 1992 respectively. She completed her Ph.D. Degree in Electronics from Guru Nanak Dev University, Amritsar in the year 2003 with specialization in the field of 'Design and Field Analysis of Electromagnetic Devices by Finite Element Method with applications to Communication Engg., Microwave and Antennas'. She is a Life Member of ISTE, New Delhi & Member of Institution of Engineers, India. She has more than 75 publications to her credit in International and National Journals.

Surekha Rani obtained her B.Tech. (Electronics and Communication Engineering) from SLIET, Longowal, in 2015. Presently she is pursuing M.Tech. in (Electronics & Communication Engineering) from SLIET Longowal. Her research interests include microstrip patch antennas and antenna arrays. She is a Member of Institution of Engineers, India.